Calculation of hydrogen diffusivity and solubility in bcc metals using machine-learning potentials and path-integral methods

체심 입방 격자 금속에서 수소의 확산도와 용해도를 머신러닝 포텐셜과 경로적분을 사용하여 계산하는 방법

2023년 8월

서울대학교 대학원

에너지시스템공학부 원자핵공학전공

권 혁 준

Calculation of hydrogen diffusivity and solubility in bcc metals using machine-learning potentials and path-integral methods

지도교수 Takuji Oda

이 논문을 공학석사 학위논문으로 제출함
2023년 7월

서울대학교 대학원

에너지시스템공학부 원자핵공학전공

권 혁 준

권혁준의 석사 학위논문을 인준함
2023년 7월

위원장 　　　　이유호　　　　(Seal)

부위원장 　　　Takuji Oda　　(Seal)

위　　원 　　　Yuji Hatano　　(Seal)

List of Contents

2

3

4

List of Figures

6

7

List of Tables

Abstract

Calculation of hydrogen diffusivity and solubility in bcc metals using machine-learning potentials and path-integral methods

Hyukjoon Kwon

Department of Energy Systems Engineering

The Graduate School of Engineering

Seoul National University

Hydrogen diffusivity, solubility and permeability in metals has been extensively investigated owing to its rich physical characteristics and importance in materials engineering. For nuclear materials engineering, the hydride formation in Zr alloys used as cladding materials in water-cooled nuclear fission reactors has been extensively studied as it significantly degrades the ductility of Zr alloys. For the development of nuclear fusion reactors, not only embrittlement/damage caused by hydrogen isotopes in metals but also the behavior of tritium itself is an important research topic, since the accumulation and leakage of tritium in reactor components need to be minimized to satisfy safety regulation due to the radioactivity of tritium and the tritium needs to be quickly recovered and used as fuels to sustain the fusion fuel cycle.

In spite of many experimental efforts, there are large deviations in the reported experimental data of diffusion coefficients and solubility constants due to surface and trapping effects, indicating that accurate measurements are inherently difficult, especially at low temperatures. For computational studies, several atomistic simulation methods have been proposed and used to determine the true hydrogen diffusivity and solubility in the lattice; however, their accuracy remains questionable

as most studies have not accurately simulated the force field, dynamic effects, or NQEs.

In this study, for bcc-Fe and bcc-W, we estimated the diffusivity and solubility of dilute hydrogen from long-time path integral simulations using machine-learning moment tensor potentials with the accuracy of density functional theory (DFT), which accurately handles the three factors (force field, dynamic effects, NQEs) simultaneously.

In the temperature range where the experiments of the diffusion coefficients seem reliable (>500 K for Fe, and >1500 K for W), our calculations show excellent agreement for the metals. Protium diffusion coefficients exhibited non-linear Arrhenius plots due to NQEs at temperatures below 500 K in Fe and W. Regarding isotope effects, even for classical diffusion coefficients above 500 K, the diffusivity ratio deviated from the square root of the mass ratio. We attributed this to dynamic effects caused by hydrogen-phonon coupling.

Our process to calculate the solubility is theoretically more accurate than the methods used in previous studies such as quasi-harmonic approximation (QHA) in that coupling of dynamic effects and NQEs is fully included in our process. Our solubility results are indirectly compared with the experimental values by converting them into permeability because the permeability at high temperatures can be more accurately measured than the solubility in experiments. The results showed an acceptable level of error compared to the available experimental values, while systematic error of DFT is transferred to the solubility to some extent through machine-learning potentials. These results demonstrate that precise measurements over a wide temperature range remain a challenge in experimental studies and simple calculation methods. Until now, many studies have calculated hydrogen diffusivity and solubility in metals using QHA without rigorous validation on approximations in it. According to this research, when dynamic effects, including NQEs are significant (e.g., in bcc-Fe), using QHA can result in errors of several orders of magnitude for the hydrogen solubility. This research has increased the applicability of molecular dynamics by developing a methodology that accurately

10

considers dynamic effects and NQEs through the combination of path integral simulations and statistical mechanical techniques.

We have developed a systematic methodology to accurately calculate hydrogen diffusivity and solubility in bcc metals, with the ability to automate the entire process. This research has the potential to create a comprehensive database on diffusivity, solubility, and permeability of hydrogen isotopes for fusion reactor materials, which can greatly contribute to nuclear fusion materials engineering. Additionally, the methods used in this study can be applied to designing functional materials that prevent hydrogen-related issues in various applications, including nuclear fission reactors and hydrogen ships for the hydrogen economy.

Student Number: 2021-29372

Abbreviation

"Engineering and theoretical background"

PFMs: Plasma-facing materials

NQEs: Nuclear quantum effects

FSEs: Finite size effects

"Forcefields"

DFT: Density functional theory

PES: Potential energy surface

MLP: Machine-learning potential

MTP: Moment tensor potential

"Molecular dynamics"

CLMD: Classical molecular dynamics

PIIMD: Path integral molecular dynamics

AI-PIMD: Ab-initio PIMD

RPMD: Ring polymer molecular dynamics

CMD: Centroid molecular dynamics

PI-QTST Path integral quantum transition state theory

"Molecular statics"

NEB: Nudged elastic band

QHA: Quasiharmonic approximation

CL-HA: Classical harmonic approximation
Q-HA: Quantum harmonic approximation

CL-QHA: Classical QHA

Q-QHA: Quantum QHA

"Others"

SC: Scaled coordinate

Nomenclature

Physical constants

k_B: Botlzman constant

$\hbar$: Reduced Planck constant

General variables

t: time

m: mass

T: temperature

$\beta = 1/k_B T$

P: Pressure

V: Volume

a: Lattice constant

Diffusion

D: Diffusion coefficient

E_a: Activation energy

Solution

θ: Solution constant

Permeation

ϕ: Permeation constant

J: Permeation flux

Thermodynamics

G_{sol}: Solution Gibbs energy.

H_{sol}: Solution enthalpy.

S_{sol}: Solution entropy.

G_X: Gibbs free energy of system X.

H_X: Enthalpy of system X.

S_X: Entropy of system X.

U_X: Internal energy of system X.

μ_X: Chemical potential of system X.

h_X: Enthalpy per molecule X.

s_X: Entropy per molecule X.

Statistical mechanics

$\Delta(N, P, T)$: Isothermal-isobaric partition function at constant N, P, and T.

$Q(N, V, T)$: Canonical partition function at constant N, V, and T

$\langle ... \rangle^X$: Ensemble average of an ensemble X.

W: Virial

1. Introduction

1.1. Issues related to hydrogen isotopes in fusion reactor materials

A fusion reactor using the nuclear reaction between deuterium (D) and tritium (T) is considered to be the earliest feasible fusion energy plant, and has been the subject of much research, including a large international project ITER, which is currently under construction in France. Tritium is a radioactive hydrogen isotope whose natural abundance is extremely low, so in order to use it as fuel in a fusion reactor, it must be efficiently produced, recovered, managed, and utilized in the fusion reactor. However, the high mobility and permeability of hydrogen in materials makes it difficult to thoroughly predict and control the behavior of hydrogen isotopes. The issues related to hydrogen isotopes behavior in fusion reactor materials are summarized in three aspects as below.

Firstly, tritium inventory and leakage pose challenges to radiation safety and environmental protection due to the radioactivity of tritium. Tritium has a half-life of approximately 12.3 years and emits high-energy electrons through β^- decay. Thus, the leakage of tritium must be prevented from a perspective of the protection of workers and environment. Beryllium and tungsten are typical materials used as plasma-facing materials (PFMs) and also act as the first barrier to confine tritium. Beryllium can be used in the main vessel walls, and tungsten can be used in the divertor. During the operation of the reactor, there is a problem of tritium dissolution in the PFMs, leading to a significant amount of tritium remaining in the inventory. For example, Roth et al. demonstrated that in a hypothetical scenario where ITER operates for around 2500 shots of 400 s discharges, approximately 700g of tritium, which is the expected regulation limit for T retention, remains inside the PFMs if the Be and W are used as first walls and divertor, respectively[1]. If W is used for both first walls and divertor, the T retention can be reduced. However, radiation damages caused by fast neutrons are expected to trap T, increasing the retention. Therefore, many studies have been performed to identify the effects of radiation defects on T retention[2], and this research field is still attracting large attention.

16
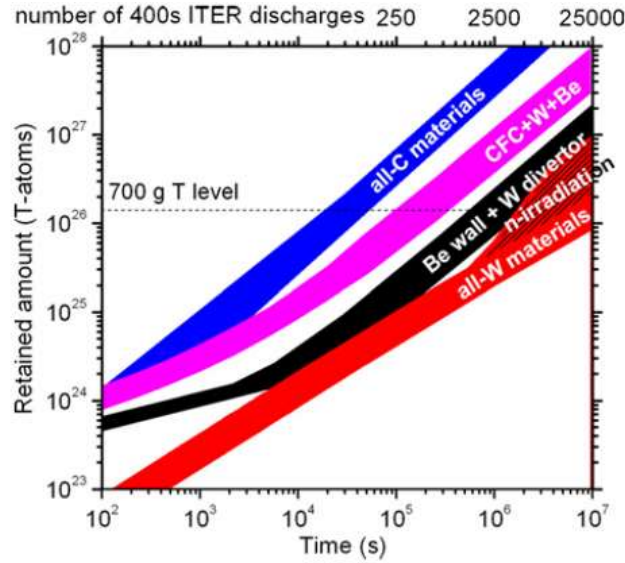
Fig. 1.1-1 Tritium inventory ion material used in ITER after operation time. This figure was taken from Ref. [1]. CBC denotes carbon fibre composite.

Secondly, large amount of tritium loss can threaten fuel cycle sustainability. Tritium is a radioactive isotope and does not exist as a natural resource; it needs to be artificially produced through the tritium breeding process. Maintaining the tritium balance (breeding, burning, and loss) is generally a difficult task because tritium loss occurs in various ways in fusion reactors. The primary channels for tritium loss are trapping in PFMs, leakage through the first wall, and β^- decays as well as leakage in fueling systems [3]. While it is inevitable for tritium to be naturally lost through the radioactive decay during tritium storage, there is a necessity to minimize the amount of tritium lost through trapping and leakage through materials. If this can be achieved by developing new materials or processes such as the use of coatings that act as tritium permeation barriers, it would increase the cost-effectiveness and sustainability of nuclear fusion reactors.

17
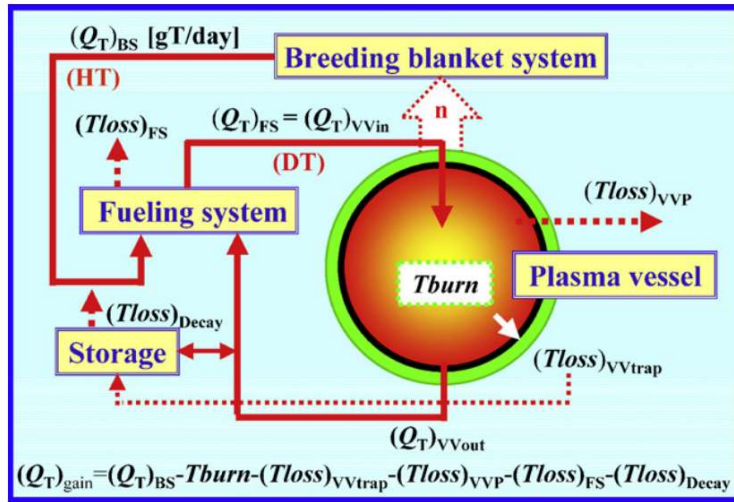
Fig. 1.1-2 Tritium balance in a DT fusion reactor. $(Tloss)_{VVtrap}$: Trapping rate of T to plasma facing materials $(Tloss)_{VVPp}$: T loss due to permeation through first wall $(Tloss)_{FS}$: T loss in fuel system $(Tloss)_{Decay}$: T loss due to β^- decay in T inventory. This figure was taken from Ref. [3]

Finally, hydrogen embrittlement can pose a serious problem for the long-term operation of fusion reactors by deteriorating the materials properties of PFMs. The presence of residual hydrogen in the PFMs can potentially induce hydrogen stress cracking or create cavities by exerting additional pressure within the metal. Fang et al. reported a maximum hardness increase of approximately 0.5 GPa in tungsten exposed to deuterium plasma [4]. To prevent hydrogen embrittlement, it is important to find materials for PFMs that minimize hydrogen inventory or find methods or operation scenarios to minimize hydrogen inventory.

1.2. Basic materials properties on hydrogen behavior: diffusivity, solubility, and permeability

Hydrogen inventory and leakage are determined by three key material properties: diffusivity, solubility, and permeability. Hydrogen diffusion refers to the phenomenon where hydrogen atoms within a metal randomly migrate between interstitial sites. Hydrogen solution describes the phenomenon where H_2 molecules present in a vacuum are dissolved into the metal, maintaining an equilibrium concentration. Hydrogen permeation is the phenomenon where hydrogen moves from a region of lower concentration to a region of higher concentration due to the chemical potential gradient between two spaces with a membrane in between. In homogeneous membranes under isothermal conditions, the hydrogen concentration gradient can be assumed to be constant, which leads to the relationship, Permeability = Diffusivity × Solubility.
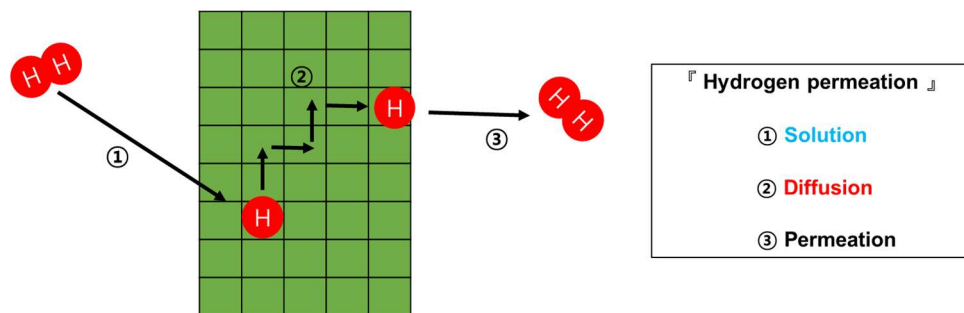
Fig. 1.2-1 A schematic diagram illustrating diffusion, solution, and permeation of hydrogen in metals.

This relation can be intuitively understood. When the solubility is held constant and the diffusivity increases, the speed of movement from low concentration to high concentration is accelerated. Therefore, the permeability should grow proportionally. On the other hand, when the diffusivity is held constant and the solubility increases, the absolute amount of hydrogen present in the metal grows. As

a result, the net amount of hydrogen escaping from the high concentration space to the low concentration space increases, leading to an increase in permeability proportionally.
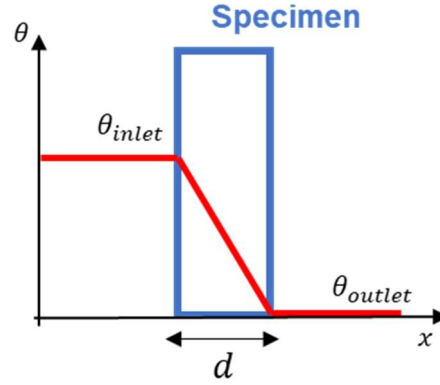
Fig. 1.2-2 Hydrogen concentration profile in gas permeation experiments.

$\boldsymbol{d}$ denotes thickness of a specimen.

The diffusion is quantified by the material property called *diffusion coefficient*. Macroscopically, the diffusion coefficient appears in Fick's law as follows:

$$\text{Fick's 1st law: } J = -D\frac{\partial \theta}{\partial x}, \qquad \text{Eq. 1.2-1}$$

$$\text{Fick's 2nd law: } \frac{\partial \theta}{\partial t} = -\frac{\partial J}{\partial x} = D\frac{\partial^2 \theta}{\partial x^2} \qquad \text{Eq. 1.2-2}$$

J denotes the hydrogen permeation flux $[\text{mol } H_2 \cdot m^{-2} \cdot s^{-1} \cdot \text{MPa}^{-0.5}]$, and D and θ are diffusion coefficients $[m^2 \cdot s^{-1}]$ and hydrogen concentration (solution constants inside the specimen) $[\text{mol } H \cdot m^{-3} \cdot \text{MPa}^{-0.5}]$, respectively.

Microscopically, D can be expressed as the jump frequency (ν_{jump}) and the activation energy (E_a) in lattice where n_{jump} is the number of neighbor sites to which a diffusing atom can jump, f_{jump} is a coefficient for jump correlation and λ_{jump} is a unit jump distance.

$$D(T) = \frac{1}{6}\left(n_{jump} f_{jump} \lambda_{jump}^2\right) \nu_{jump} e^{-\frac{E_a}{kT}} \qquad \text{Eq. 1.2-3}$$
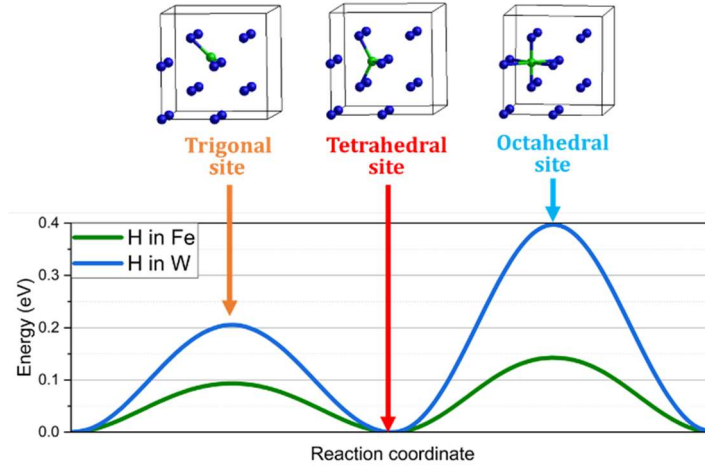
Fig. 1.2-3 Minimum energy path of hydrogen migration in bcc-Fe and bcc-W by the DFT calculations.

The solution can be quantified by a material property known as the solubility constant. This constant represents the concentration of hydrogen in a material that is in equilibrium with the pressure of hydrogen gas $\left(P_{H_2}\right)$. Using the solubility constant, the concentration of hydrogen in a metal at equilibrium with a hydrogen gas of a partial pressure of P_{H_2} can be express with solution entropy (S_{sol}) and solution enthalpy (H_{sol}) [5]. n_{sites} denotes the number of interstitial sites in a unit cell, which is 6 for the tetrahedral sites in bcc crystals.

$$\theta\left(P_{H_2}, T\right) = n_{sites}\sqrt{\frac{P_{H_2}}{P_{1bar}}} exp\left(\frac{S_{sol}(P_{1bar}, T)}{k_B}\right) exp\left(-\frac{H_{sol}(P_{1bar}, T)}{k_B T}\right) \quad \text{Eq. 1.2-4}$$

This equation is derived by equilibrium theory of thermodynamics at chemical equilibrium between hydrogen gas and hydrogen solute state. For some metal-hydrogen systems such as Nb-H, the concentration of solute hydrogen exceeds the threshold concentration, namely, the solubility limit, a hydride phase can be formed.

This hardly occurs for other metal-hydrogen systems such as Fe-H and W-H where the thermodynamic stability of hydride phases is low. Note that, in the present study, we basically focus on hydrogen at a dilute limit, where the hydrogen concentration is far lower than the solubility limit and hydrogen-hydrogen interaction in a metal does not significantly occur.

The permeation is quantified by the material property called *permeability constant*. Macroscopically, the permeability coefficient (ϕ) is derived by solving Fick's 2nd law under the permeation flux at steady state (J_{steady}).

$$\frac{\partial \theta}{\partial t} = \frac{\partial^2 \theta}{\partial x^2} = 0$$

$$\theta(x,t) = \theta_{inlet}\left[1 - \frac{x}{d} - \frac{2}{\pi}\sum_n \sin\left(\frac{n\pi x}{d}\right)\exp\left(-\frac{Dn^2\pi^2}{d^2}t\right)\right]$$

$$J(x,t) = -D\frac{\partial \theta}{\partial x}(x,t) = \frac{D\theta_{inlet}}{d}\left[1 + 2\sum_n n(-1)^n \cos\left(\frac{n\pi x}{d}\right)\exp\left(-\frac{Dn^2\pi^2}{d^2}t\right)\right]$$

$$J_{steady} = \lim_{t\to\infty} J(d,t) = \frac{D\theta_{inlet}}{d}$$

For the saturated hydrogen permeation flux, the permeability coefficient [mol $H_2 \cdot m^{-1}\cdot s^{-1}$] equals D times $\theta\left(P_{H_2}\right)$.

$$\therefore \phi = J_{steady}d = D\theta_{inlet} \qquad\qquad \text{Eq. 1.2-5}$$

1.3. Low reliability of experimental data on diffusivity and solubility

Despite great experimental effort, accurate measurement of diffusion coefficients has been hampered by lattice imperfections such as surfaces, impurities, and defects[6]. Thus, experimentally measured diffusion coefficients often fail to represent actual diffusion coefficients in the lattice. For example, the deviation of reported diffusion coefficients for Fe or W is several orders of magnitude at room temperature [6–8].
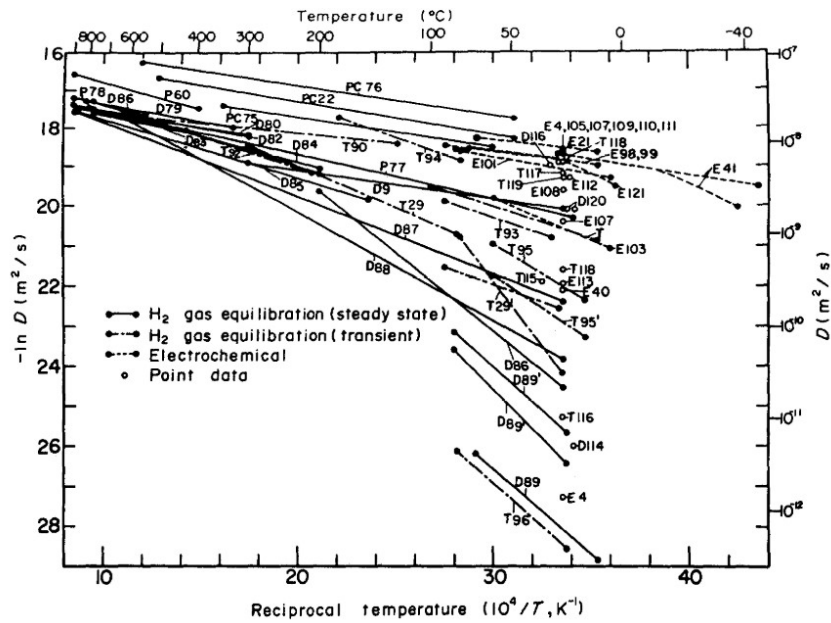
Fig. 1.3-1 Experimental values of protium diffusion coefficients in Fe.

This figure was taken from Ref. [6].

The large scattering in the experimentally data can be explained by three factors: surface effects, trap effects sch as impurity and vacancy, and grain-boundary effects.

Firstly, the differences in experimentally measured diffusivity can be

23

attributed to the high adsorption energy on the metal surface, known as surface effects. Studies conducted by Jiang and Carter[9] for bcc-Fe, and Heinola and Ahlgren[10] for bcc-W used first principles calculations based on density functional theory (DFT) to evaluate the adsorption energy of hydrogen on metal surfaces, which ranges 0.38-0.91 eV in reference to H_2 gas molecule and 0.58-1.86 eV in reference to solute H in metals. The high adsorption energy is identical to high desorption energy, which interferes with the recombinational desorption of hydrogen to a gas phase, contaminating non-steady state permeability data and reducing the accuracy of the H_2 gas permeation technique in experiments.
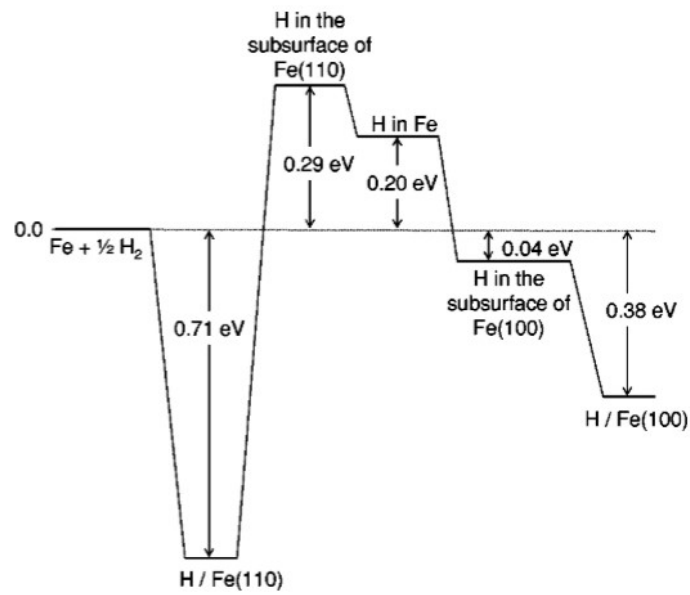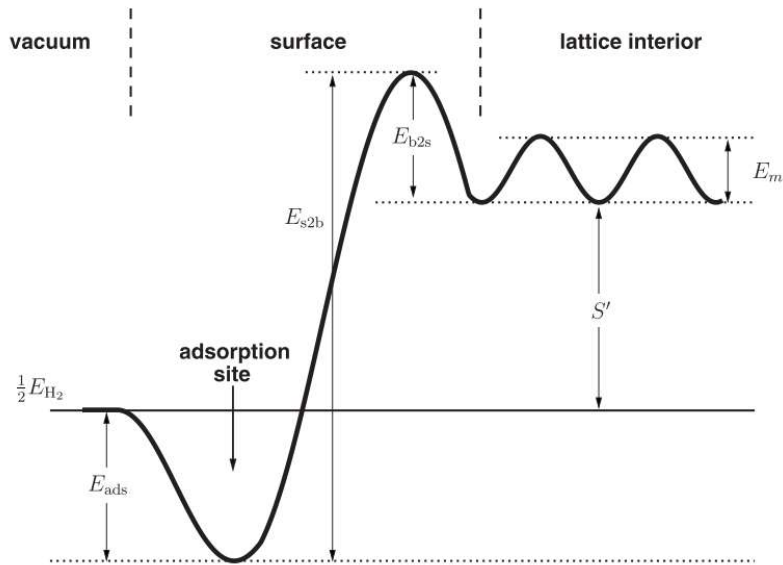
Fig. 1.3-2 Energy landscape of hydrogen from **H₂** gas to the dissolved state in (upper) Fe and (lower) W. DFT was used to calculate the landscapes. These figures were taken from Ref. [9,10]

Secondly, the trapping effects of impurities and point defects such as vacancies slow down hydrogen diffusion by increasing the activation energy required for migration. For hydrogen in bulk Fe and W, Tateyama and Ohno[11] and Ohsawa et al[12]. used DFT to determine the negative energy associated with hydrogen trapping by mono-vacancies, indicating that hydrogen is more likely to occupy vacancies rather than tetrahedral sites. Oda et al. showed by kinetic Monte Carlo simulations that such trapping effects cause non-linear relation between logarithm of apparent hydrogen diffusion coefficients and reciprocal temperature, depending on the concentration of traps, and can explain large deviation observed in experimental data of hydrogen diffusivity in W[13], as suggested by Heinola et al.[14] Therefore, at low temperatures where the trap effect cannot be negligible even if the trap concentration is relatively low, it is essentially difficult to measure the true diffusion coefficient of hydrogen in lattice.

25

Finally, the diffusion of trapped hydrogen at grain boundaries can exhibit a different behavior compared to diffusion in a perfect lattice at whole temperature ranges. While hydrogen trapped by vacancies cannot migrate without detrapping, hydrogen trapped at grain boundaries can still migration with being trapped. Due to the wide variety of grain boundaries and the potential for each type to exhibit completely different behaviors, the experimental diffusion coefficients were thought to show large scattering depending on the microstructure within the specimen.
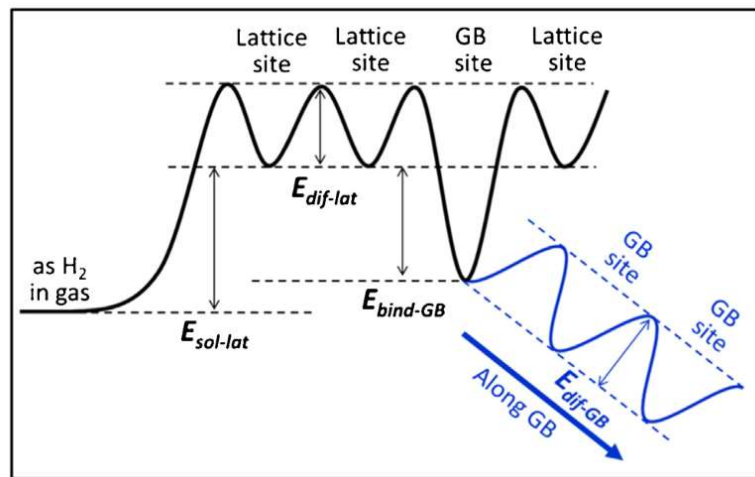
Fig. 1.3-3 Potential energy curve for hydrogen in W. GB denotes a grain boundary. This figure was taken from Ref. [15]

Even disregarding the three systematic error factors mentioned earlier (surface, trapping, and grain boundary effects), the lag-time method in H_2 gas equilibration technique has a high level of random error in measuring diffusivity.
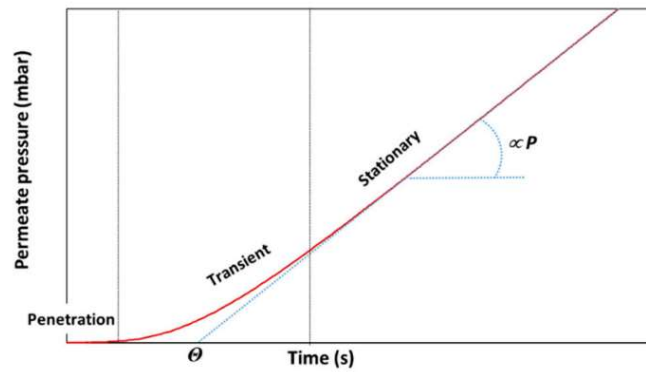
Fig. 1.3-4 Typical output curve of a lag-time method in H_2 gas equilibration experiments. This figure was taken from Ref. [16] θ **and** P in this figure denotes time lag and H_2 pressure.

As illustrated in Figure 1.3-4, diffusion coefficients are measured in transient states, while permeation constants are measured in stationary states. Generally, the permeate pressure highly fluctuate in transient states. Thus, precision of measured diffusion coefficients is not as high as that of measured permeation constants in H_2 gas equilibration experiments.

It should be noted that permeability in Fe and W is commonly reported consistently in experimental studies[7,17–19], whereas diffusivity showed large scattering, leading to lower accuracy in determining solubility. This comes from the fact that the effects of traps such as vacancies on apparent diffusivity is cancelled with those on apparent solubility, resulting in no trap effects on determined permeability. However, this cancellation cannot be fully achieved if hydrogen can diffuse with being trapped by GBs, which causes deviation even in permeability data if the temperature is low enough for GBs to significantly trap hydrogen[15].

1.4. Low availability of data for deuterium and tritium

There are two main issues for low availability of experimental data for deuterium and tritium. Their large mass results in lower diffusivity than that of protium, which not only takes longer to reach the equilibrium state in specimens but also decreases the permeation rate, leading to poor experimental accuracy as the effects of lattice imperfection become relatively large. In addition, tritium is a radioactive isotope, requiring special facilities with the radiation shielding. This incurs significant costs for the setup and maintenance of such facilities.

From the perspective of classical physics, isotope effects on diffusivity and solubility are constant at whole temperatures, so deuterium and tritium data can be estimated from experimental data of protium. In the case of diffusivity, neglecting the dynamic effects owing to the hydrogen-phonon coupling, the diffusivity ratio between isotopes is inversely proportional to the square root of their mass ratio[20]. Therefore, the diffusion coefficients of deuterium and tritium would be approximately $\sqrt{2}$ and $\sqrt{3}$ times smaller than that of protium, respectively. However, even at high temperatures where classical limit is expected to be satisfied, the large discrepancy in measured diffusivity with the classical theory is often observed for Fe. Fig. 1.4-1 shows the diffusion coefficient ratio between H and D in bcc-Fe [18]. According to Vineyard's study [20] explained by the strong hydrogen-phonon interaction[19]in Fe, which may come from relatively small mass of Fe, compared to heavy metals, such as W.
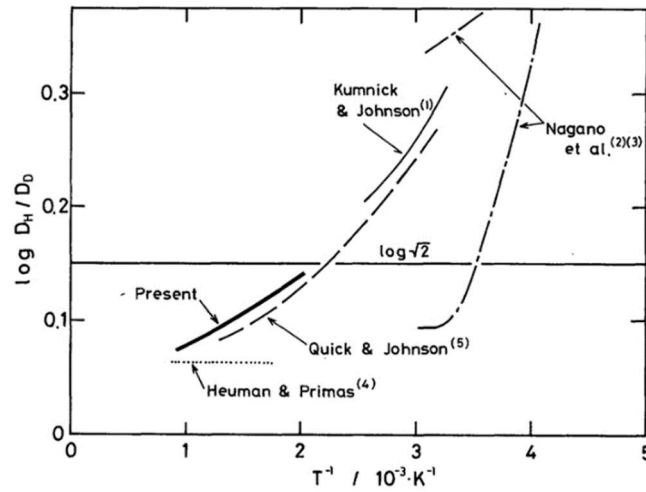
Fig. 1.4-1 Ratio of diffusion coefficient of hydrogen to that of deuterium in Fe (D_H/D_D). According to classical physics, $D_H/D_D \cong \sqrt{m_D/m_H} = \sqrt{2}$. This figure was taken from Ref. [18]

As for solubility, it is determined by the Gibbs free energy between the H_2 molecule and the dissolved state. Since the classical Gibbs free energy is independent of mass, there is no isotope effect on solubility.

On the other hand, from the perspective of quantum physics, isotope effects that take into account NQEs exhibit temperature dependence at low temperatures, while they converge to the classical results at sufficiently high temperatures. Qi et al.[21] experimentally measured the hydrogen diffusivity in bcc-Nb for all isotopes of hydrogen at temperatures above 100 K.

29
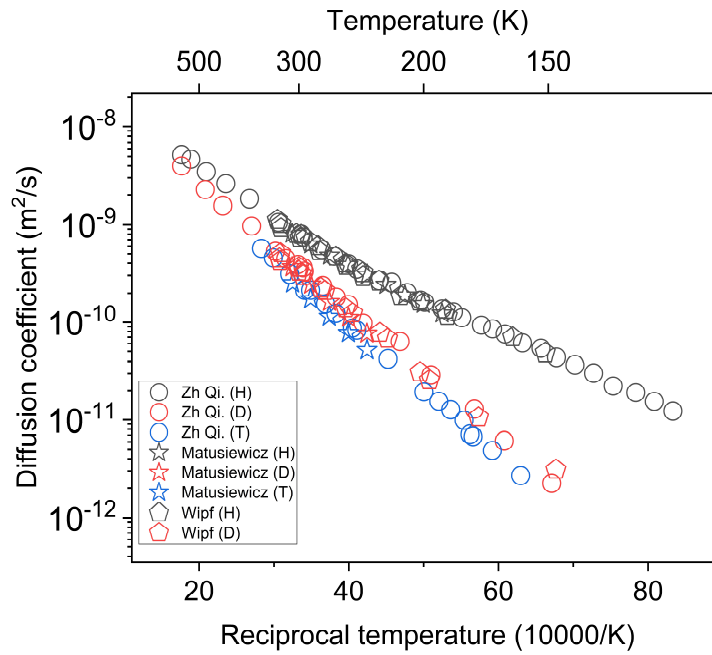
Fig. 1.4-2 Hydrogen diffusion coefficients in bcc-Nb. According to classical rate theory, the Arrhenius plots of diffusion coefficients is approximately linear. The experimental values are from Ref. [21–23].

Contrary to the expected temperature dependence of diffusion coefficients based on the classical Arrhenius equation, their results showed non-linearity below approximately 250 K. That quantum diffusivity is attributed to tunneling effects and ZPE. Tunneling effects act as factors that always accelerate the hydrogen diffusion, while ZPE can either accelerate or slow down diffusion depending on the change in the free energy barrier. Therefore, significant isotope effects are anticipated in hydrogen diffusivity. Kimizuka and Shiga [24] demonstrated through path integral simulations that the quantum diffusivity of protium in fcc-Ag and fcc-Cu can be smaller than the classical diffusivity. Similarly, in the case of solubility, it is expected that mass dependence will arise due to NQEs, but research on this aspect is still limited.

1.5. Objectives of this study

There is a need to develop new materials or methods that effectively prevent hydrogen inventory and leakage in nuclear fusion reactors. However, there are two barriers to experimentally designing nuclear materials and prevention methods. Firstly, as highlighted in Sections 1.3 and 1.4, the experimental determination of hydrogen diffusivity, solubility, and permeability is challenging due to their significant dependence on the material's microstructure and unavoidable effects of surface and trap effects, making it difficult to obtain precise values. Secondly, the vast number of possible combinations of elements and their compositions for new alloy development results in an enormous amount of labor and time required.

Therefore, computational materials design is needed to develop an automated process for calculating the properties of materials including hydrogen diffusivity and solubility in order to find adequate materials for each application. In the pharmaceutical industry, Virtual Screening, a computational chemistry method, is used to reduce the number of potential drug candidates before experiments and clinical trials. Similarly, for nuclear materials engineering, a computational chemistry approach is required to simplify the process of finding alloy compositions that optimize material properties in PFMs and cladding materials. To achieve this, there is a need for research on automatically and accurately calculating the hydrogen transport properties in alloys.

However, accurate computations of both diffusivity and solubility have not been straightforward. One must carefully consider dynamic effects and nuclear quantum effects (NQEs) involved in the transport mechanism, which are important at high and low temperatures, respectively. Dynamic effects beyond the harmonic approximation are not considered in the conventional minimum energy path analysis [9,14], whereas NQEs are not considered in classical molecular dynamics (CLMD) simulations [25]. Through path integral simulations, it is possible to include dynamic effects and NQEs naturally [26,27]. However, the reliability of PI simulations based on empirical force fields is questionable, because the results are sensitive to the assumed

31

potential energy surface (PES). Ab initio path integral molecular dynamics (AI-PIMD) [28–30] is one of the most ideal approaches for this purpose, fully rooted in first-principles calculations; however, its application to hydrogen diffusion in metals is not yet practical due to the enormous amount of computations.

Recently, the concept of machine-learning potential (MLP) has emerged, and the paradigm of the potential model has dramatically changed [31]. By learning from first-principles calculations, the MLP can provide an accurate PES at a low computational cost. It has recently been reported that MLPs based on artificial neural networks [32] and Bravais-inspired gradient domains [33] work successfully for hydrogen diffusion in fcc-Pd.

In this study, the diffusivity and solubility of dilute hydrogen in Fe and W are investigated through PI simulations using a modern MLP known as moment tensor potential (MTP) [34]. The objective of this research is to establish accurate and efficient computational methods for hydrogen solubility and diffusivity in bcc metals and obtain reliable data above 100 K and reveal NQEs and isotope effects on hydrogen transport over the entire temperature range.

The biggest difference between the current target system of study and the reality is that we use single crystals, whereas actual materials are polycrystals. Generally, the existence of grain boundaries increases the effective diffusivity and solubility because the interfaces provide fast diffusion paths and voids which are the preferred locations than the tetrahedral sites for the solute hydrogen.

If the actual material has low concentrations of grain boundaries, the difference between single crystal and polycrystal in terms of diffusivity and solubility would generally be negligible at sufficiently high temperatures. In this study, we used data obtained at sufficiently high temperatures when comparing experimental and calculated values. In such cases, the experimental values can serve as good reference data for our calculations. On the other hand, if the actual material has high concentrations of grain boundaries, even at sufficiently high temperatures, there can

be significant differences between the measured values and the calculated values. The effects of the lattice imperfections remain as future task, and the results of this study can be reference data for it at the low concentration limit.

In the remainder of this manuscript, after a detailed description of the methodology in Section 3, we show that MTP can successfully reproduce first-principles calculations based on density functional theory, not only for energy, force, and stress data but also for characteristic quantities of the transport phenomena such as the hydrogen migration barrier and vibrational frequencies. This partially justifies the assumption that PI simulations using MTP can produce similar results to ab initio PI simulations using DFT.

In Section 4, the diffusion coefficients calculated using the verified MTPs are compared with the available experimental data, demonstrating that the proposed method can provide reliable diffusion coefficients for Fe and W. Subsequently, NQEs and dynamic effects are identified by comparing the calculations from CLMD and three PI methods: ring polymer molecular dynamics (RPMD), centroid molecular dynamics (CMD), and path integral quantum transition state theory (PI-QTST).

In Section 5, we introduce a methodology that utilizes path integral simulations to calculate the solubility, taking into account dynamic effects and NQEs simultaneously. Section 5.1 provides the theoretical background on this approach, while Section 5.2 presents the methods for calculating the two components that constitute solubility: solution enthalpy and solution entropy. In Section 5.3, the calculated solubility is compared to experimental values after converted to permeability because consistent experimental values have been reported for it.

Hereafter, protium, deuterium, and tritium are referred to as H, D, and T, respectively. When discussing without specifying the type of isotope, the term 'hydrogen' is used.
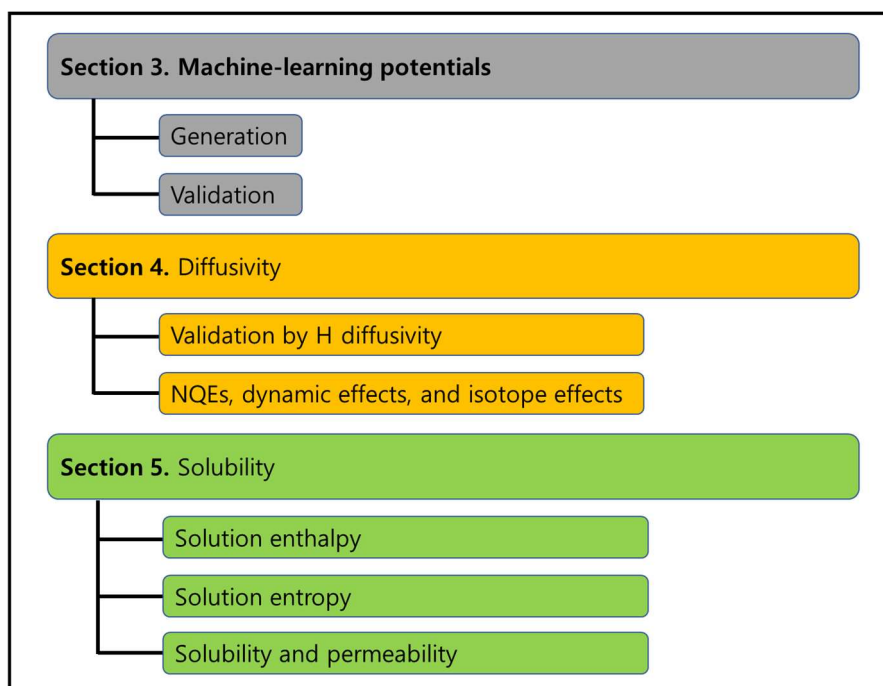
Fig. 1.5-1 Main contents of this thesis

2. Methods

2.1. Moment tensor potential (MTP)

MTP imitates target PESs by a set of polynomials. The theoretical concept of MTP is described in Ref. [34], and its systematic generation process is illustrated in Ref. [35]. The key features of MTP are explained in Section A1 of the Appendix.

Two advantages of MTP are worthy of attention. First, angle-dependent manybody interactions are embodied from the tensor products of atomic displacement, so a variety of atomic environments can be represented by MTP. Second, the computational burden is much relieved in that the MTP algorithm is devoid of any transcendental function but contains only arithmetic operations of polynomials. For several systems, it was confirmed that MTP achieved accuracy comparable with that of Gaussian approximation potential, which is often regarded as one of the most accurate MLPs, with less than a tenth of the computation time [34].

2.2. Imaginary time path integral theory

According to imaginary time path integral theory, the quantum canonical partition function of a particle can be approximated to the classical partition function of a ring polymer with n_{bead} imaginary time slices [36]. Each imaginary time slice can be expressed as "bead" of the ring polymer. Based on this classical isomorphism, the one-dimensional quantum canonical partition function of a nucleus in a physical potential (V_{ph}) is approximated by

$$Z \cong \left(\frac{mn_{bead}}{2\pi\beta\hbar^2}\right)^{\frac{n_{bead}}{2}} \int dq^{(1)} \cdots dq^{(P)} \exp\left(-\beta V_{eff}\right) \qquad \text{Eq. 2.2-1}$$

and the effective potential (V_{eff}) is defined as

$$V_{eff} = \sum_{s=1}^{P} \left[\frac{1}{2}m\omega_P^2\left(q^{(s)} - q^{(s+1)}\right)^2 + \frac{1}{P}V_{ph}\left(q^{(s)}\right)\right], \qquad \text{Eq. 2.2-2}$$

where m is the mass of the nucleus, $q^{(s)}$ is the position of the s-th bead, and $q^{(P+1)} = q^{(1)}$ due to periodicity. ω_P is a harmonic chain frequency.

$$\omega_P = \frac{\sqrt{n_{bead}}}{\beta\hbar}, \qquad \text{Eq. 2.2-3}$$

In the high-temperature limit ($\beta \to 0$), the spring constant ($m\omega_p^2$) becomes so large that the ring polymers shrink toward their centroids. In this limit, the nucleus loses its quantum nature and the quantum partition function converges to its classical one.

We used three methods for the time evolution of the beads: PIMD, CMD [37–40], and RPMD [41,42]. They are very different conceptually as PIMD can only calculate static properties whereas CMD and RPMD are designed to calculate dynamic properties based on different concepts from each other. In the formulation, however, only the choice of the fictitious mass (m_f) of the beads and the use of thermostats differ among them[43]. For more information about the choice of mass, see Ref. [43]. Finally, classical equations of motion are applied to the dynamics of the beads as

shown in Eq. 2.2-4.[43]

$$m_f^{(s)}\ddot{q}^{(s)} = -\frac{\partial}{\partial q^{(s)}} \sum_{s=1}^{n_{bead}} \left[\frac{1}{2}m_f^{(s)}\omega_P^2\left(q^{(s)} - q^{(s+1)}\right)^2 + \frac{1}{P}V_{ph}\left(q^{(s)}\right)\right] \qquad \text{Eq. 2.2-4}$$

In this study, PIMD was used for equilibration before CMD and RPMD simulations and for free energy profiles in the application of PI-QTST methods. RPMD without a thermostat and adiabatic CMD were employed to collect real-time trajectories of H. The PIMD code [44] was used for all PI calculations.

3. MTP generation and validation

3.1. MTP generation

For each bcc metal, MTPs were trained to reproduce the PESs of DFT in the position space relevant to hydrogen dynamics. The DFT calculations for energy, force, and stress were performed with the Vienna Ab initio Simulation Package (VASP) [45–47]. The Perdew-Burke-Ernzerhof functionals [48] were used to describe the electron exchange-correlation. The total energy was sampled on a Γ-centered $6 \times 6 \times 6$ k-point grid by the Monkhorst and Pack scheme [49] with a 650 eV energy cutoff. Spin-polarized calculations were performed for the systems of Fe, but not for the systems of W because their electronic ground states are nonspin polarized.

The procedure for MTP generation involved supervised learning with molecular statics calculations and active learning by CLMD and PIMD. First, to obtain an accurate and stable description of key kinetic and thermodynamic properties for hydrogen diffusion, the molecular statics configurations were prepared from (1) random deformation of unit bcc cells, (2) stable structures for dissolved hydrogen, (3) snapshots in nudged elastic band (NEB) calculations [50] for hydrogen migration, and (4) finite-displacement structures for quasiharmonic approximation (QHA) calculations. Second, the accuracy and stability of MTPs were strengthened through active learning with classical NPT ensembles. The machine learning interatomic potential (MLIP) package [35], invented by Novikov et al., was used to determine the extrapolation grade of configurations, reinforce the training sets, and reoptimize MTP parameters. The maximum temperature in active learning with CLMD was approximately two-thirds of the melting temperature of pure bcc metals. Finally, training was completed by active learning using PIMD with NVT ensembles to incorporate the configuration of beads. MTP level was set to 16 for all metals, and the maximum cutoff radius was set to 5.5 Å for the Fe–H system and 6.0 Å for the W–H systems. More details of the training sets and active learning are explained in Section A2 of the Appendix. The training sets and the MTP parameters used in this study are available in Ref. [51].

38

3.2. MTP validation
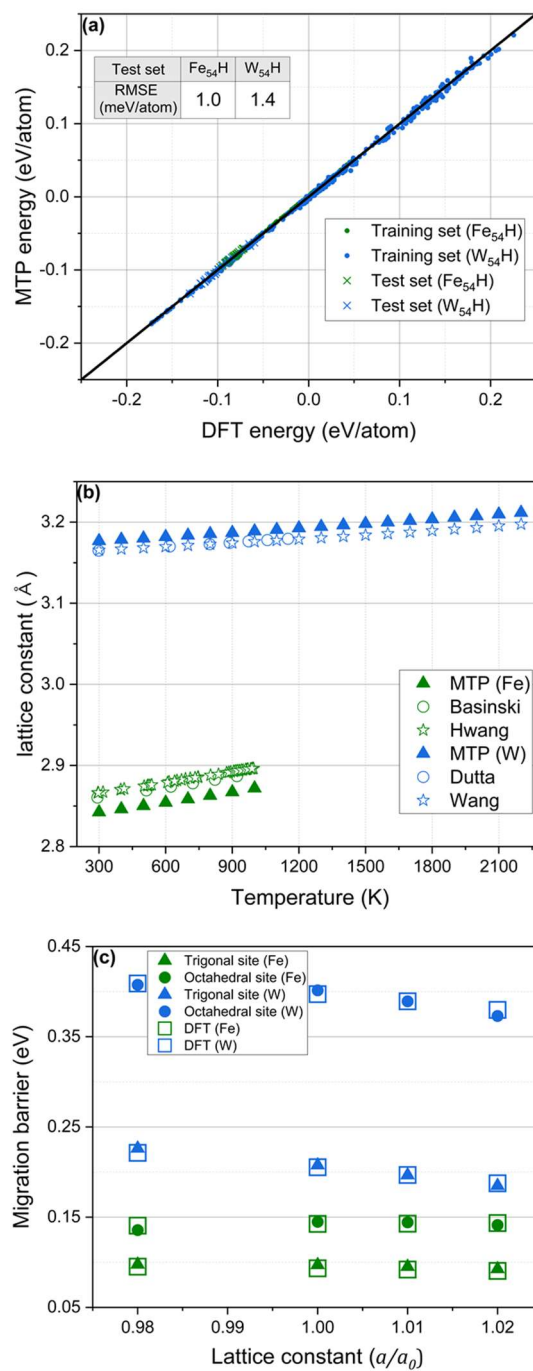
Fig. 3.2-1 Validation of generated MTPs. (a) Scatter plots of energies for training

and test sets calculated using DFT and MTPs; (b) Equilibrium lattice constants at 1 bar estimated by CLMD. Experimental data were obtained from Ref. [52,53] for Fe, and Ref. [54,55] for W. Ref. [55] was from a statistical analysis of available experimental data. (c) Hydrogen migration barriers at different lattice constants (a). a_0 denotes a lattice constant from geometry optimization. The LAMMPS code was used for the classical atomistic simulations.

The energy, force, and stress data from DFT fit well with the MTPs. For example, good agreement in energy is confirmed in Fig. 3.2-1(a), which compares the energies calculated on the training and test sets using DFT and MTPs.

The lattice constants, lattice thermal expansion, and elastic constants were examined for pure bcc metals. Lattice constants from geometry optimization showed an error of 0.02% at most in reference to DFT, and an absolute error of 0.02 Å ∼ 0.03 Å from the experiments after correction of the zero-point vibration effect [56]. The thermal expansion coefficients calculated by CLMD were nearly identical to those of the experiments above 300 K [52–55,57], where quantum effects can be ignored, as shown in Fig. 3.2-1(b). The elastic constants were also reasonably reproduced; errors with respect to DFT were all less than 10% and the absolute differences from experiments [58–60] were 25 GPa at most. The lattice constants and elastic constants are provided in Section A3 of the Appendix.

Fig. 3.2-1(c) shows that the migration barriers obtained by the MTPs are similar to those obtained by DFT, including the effect of isotropic lattice deformation (-2% ∼ 2% strain), which is related to the temperature dependence of the barriers due to thermal expansion. The errors from DFT calculations were less than 5% for a path via a trigonal site or via an octahedral site. In addition, errors in the normal mode frequencies related to H were less than 6% for the tetrahedral site (ground state), trigonal site (1st-order transition state), and octahedral site (2nd-order transition state), as shown in Table 3.2-1. The frequencies of all vibrational modes are plotted in Section A3 of the Appendix, also showing good correspondence between the MTP and DFT data.

40

In summary, the validation test results demonstrate that MTP can achieve DFT accuracy for PESs and properties related to lattice mechanics/dynamics and hydrogen migration in bcc metals.

Table 3.2-1 Normal mode frequencies related to H. The value in parenthesis denotes the error from the DFT calculation ($(\nu_{MTP} - \nu_{DFT})/\nu_{DFT}$) in percent (%). i indicates an imaginary mode.

Unit: THz	Fe	W
Tetrahedral site	30.2 (3.25)	35.2 (0.95)
	44.0 (0.61)	47.3 (1.48)
	44.0 (0.61)	47.3 (1.48)
Trigonal site	20.4i (4.29)	25.7i (1.00)
	34.6 (-0.30)	46.0 (0.73)
	57.8 (-1.39)	63.2 (0.51)
Octahedral site	17.5i (0.56)	27.8i (5.68)
	17.5i (0.56)	27.8i (5.68)
	63.7 (-2.75)	75.5 (0.38)

4. Hydrogen diffusivity

4.1. Diffusion coefficient calculations

4.1.1. Einstein relation

The Einstein relation between the mean square displacement and diffusion coefficient at three-dimensions is expressed as

$$D = \lim_{t \to \infty} \frac{\overline{|\boldsymbol{r}_{cent}(t)|^2}}{6t}, \qquad\qquad \text{Eq. 4.1-1}$$

where $\overline{|\boldsymbol{r}_{cent}(t)|}^2$ represents the mean square displacement of a centroid. The diffusion coefficient can be determined in the framework of molecular dynamics with a reasonably large t value as

$$D \cong \frac{\overline{|\boldsymbol{r}_{cent}(t)|^2}}{6t}. \qquad\qquad \text{Eq. 4.1-2}$$

4.1.2. Path integral quantum transition state theory

A general concept of PI-QTST was established by Gillan [61], and it was combined with the minimum free energy path by Schenter et al. [62]. Althorpe and Richardson [63] further developed it by connecting PI-QTST to semiclassical instanton theory. For a reaction of interest, the PI-QTST method requires the free energy profile which can be obtained by integrating the mean force along a minimum energy path [61]. The mean force can be approximately taken during bead sampling while the centroid positions of atoms are fixed along the minimum energy path of reaction. The combined reaction constant [63–66] is expressed as

$$\Gamma_{PI-QTST}(T) \cong \alpha(T) \sqrt{\frac{1}{2\pi\beta m^*}} \frac{e^{-\beta F(q^*,T)}}{\int_{q_2^*}^{q_1^*} dq \, e^{-\beta F(q,T)}} \qquad\qquad \text{Eq. 4.1-3}$$

$$\alpha(T) = min\left[1, \frac{2\pi}{\beta\hbar\omega_b(T)}\right] \qquad \text{Eq. 4.1-4}$$

$$\omega_b(T) = \sqrt{\frac{|F''(q^*,T)|}{m^*}}, \qquad \text{Eq. 4.1-5}$$

where q is a reaction coordinate and q^* denotes a barrier top. q_1^* and q_2^* are adjacent barrier tops. $F(q,T)$ is the free energy at the reaction coordinate q and temperature T. ω_b is the absolute value of the imaginary angular frequency of the normal mode at the barrier top q^*. m^* is the effective mass of the diffusing particle along the reaction path [20]. For the migration of hydrogen through trigonal sites of the bcc lattice of Fe and W, the difference between the effective mass and its physical mass of hydrogen was approximately 4%. $T_{instanton}$ is a crossover temperature below which deep tunneling dominates the reaction rate [63].

$$T_{instanton} = \frac{\hbar\omega_b(T_{instanton})}{2\pi k_b} \qquad \text{Eq. 4.1-6}$$

The interstitial atomic diffusion coefficient is analytically expressed for three dimensions as

$$D = \frac{1}{6}n_{jump}f_{jump}\lambda_{jump}^2\Gamma, \qquad \text{Eq. 4.1-7}$$

where Γ is a jump rate. For hydrogen diffusion in a bcc metal, the dominant migration paths are jumps between tetrahedral sites: $n_{jump} = 4$ and $\lambda_{jump} = \frac{\sqrt{2}}{4}a$ where a is the lattice constant. Consequently, assuming there is no jump correlation, namely, $f_{jump} = 1$, the diffusion coefficient can be calculated as

$$D_{PI-QTST}(T) = \frac{a^2}{12}\Gamma_{PI-QTST}(T). \qquad \text{Eq. 4.1-8}$$

43

4.2. Validation by H diffusivity
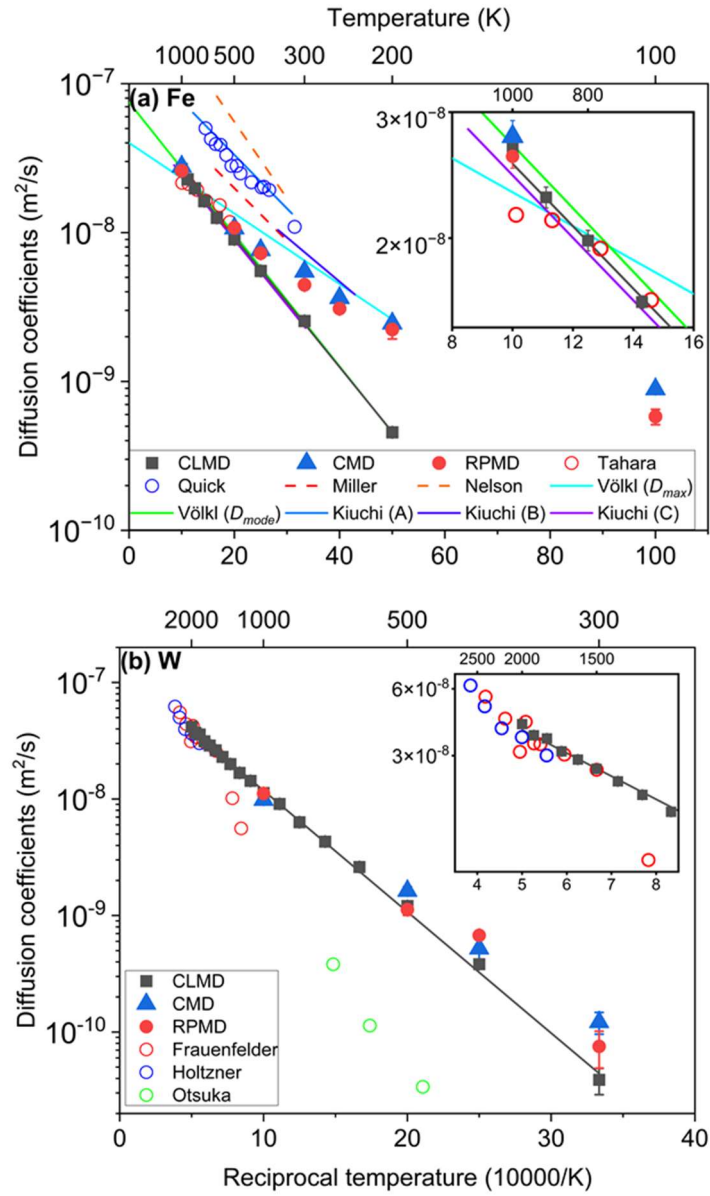
Fig. 4.2-1. H diffusivity in (a) Fe, and (b) W. The black solid line connecting CLMD plots denotes fitted Arrhenius equations. The error bars represent standard errors. The experimental data were obtained from Ref. [6,18,67–70] for Fe, and Ref. [7,8,71] for W. The simulation conditions of CLMD, CMD, and RPMD are enumerated in Section A4 of the Appendix.

Fig. 4.2-1 shows Arrhenius plots of the H diffusion coefficients for each material from the CLMD, CMD, and RPMD calculations and some experimental data. The differences between the CMD and RPMD results were minimal in all cases. The overall similarity demonstrates that the conceptual difference between the two methods does not lead to incompatible results, as also observed in a previous study [72]. In addition, their results converged to those of the CLMD above approximately 500 K, explained by the classical limit of quantum dynamics.

4.2.1. H diffusivity in bcc Fe

For Fe, the deviation in the previous experimental data was too large for direct comparison with the simulation results. Thus, we made a comparison with the recommended empirical equations obtained by Völkl and Alefeld [69] and Kiuchi and McLellan [6] by fitting many experimental results. Völkl suggested two plausible Arrhenius equations based on the highest value (D_{max}) and amount of data (D_{mode}). The former is based on the assumption that the surface and trapping effects are responsible for slowing the diffusion [69]. These two equations intersect at approximately 800 K. The CLMD/CMD/RPMD results were at the intersection, and agreed with D_{mode} above 800 K. The CMD/RPMD results were also reasonably consistent with D_{max} in the temperature range of 300 K $\sim$ 500 K. Nevertheless, we consider the reliability of Völkl's equations to be limited because Arrhenius equations are not valid in such a broad temperature range (200 K $\sim$ 1000 K) due to NQEs, as indicated by the current and previous [73] RPMD/CMD simulations.

Kiuchi organized experimental data based on the methods and conditions, and fitted each with an Arrhenius equation in a narrow temperature range: Group A (Pd-coated, ultrahigh vacuum, H_2-gas equilibration), Group B (electrochemical), and Group C (H_2-gas equilibration without a coating) [6]. Kiuchi considered Group A to be the most reliable group because the surface effects were expected to be attenuated

45

by attaching a Pd coating to the specimens. However, the reliability of Group A is still dubious because it was composed of only three datasets (Miller et al. [67], Nelson et al. [68], Quick et al. [70]), of which Miller indirectly determined H diffusivity from the ratio of measured permeability to solubility reported by others. Furthermore, the fact that the three datasets showed large deviations among Group A, as shown in Fig. 4.2-1(a), cast doubt on the effectiveness of the Pd coating in determining the true diffusivity in the lattice. A theoretical study analyzing the characteristics of the time-lag method in multiple laminates has shown that the effective diffusion coefficient determined by the time-lag method is affected by the thickness and H diffusion coefficients in the coatings [74]. Such effects did not appear to have been considered by Nelson and Quick.

Thus, acknowledging that there is room for other interpretations, we consider that Kiuchi's Group C equation (H_2-gas equilibration without a coating) above 500 K and Völkl's D_{mode} equation above 500 K, which are in close agreement, are the most reliable experimental data available. The following two points support our findings. First, the experimental data above 500 K show a relatively small variation if the Pd-coating data are ignored, as shown in Fig. 8 of Kiuchi's study [6]. Second, it has been estimated that the effect of surface processes is negligible above approximately 500 K [75]. The CLMD/CMD/RPMD results agreed well with the experimental data above 500 K.
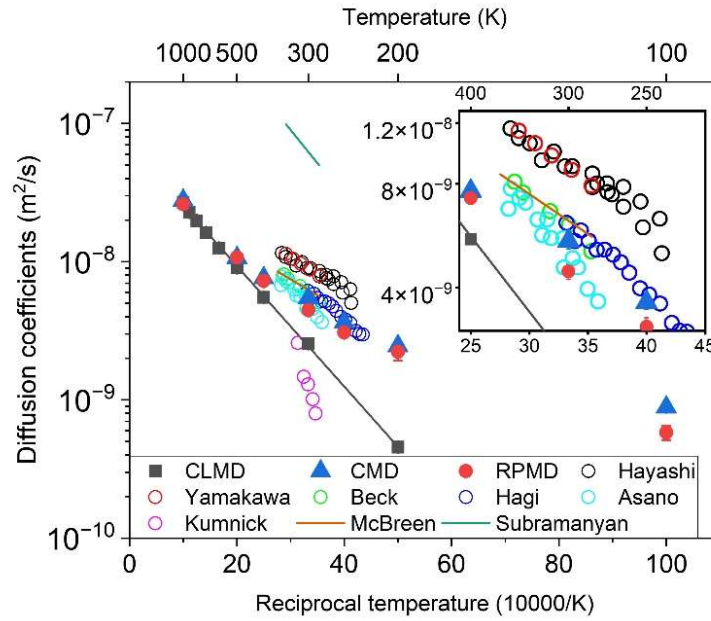
Fig. 4.2-2 Comparison of H diffusivity in Fe for current simulation results and experimental values obtained by electrochemical techniques. The black solid line connecting CLMD plots denotes the fitted Arrhenius equation. The error bars of CLMD/CMD/RPMD plots represent standard errors. The experimental data were obtained from Ref. [76–83]. The Arrhenius equations of McBreen [82] and Subramanyan [83] were taken from Table 2 of Kiuchi's study [6] due to inaccessibility to the original literature.

Below 500 K, Kiuchi showed that the diffusion coefficients determined by gas equilibrium methods such as permeation, desorption, and time-lag methods varied by several orders of magnitude or more, whereas those determined by electrochemical methods varied relatively little in the temperature range of 250 K ~ 350 K [6]. In Fig. 4.2-2, excluding two data sets (Kumnick [81] and Subramanyan [83]), the variation in the electrochemical measurements is half an order of magnitude, and the CMD/RPMD calculations agree with the measurements within that variation range.

47

4.2.2. H diffusivity in bcc W

For bcc W, the H diffusion coefficients reported by Frauenfelder [7] and Holzner et al. [71] are comparable to the CLMD results above 1500 K. Frauenfelder fitted the Arrhenius equation in the temperature range of 1100 K ~ 2500 K for H diffusion coefficients determined by degassing experiments [7]. Heinola and Ahlgren reinterpreted Frauenfelder's data and suggested that the appropriate fitting region should be 1500 K ~ 2500 K to exclude the trapping effects [14]. Subsequent theoretical and computational studies have confirmed that trapping effects due to vacancies or grain boundaries can explain the deviation in diffusion coefficients below 1500 K [13,15].

4.2.3. Arrhenius equations of H diffusivity
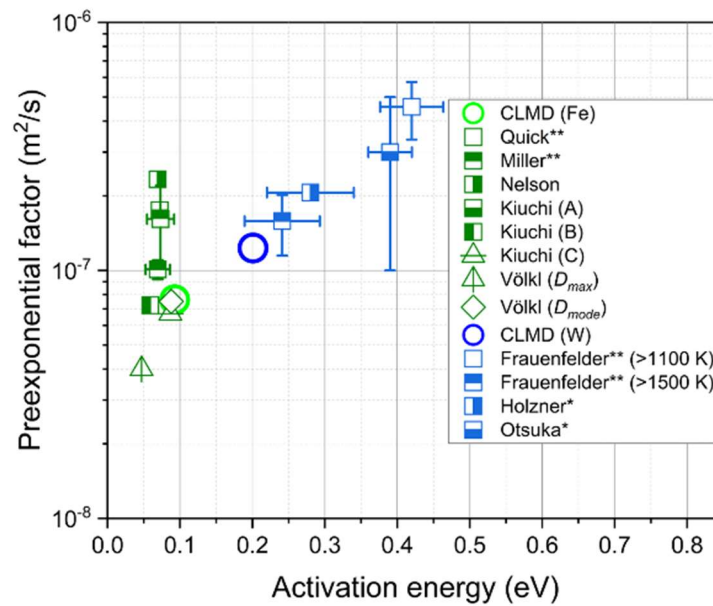
Fig. 4.2-3 Activation energies and preexponential factors of Arrhenius equations of H diffusivity. The current CLMD results and previous experimental studies presented in Fig. 4.2-1 are plotted. In the legend, '*' indicates data that were reported with a standard error of the activation energy, and '**' indicates data that were reported with standard errors of both pre-exponential factor and activation

energy. The standard errors in the current CLMD results are negligible.

Fig. 4.2-3 presents the pre-exponential factors and activation energies of the Arrhenius equations for H diffusion obtained by CLMD for the three materials, together with some experimental results. As the CLMD results were used, the calculation results in Fig. 4.2-3 represent the diffusivity at temperatures above 500 K, where the NQEs are negligible. Völkl's D_{mode} for Fe, and Kiuchi's Group C data for Fe agreed well with the corresponding CLMD results. As discussed above, these experimental data are considered reliable at high temperatures.

For W, although the Arrhenius plots in Fig. 4.2-1(b) show good agreement between the current calculation and the data of Frauenfelder [7] and Holzner [71], the derived Arrhenius equations are inconsistent, as shown in Fig. 4.2-3. The inconsistency arises from the large variation in the experimental measurement, as seen in Fig. 4.2-1(b). At high temperatures, the data interval for the reciprocal temperature scale is short; thus, the fitting error in the Arrhenius plot can easily become large if the measurement variation is large. In our estimate, the fitting error in the activation energy was 0.05 eV as the standard error of linear fitting of the Arrhenius plot of Frauenfelder's data above 1500 K; Holzner et al. reported a fitting error in the activation energy of 0.06 eV. In contrast, because the Arrhenius equation for the CLMD results was obtained over a wider temperature range, the estimated deviation in the CLMD data was only 0.003 eV. Considering these statistical errors, the Arrhenius equation from the current CLMD is more precise than those from Frauenfelder's and Holzner's data.

In summary, although the large deviation in experimental data makes it difficult to validate the calculation results, in temperature ranges where the reliability of experimental data is considered to be high (>500 K for Fe, and >1500 K for W), the current calculation shows excellent agreement with experiments for Fe and W.

4.3. NQEs, dynamic effects, and isotope effects

   4.3.1. Free energy barriers

       Although the simulation speed of PIMD with MTP is much higher than that
of AI-PIMD, applying CMD and RPMD to the Einstein relation at very low
temperatures is still demanding. Additionally, the calculation for heavier isotopes is
difficult because NQEs are less considerable in D or T migration; thus, their diffusion
coefficients are not as large as those of H. To provide a reasonable estimate including
NQEs, even when the diffusion coefficient is too low, we adopted PI-QTST.
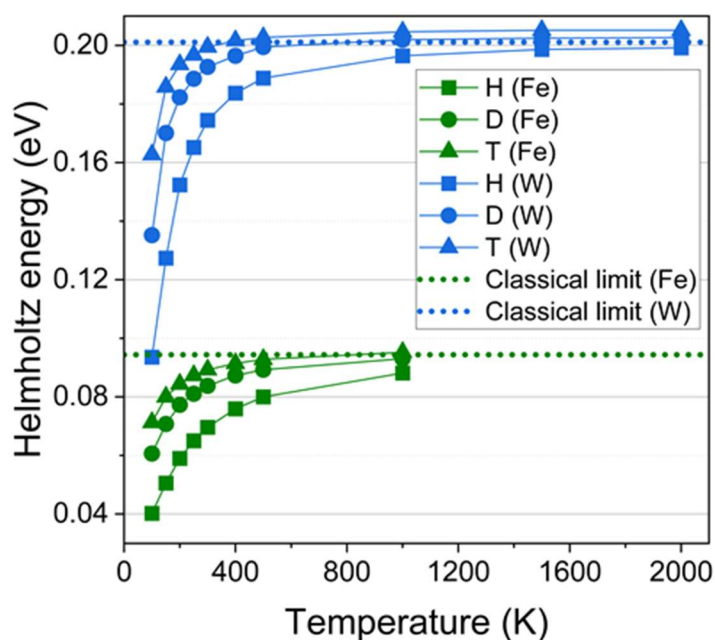
Fig. 4.3-1 Temperature-dependent free energy barriers for migration of
hydrogen isotopes in Fe and W through trigonal site. Simulation conditions are
enumerated in Section A4 of the Appendix.

       Several assumptions were made to simplify the PI-QTST process. First, jumps
through octahedral sites were ignored because they rarely occur compared to jumps
through tetrahedral sites. Second, the one-dimensional minimum free energy path for

50

hydrogen migration was assumed to be identical to the classical path. This assumption is likely to be valid, as Kimizuka et al. reasonably reproduced the quantum behavior of hydrogen in fcc metals over a wide temperature range of 75 K ~ 1200 K [24]. Finally, the thermal expansion effects were neglected for simplicity; thus, a geometry-optimized lattice constant was used to construct the supercells. In some test cases, we confirmed that the effect of thermal expansion was not significant.

Fig. 4.3-1 shows the temperature-dependent free energy barriers obtained by the PI-QTST method using Eq. 4.3-1,

$$\Delta F(T) = - \int d\boldsymbol{s} \cdot \boldsymbol{f_{mean}}(\boldsymbol{q}, T), \qquad \text{Eq. 4.3-1}$$

where $\Delta F(T)$ is the free energy barrier at temperature T, $\boldsymbol{q}$ is the reaction path, and $\boldsymbol{f_{mean}}(\boldsymbol{q}, T)$ is the mean force acting on the beads when the centroid is fixed at $\boldsymbol{q}$ [61]. As theoretically expected, the free energy barriers decreased as the temperature fell due to NQEs, and the NQEs were more pronounced for lighter isotopes.

4.3.2. Dynamic effects and NQEs
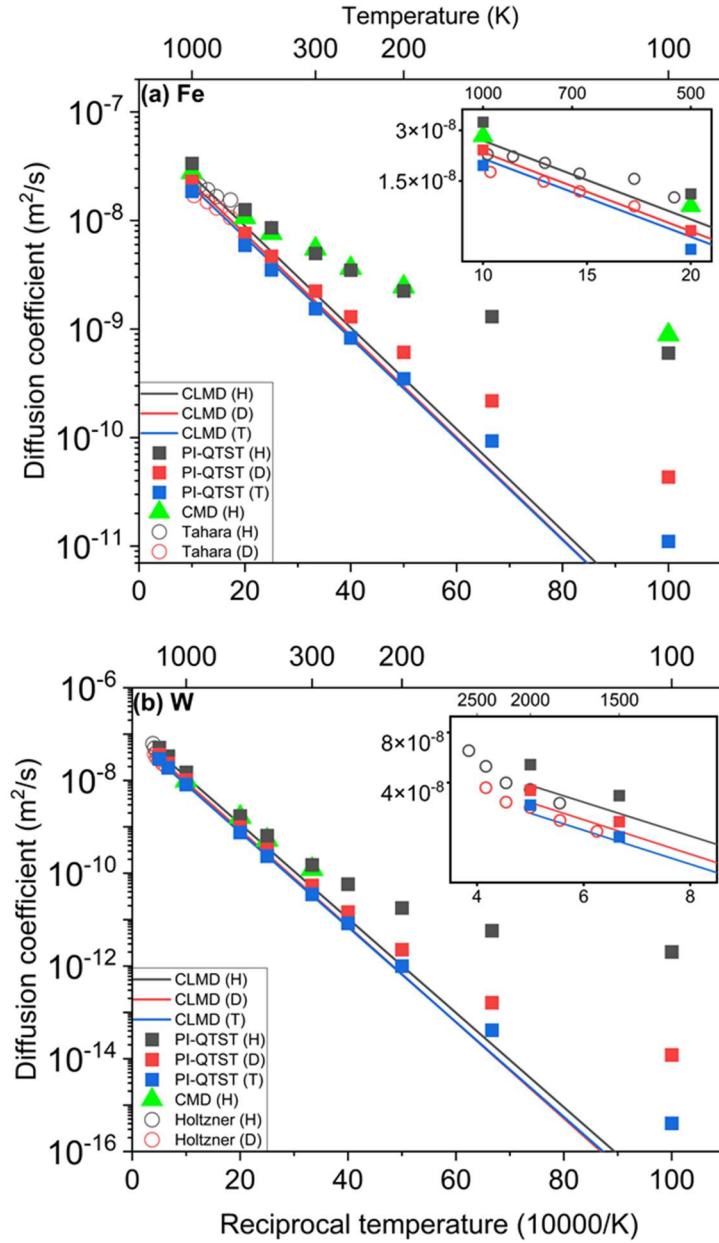
Fig. 4.3-2 Hydrogen diffusivity in (a) Fe, and (b) W. RPMD results are not plotted because diffusivity differences between CMD and RPMD are small in comparison with their standard errors. Experimental data were obtained from Ref. [18] for Fe and Ref. [71] for W.

Fig. 4.3-2 (a) ~ (b) show the diffusion coefficients of H, D, and T calculated by PI-QTST using Eq. 4.1-3 and Eq. 4.1-8, together with those calculated by CLMD, the H diffusion coefficients calculated by CMD, and the experimental results for the three isotopes. The H diffusion coefficients calculated by PI-QTST showed good agreement with the CMD results at low temperatures, whereas relatively large differences were observed at high temperatures. For example, there was a ~50% difference from the CMD results at 1000 K for W.

The high-temperature discrepancy between PI-QTST and CMD is the result of dynamic effects. Although the dynamic effects are fully considered in CMD, recrossing is neglected in PI-QTST because a centroid position of each atom is fixed during bead sampling. We estimated the crossover temperature of the dynamic effects, $T_{dynamic}$, from the transmission coefficient (τ), which is defined as $\tau = D_{CMD}/D_{PI-QT}$. Fig. 4.3-3(a) shows the temperature-dependent transmission coefficients of H diffusivity in Fe and W. Generally, τ is less than 1 due to recrossing, as shown in Fig. 4.3-3(a). $\tau = 1$ means that the crossing event is not disturbed by phonons and that dynamic effects are negligible. Although the uncertainty in W is large owing to the large standard errors in D_{CMD}, we approximate $T_{dynamic}$ to be 300 K for all metals. Our suggested $T_{dynamic}$ is consistent with the study of Paxton and Katzarov [84], which revealed that the transmission coefficient of H diffusion in Fe can be approximated as 1 below 300 K by QTST using the magnetic tight binding model [85]. PI-QTST can be an accurate alternative to CMD/RPMD for estimating the H diffusivity below $T_{dynamic}$.

Furthermore, at very low temperatures, below $T_{instanton}$ as defined by Eq. 4.1-6, the PI-QTST can theoretically be more accurate than the CMD/RPMD. This is because the contribution of deep tunneling, which CMD/RPMD cannot describe properly and, in contrast, PI-QTST considers with the instanton theory, starts to increase below $T_{instanton}$ [86]. For H diffusivity, $T_{instanton}$ was approximately 100

K and 200 K in Fe and W, respectively.

However, at temperatures above the crossover temperature of NQEs, T_{NQEs}, above which the NQEs are negligible, CLMD can be the best alternative. Fig. 4.3-3(b) shows D_{CMD}/D_{CLMD} to estimate T_{NQEs}. Regardless of the metal, T_{NQEs} in H diffusivity was approximately 500 K, and was higher than $T_{dynamic}$.
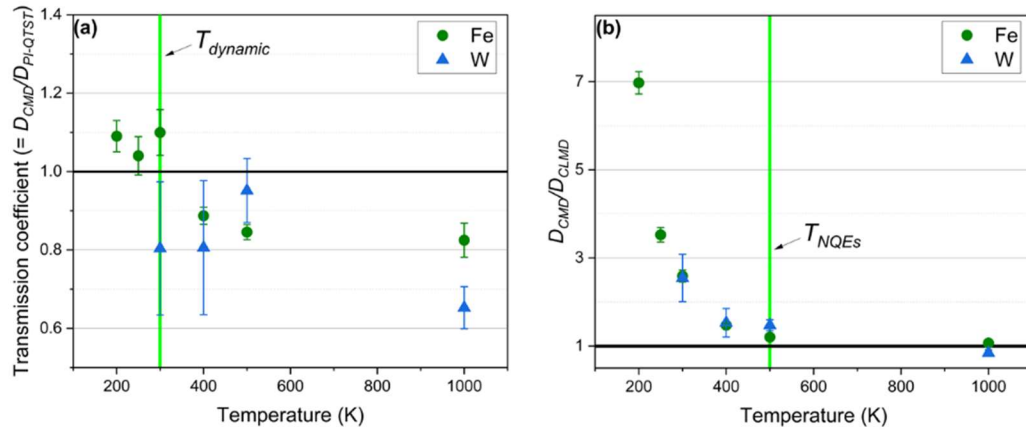
Fig. 4.3-3 (a) Dynamic effects of H diffusivity in Fe, and W. The transmission coefficients are defined as $\boldsymbol{D_{CMD}/D_{PI-QTST}}$. (b) NQEs on H diffusivity in Fe, and W.

Fig. 4.3-4 illustrates the key factors that affect hydrogen diffusivity and the temperature range over which each method can accurately determine the diffusion coefficient. PI-QTST and CLMD are accurate below $T_{dynamic}$ and above T_{NQEs}, respectively. In the temperature range between $T_{dynamic}$ and T_{NQEs}, estimated to be 300 K ~ 500 K for H in the three metals, there is no accurate alternative to CMD/RPMD.
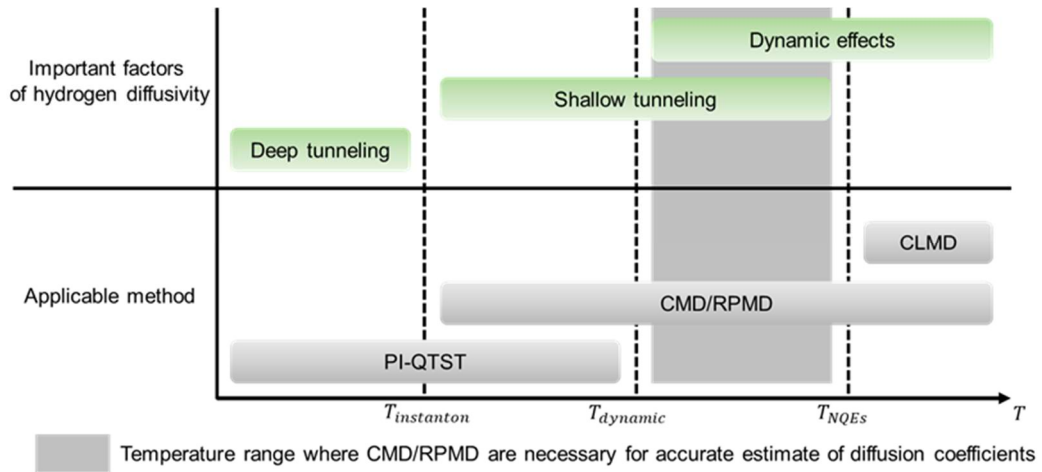
Fig. 4.3-4 Key factors affecting hydrogen diffusion coefficients and applicable methods in corresponding temperature ranges.

4.3.3 Isotope effects

For the heavier isotopes (D and T), the temperature ranges of $T_{dynamic} < T < T_{NQEs}$ are approximately within that of H for the following reasons. First, Paxton and Katzarov confirmed that the transmission coefficients are weakly dependent on isotopes [84]. Thus, $T_{dynamic}^D$ and $T_{dynamic}^T$ were considered comparable to $T_{dynamic}^H$. Second, T_{NQEs}^D and T_{NQEs}^T are generally lower than T_{NQEs}^H due to the heavier atomic masses of D and T, as confirmed by Qi's experiments [21]. Thus, it is justifiable to determine the isotope effects below 300 K using PI-QTST and above 500 K using CLMD for Fe and W. Fig. 4.3-5 shows the isotope effects of hydrogen diffusivity calculated using PI-QTST and CLMD.
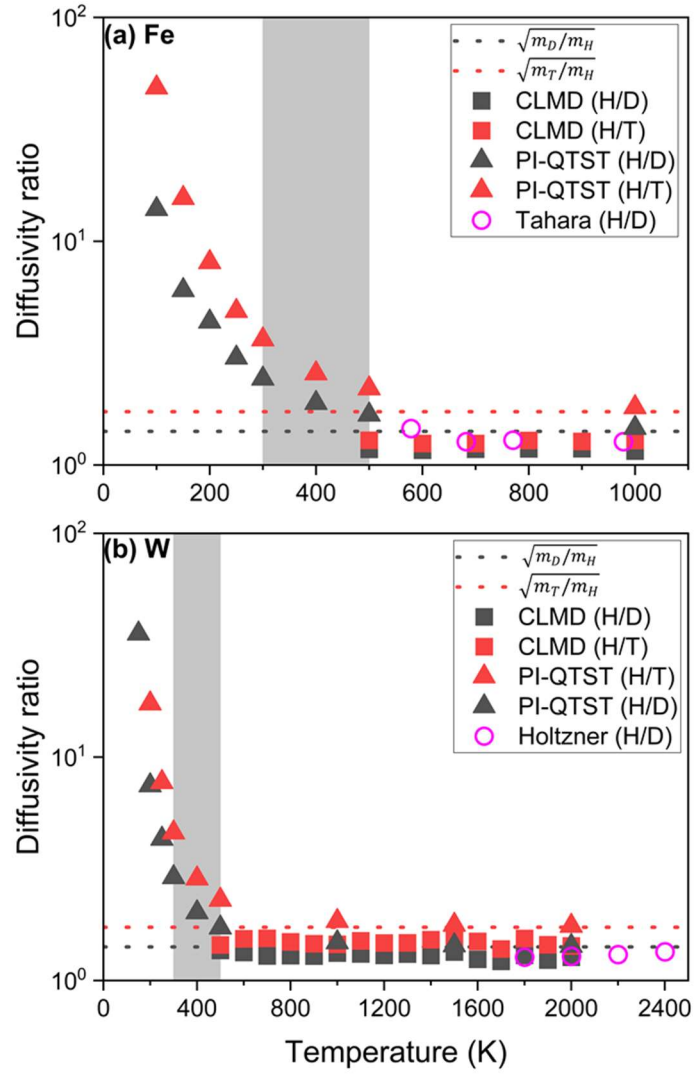
Fig. 4.3-5 Hydrogen isotope effects in (a) Fe and (b) W. "H/D" and "H/T" denote D_H/D_D and D_H/D_T, respectively. In (a), the solid lines are from the cubic spline method. $\sqrt{m_D/m_H}$ and $\sqrt{m_T/m_H}$ are the theoretical diffusivity ratios proposed by the classical rate theory under harmonic approximation conditions. Experimental data were obtained from Ref. [18] for Fe and Ref. [71] for W. The gray regions denote the temperature ranges in which both PI-QTST and CLMD results are less accurate.

In experiments on bcc metals, H diffusion has always been faster than D

56

diffusion, and significant temperature dependence of the isotope effects has been observed [69].

For Fe, experimental data on H diffusivity are scattered; thus, it is difficult to estimate the isotope effects with high accuracy. Although isotope effects have been obtained below 500 K in several studies [87,88], we do not refer to these experimental data because they likely do not reflect the true diffusion coefficient in the lattice, as discussed in Section 4.2.1. The isotopes data of Tahara and Hayashi [18] seem to be reasonably accurate because the H diffusivity obtained above 580 K shows good agreement with Kiuchi's Group C and Völkl's D_{mode} equation, which we verified to be the most reliable above 500 K. In Tahara's study, the isotope effect between H and D at high temperatures did not converge to the square root of the mass ratio [18], as expected in classical rate theory [20], but became smaller. The CLMD results reproduced this trend, as shown in Fig. 4.3-5(a).

For W, isotope effects between H and D were reported by Holzner et al. [71] at 1800 K ∼ 2600 K, where NQEs and trapping effects were negligible. As shown in Fig. 4.3-5(b), the isotope effects calculated by CLMD were consistent with those of Holzner. This consistency further demonstrates that MTPs can accurately describe the isotope effects in hydrogen diffusion.

4.3.4 Isotope effects in the classical regime, $T > T_{NQEs}$

A disparity in isotope effects from the classical rate theory was observed for Fe and W, even above 500 K, at which the NQEs can be ignored as $T > T_{NQEs}$. In Fig. 4.3-2(a) ∼ (b), the slopes of the Arrhenius plots obtained from CLMD are almost independent of the isotopes. Thus, at temperatures above T_{NQEs} where hydrogen behaves as a classical particle, the Arrhenius equations for hydrogen isotopes differ only in the pre-exponential factor and not in the activation energy. The parameters of the Arrhenius equations derived from the CLMD in Fig. 4.3-2 are presented in Table 2. As the activation energy is almost isotope-independent, the isotope effect can be

57

quantified from the ratio of the pre-exponential factors, with smaller values than those from classical rate theory. For example, the diffusivity ratio of H to T in bcc Fe obtained by CLMD is 1.28, whereas $\sqrt{m_T/m_H}$ is 1.73. We consider that dynamic effects such as anharmonicity and recrossing caused the difference from classical rate theory, although the mechanism is a subject for future research.

Table 4.2-1 Parameters of Arrhenius equations for hydrogen isotope diffusivity from CLMD. D_0 denotes the pre-exponential factors of the Arrhenius equations.

	Fe	W
Activation energy (meV)	92.7 ± 3.6	203 ± 6
$D_0^H \ (10^{-8} m^2 s^{-1})$	7.62 ± 0.2	12.3 ± 0.5
D_0^H/D_0^D	1.16 ± 0.06	1.26 ± 0.07
D_0^H/D_0^T	1.28 ± 0.05	1.43 ± 0.09

5. Hydrogen solubility

5.1. Solution constant calculations

  5.1.1. Solubility at dilute concentration limit

Under the chemical equilibrium at dilute hydrogen concentration limit for an isothermal-isobaric condition of a closed system, namely, NPT ensemble, the change of Gibbs free energy is zero in terms of hydrogen transfer between the hydrogen gas and the hydrogen solute state.

$$G_{sol}(N_H, N_M, P_{H_2}, T) = H_{sol}(N_H, N_M, P_{H_2}, T) - TS_{sol}(N_H, N_M, P_{H_2}, T)$$
$$= 0$$

Eq. 5.1-1

The solution entropy (S_{sol}) is the sum of the configurational (S_{sol}^c) and non-configurational (S_{sol}^{nc}) terms. The former only depends on the numbers of hydrogen atoms (N_H) and their stable sites (N_{site}) in the lattice.

$$S_{sol}^c(N_H, N_{site}) = k_B \ln\left(\frac{N_{site}!}{N_H!\,(N_{site}! - N_H!)}\right)$$

Eq. 5.1-2

For bcc metals, $N_{site} = 6N_M$ as the tetrahedral sites are the most stable interstitial sites for hydrogen. At the dilute concentration limit $(N_H \ll N_M)$, Stirling's approximation can be applied to the logarithm in Eq. 5.1-2.

$$\ln\left(\frac{N_{site}!}{N_H!\,(N_{site}! - N_H!)}\right) \cong -\ln\left(\frac{N_H}{N_{site} - N_H}\right) \cong -\ln\left(\frac{N_H}{N_{site}}\right)$$
$$= -\ln\left(\frac{N_H}{6N_M}\right) = -\ln\left(\frac{\theta}{6}\right)$$

Eq. 5.1-3

Consequently, the hydrogen solubility (θ) in bcc metals is expressed by solution enthalpy (H_{sol}) and non-configurational solution entropy (S_{sol}^{nc}).

$$H_{sol}(N_H, N_M, P_{H_2}, T)$$

$$= H_{H+M}(N_H, N_M P_{H_2}, T)$$

$$- \left[H_M(N_M, P_{H_2}, T) + N_H \times \frac{1}{2} h_{H_2}(P_{H_2}, T) \right]$$

Eq. 5.1-4

$$S_{sol}^{nc}(N_H, N_M, P_{H_2}, T) = S_{sol}(N_H, N_M, P_{H_2}, T) - S_{sol}^c(N_H, N_M)$$

$$= S_{H+M}(N_H, N_M, P_{H_2}, T)$$

$$- \left[S_M(N_M, P_{H_2}, T) + N_H \times \frac{1}{2} s_{H_2}(P_{H_2}, T) \right]$$

$$- S_{sol}^c(N_H, N_M)$$

Eq. 5.1-5

$$\theta(N_H, N_M, P_{H_2}, T)$$

$$= 6 \exp \left(\frac{S_{sol}^{nc}(N_H, N_M, P_{H_2}, T)}{k_B} \right) \exp \left(- \frac{H_{sol}(N_H, N_M, P_{H_2}, T)}{k_B T} \right)$$

Eq. 5.1-6

Thus, to calculate θ, we need to obtain the enthalpy term, H_{sol}, and the non-configurational entropy term, S_{sol}^{nc}.

5.1.2. Calculation of solution enthalpy (H_{sol})

According to Ref. [89], enthalpy at NPT ensembles is defined as a function of isobaric partition function.

$$H(N, P, T) := k_B T^2 \frac{1}{\Delta(N, P, T)} \left(\frac{\partial \Delta(N, P, T)}{\partial T} \right)_{N, P}$$

Eq. 5.1-7

where Δ is a weighted sum of the canonical partition functions.

$$\Delta(N, P, T) = \sum_V Q(N, V, T) e^{-\beta PV}$$

Eq. 5.1-8

There are two types of Finite Size Effects (FSEs). One is on the hydrogen-hydrogen interaction and the other is on the lattice expansion by dissolved-hydrogen. The former is not only about the direct interaction, which can be eliminated if the cell

length is larger than twice the cutoff radius of interaction, but also the indirect interaction via stress field generated around hydrogen, which is usually more long-ranged. We have found that the latter is significant at NPT ensembles because the lattice expansion induced by interstitial hydrogen, which should be negligible at the dilute limit, is significant if the supercell size is small. Although it is difficult to precisely quantify the FSEs in NPT-MD due to large fluctuations in energy and volume, rough estimation by the elastic theory would be sufficient to prove the large FSEs. Fig. 5.1-1 shows differences of equilibrium lattice constants between hydrogen - dissolved and pure bcc-W in NPT-CLMD at 500 K, which were calculated up to a $14 \times 14 \times 14$ supercell. For larger supercells, the 3rd order fitting was applied to extrapolate $\frac{1}{a_{H+W}-a_W}$ from the bulk modulus of tungsten (K_W) and hydrogen virial (W_{H+W}).

$$K_W = -V\frac{dP}{dV} \cong V_W \frac{-\Delta P}{V_{W+H} - V_W}$$

$$V_{H+W} = V_W \left(1 - \frac{\Delta P}{K_W}\right)$$

$$a_{H+W} = \frac{(V_{W+H})^{\frac{1}{3}}}{n} = a_W \left(1 - \frac{\Delta P}{K_W}\right)^{\frac{1}{3}}$$

$$a_{H+W} - a_W = a_W \left[\left(1 - \frac{\Delta P}{K_W}\right)^{\frac{1}{3}} - 1\right] \cong a_W \left(-\frac{1}{3}\frac{\Delta P}{K_W}\right) = \frac{a_W}{3K_W}\frac{W_{H+W}}{V_W}$$

$$= \frac{W_{H+W}}{3K_W n^3 a_W^2} \propto n^{-3}$$

Eq. 5.1-9

where n denotes a size of $(n \times n \times n)$ supercell. If the difference in the lattice constant $(a_{H+W} - a_W)$ can be approximated by a specific function as n grows, the internal energy change by the FSEs can be roughly estimated using the bulk modulus. Additional stress induced by the dissolved hydrogen in a lattice (ΔP) equals the hydrogen virial divided by lattice volume (V_W), so the appropriate fitting function of $(a_{H+W} - a_W)^{-1}$ is 3rd-order polynomial of n. Good agreement between this model

61

equation and MD results is seen in Fig. 5.1-1. Using this model equation, the internal energy change caused by lattice expansion in each supercell was estimated by Eq. 5.1-10, which is also shown in Fig. 5.1-1.

$$\Delta U(n)$$
$$\cong \frac{1}{2}\frac{K_W}{V_W(n)}\left(V_{H+W}(n) - V_W(n)\right)^2 \qquad \text{Eq. 5.1-10}$$
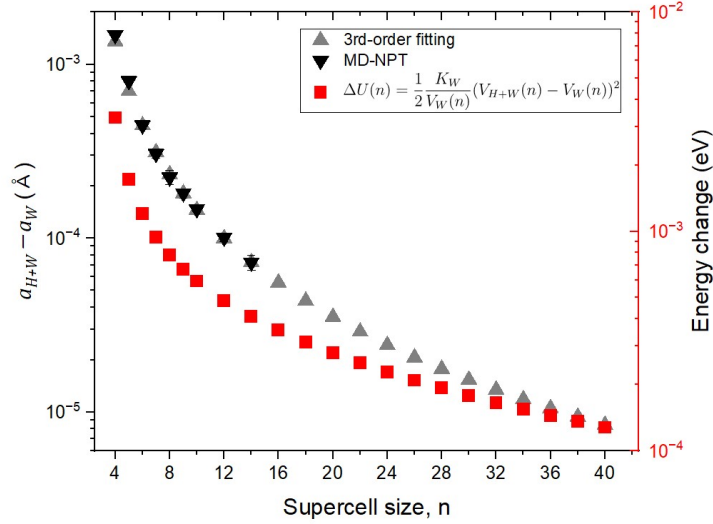
Fig. 5.1-1 (Left axis) Lattice constant difference between hydrogen-dissolved tungsten (a_{H+W}) and perfect tungsten (a_W) (Right axis) Energy change induced by the volume expansion. The standard error of the mean was estimated to be 7.4×10^{-6} Å for $(a_{W+H} - a_W)$ and 8.2×10^{-5} eV for ΔV in the $14 \times 14 \times 14$ supercell, for example. $K_W = 313$ **GPa** was determined from the strain-stress relation of the MTP for W.

According to the energy change trend in Fig. 5.1-1, approximately $7 \times 7 \times 7$ supercell is needed to make the energy change smaller than 0.001 eV from the value of $n \to \infty$, corresponding to the dilute limit. However, increasing the supercell size in NPT-MD is practically difficult because the magnitude of system energy fluctuation increases with the number of atoms, which necessitates longer simulation times to maintain the constant precision in enthalpy calculation.

Specifically, the standard error of the mean (SEM) of the system energy is proportional to $\sqrt{n^3}$, and thus the simulation length and total simulation cost of MD increase in proportional to n^3 and n^6, respectively, to achieve a constant precision. Note that the precision of the solution enthalpy is relevant with the SEM of the system energy, not the SEM of per-atom energy, which is proportional to $1/\sqrt{n^3}$.

Since it is impractical to adequately suppress both SEM and FSEs at NPT-MD, we propose an effective method that eliminates volume expansion effects by applying the same volume to both hydrogen-dissolved and pure lattice in NVT-MD with small supercells. In other words, the isothermal-isobaric partition function is approximated by a *representative* canonical partition function whose volume is an equilibrium one of the pure metals at the NPT ensembles.

$$V_{rep}(N_M, P, T) := \langle V \rangle^{NPT}(N_M, P, T) = \sum_V V \left[\frac{Q(N_M, V, T)e^{-\beta PV}}{\Delta(N_M, P, T)} \right] \qquad \text{Eq. 5.1-11}$$

The FSEs due to the lattice expansion are eliminated since hydrogen dissolution does not contribute to the expansion in this method. This approximation is likely valid under the dilute hydrogen concentration limits for the following two reasons. First, the equilibrium lattice constant difference between the hydrogen-dissolved and the pure metallic systems and the energy difference induced by the lattice expansion converge to zero as the system size grows, as clearly seen in Eq. 5.1-12 and confirmed in Fig. 5.1-1.

$$\Delta U(n)$$
$$\cong \frac{1}{2} \frac{K_W}{V_W(n)} (V_{H+W} - V_W)^2$$
$$= \frac{n^3 K_W}{2 a_W^3} \left[\left(a_W + \frac{W_{H+W}}{3 K_W n^3 a_W^2} \right)^3 - a_W^3 \right]^2$$
$$= \frac{n^3 K_W}{2 a_W^3} \left[\frac{W_{H+W}}{K_W} n^{-3} + O(n^{-6}) \right]^2$$

63

$$\therefore \Delta U(n) = O(n^{-3}) \qquad\qquad \text{Eq. 5.1-12}$$

Second, at thermodynamic limit $(N_M, \langle V \rangle^{NPT} \to \infty)$, both NPT ensemble with $\Delta(N, P, T)$ and NVT ensemble with $Q(N, \langle V \rangle^{NPT}, T)$ should produce the same solution enthalpy. Finally, in the NVT ensemble with $Q(N, \langle V \rangle^{NPT}, T)$, the regions that strongly interact with hydrogen contribute to the most of solution energy.

Thus, in this study, the isothermal-isobaric partition functions are approximated as Eq. 5.1-13 by using the canonical partition function of the equilibrium volumes that dominantly contribute to it.

$$\Delta\left(N_H, N_M, P_{H_2}, T\right) \cong \sum_V Q(N_H, N_M, V, T) e^{-\beta P_{H_2} V} \delta\left(V - V_{rep}\right)$$

$$\text{Eq. 5.1-13}$$

$$= Q\left(N_H, N_M, V_{rep}, T\right) e^{-\beta P_{H_2} V_{rep}}$$

$$H\left(P_{H_2}, T\right)$$

$$:= k_B T^2 \frac{1}{\Delta\left(P_{H_2}, T\right)} \left(\frac{\partial \Delta\left(P_{H_2}, T\right)}{\partial T}\right)_{P_{H_2}}$$

$$\cong \frac{k_B T^2}{Q\left(V_{rep}, T\right) e^{-\beta P_{H_2} V_{rep}}} \left(\frac{\partial Q\left(V_{rep}, T\right) e^{-\beta P_{H_2} V_{rep}}}{\partial T}\right)_{P_{H_2}}$$

$$= \frac{k_B T^2}{Q e^{-\beta P_{H_2} V_{rep}}} \left[\left(\frac{\partial Q}{\partial T}\right)_{P_{H_2}} e^{-\beta P_{H_2} V_{rep}} + Q \left(\frac{\partial e^{-\beta P_{H_2} V_{rep}}}{\partial T}\right)_{P_{H_2}}\right]$$

$$= k_B T^2 \left[\frac{1}{Q}\left(\frac{\partial Q}{\partial T}\right)_{P_{H_2}} + \frac{1}{e^{-\beta P_{H_2} V_{rep}}} \left(\frac{\partial e^{-\beta P_{H_2} V_{rep}}}{\partial T}\right)_{P_{H_2}}\right]$$

$$\frac{1}{Q}\left(\frac{\partial Q}{\partial T}\right)_{P_{H_2}}$$

$$= \frac{1}{Q}\left(\frac{\partial}{\partial T}\right)_{P_{H_2}} \sum_j e^{-\beta E_j}$$

64

$$= \sum_j \left(\frac{E_j}{k_B T^2} - \frac{1}{k_B T} \left(\frac{\partial E_j}{\partial T} \right)_{P_{H_2}} \right) \left(\frac{e^{-\beta E_j}}{Q} \right)$$

$$= \sum_j \left(\frac{E_j}{k_B T^2} - \frac{1}{k_B T} \left(\frac{\partial V}{\partial T} \right)_{P_{H_2}} \left(\frac{\partial E_j}{\partial V} \right)_{P_{H_2}} \right) \left(\frac{e^{-\beta E_j}}{Q} \right)$$

where E_j denotes internal energy of microstate j. Energy of each microstate in the canonical ensemble has nothing to do with P_{H_2}. In each microstate, fractional coordinates are fixed.

$$\left(\frac{\partial E_j}{\partial V} \right)_{P_{H_2}} = \left(\frac{\partial E_j}{\partial V} \right)_{\{x_i^j\}}$$

E_j is a function of position $\{q_i^j\}$ and momentum $\{p_i^j\}$ space, where each position (q_i^j) is defined as the product of volume length $(V^{\frac{1}{3}})$ and fractional coordinate (x_i^j).

$$E_j(\{q_i^j\}, \{p_i^j\}) = E_j \left(\{V^{\frac{1}{3}} x_i^j\}, \{p_i^j\} \right)$$

For the volume expansion of microstates, the fractional coordinates are fixed.

$$\left(\frac{\partial E_j}{\partial V} \right)_{\{x_i^j\}} = \sum_{3N} \left(\frac{\partial E_j}{\partial q_i^j} \right) \left(\frac{\partial q_i^j}{\partial V} \right) = \sum_{3N} \left(\frac{\partial E_j}{\partial q_i^j} \right) \left(\frac{1}{3} V^{-\frac{2}{3}} x_i^j \right) = \sum_{3N} (-f_i^j) \left(\frac{1}{3} V^{-\frac{2}{3}} x_i^j \right)$$

$$= -\frac{1}{3V} \sum_{3N} f_i^j q_i^j = -\frac{1}{3V} W_j$$

Where W_j denotes the virial of microstate j.

$$\frac{1}{Q} \left(\frac{\partial Q}{\partial T} \right)_{P_{H_2}}$$

$$= \frac{1}{k_B T^2} \sum_j E_j \left(\frac{e^{-\beta E_j}}{Q} \right) + \frac{1}{k_B T} \left(\frac{\partial V}{\partial T} \right)_{P_{H_2}} \sum_j \left(-\frac{1}{3V} W_j \right) \left(\frac{e^{-\beta E_j}}{Q} \right)$$

$$= \frac{1}{k_B T^2} \sum_j E_j \left(\frac{e^{-\beta E_j}}{Q} \right) + \frac{1}{k_B T} \left(\frac{\partial V}{\partial T} \right)_{P_{H_2}} \sum_j \left(-\frac{W_j}{3V} \right) \left(\frac{e^{-\beta E_j}}{Q} \right)$$

$$= \frac{1}{k_B T^2} \langle E \rangle^{NVT} (V_{rep}, T) + \frac{1}{k_B T} \left(\frac{\partial V}{\partial T} \right)_{P_{H_2}} \left\langle -\frac{W}{3V} \right\rangle^{NVT} (V_{rep}, T)$$

$$\frac{1}{e^{-\beta P_{H_2} V_{rep}}} \left(\frac{\partial e^{-\beta P_{H_2} V_{rep}}}{\partial T} \right)_{P_{H_2}}$$

$$= \left(\frac{P_{H_2} V_{rep}}{k_B T^2} - \frac{P_{H_2}}{k_B T} \left(\frac{\partial V_{rep}}{\partial T} \right)_{P_{H_2}} \right)$$

Therefore, the enthalpy is expressed by the equilibrium internal energy $(\langle E \rangle^{NVT})$ and virial $(\langle W \rangle^{NVT})$ of NVT ensembles.

$$H(P_{H_2}, T) \cong \left[\langle E \rangle^{NVT} (V_{rep}, T) + P_{H_2} V_{rep} \right]$$

$$+ T \left(\frac{\partial V_{rep}}{\partial T} \right)_{P_{H_2}} \left[\left\langle \frac{W}{3V} \right\rangle^{NVT} (V_{rep}, T) - P_{H_2} \right] \qquad \text{Eq. 5.1-14}$$

To determine $V_{rep}(P_{H_2}, T)$, Quasi-harmonic approximation was used for the pure metals in the whole temperature ranges, including ZPE effects. $\langle E \rangle^{NVT}$ and $\langle W \rangle^{NVT}$ were replaced with the time-averaged values in MD.

5.1.3. Calculation of solution entropy S_{sol}

5.1.3.1. Entropy as a function of temperature $(T > T_0)$

The temperature dependence of entropy at an isobaric condition is expressed as

$$\left(\frac{\partial S}{\partial T} \right)_P = \frac{1}{T} \left(\frac{\partial H}{\partial T} \right)_P . \qquad \text{Eq. 5.1-15}$$

Assuming that the entropy at T_0 K is known, $S(T_0)$, the entropy at T is calculated using the temperature dependence of enthalpy as Eq. 5.1-16.

$$S(T) = \int_{T_0}^{T} \left(\frac{\partial S}{\partial T}\right)_P dT + S(T_0) = \int_{T_0}^{T} \frac{1}{T} \left(\frac{\partial H}{\partial T}\right)_P dT + S(T_0) \,. \qquad \text{Eq. 5.1-16}$$

Since the enthalpy term is obtained in Section 5.1.2, what we need to calculate is $S(T_0)$ here.

5.1.3.2. Absolute entropy at $T_0 = 100$ K: Thermodynamic integration

If ZPE is comparable to hydrogen migration barrier, the probability of hydrogen being distributed even in places far away from the T-site cannot be ignored, making it unreasonable to approximate hydrogen dynamics with quantum harmonic approximation at sufficiently low temperatures. Therefore, a two-step scheme was implemented. First, we approximate the hydrogen-trapped lattice at 100 K with classical harmonic oscillators. In this case, since there is no ZPE, the 1-d average kinetic energy of hydrogen is about 4.3 meV at 100 K according to the equipartition theorem. Considering that the migration energy of hydrogen in typical bcc metals is much larger, e.g., 95 meV in Fe and 200 meV in W, classical harmonic approximation (CL-HA) is reasonably used to estimate free energy of CLMD at 100 K, as shown in Eq. 5.1-17. ν denotes vibrational frequency at the tetrahedral sites.

$$S^{CLMD}(T_0) \cong S^{CL-QHA}(T_0) = \sum_{\nu} k_B \left[\ln\left(\frac{k_B T_0}{h\nu}\right) + 1\right] \qquad \text{Eq. 5.1-17}$$

Here, we use CL-QHA at 100 K as the state whose thermodynamic quantities are known.

Subsequently, to take into account the quantum effect without HA, the Scaled Coordinate (SC) method suggested by S. Habershon and D. Manopoulos[90], a method of thermodynamic integration from classical to quantum state, is used to calculate free energy difference between PIMD and CLMD at 100 K.

$$\frac{dF}{d\lambda} = \left\langle \frac{1}{n}\sum_{j=1}^{n}(q_j - q_c)\left(\frac{\partial V_{MTP}(u_j^\lambda)}{\partial u_j^\lambda}\right)\right\rangle_\lambda^{SC} \qquad \text{Eq. 5.1-18}$$

where scaled coordinate of the *j*-th bead at coupling parameter (λ) is u_j^λ, and it is defined as an interpolation between *j*-th bead's position (q_j) and the centroid position (q_c). *n* is the total number of imaginary time slices, or "beads". The bracket notation $\langle \cdots \rangle_\lambda^{SC}$ denotes an ensemble average of SC Hamiltonian (H_n^{SC}).

$$q_c = \frac{1}{n}\sum_{j=1}^{n}q_j \qquad \text{Eq. 5.1-19}$$

$$u_j^\lambda = \lambda q_j + [1-\lambda]q_c \qquad \text{Eq. 5.1-20}$$

$$H_n^{SC}(\boldsymbol{p},\boldsymbol{q};\lambda) = \sum_{j=1}^{n}\left[\frac{p_j^2}{2m} + \frac{1}{2}m\omega_n^2(q_j - q_{j-1})^2 + V(u_j^\lambda)\right] \qquad \text{Eq. 5.1-21}$$

Therefore, the absolute entropy of PIMD at 100 K is calculated as follows.

$$F_{sol}^{CLMD \to PIMD}(T_0)$$

$$= \int_0^1 \left(\frac{dF}{d\lambda}\right)d\lambda$$

$$\cong \left[U_{sol}^{PIMD}(T_0) - U_{sol}^{CLMD}(T_0)\right] - T_0\left[S_{sol}^{PIMD}(T_0) - S_{sol}^{CL}\qquad (T_0)\right]$$

$$\therefore S_{sol}^{PIMD}(T_0) = S_{sol}^{CL-QHA}(T_0)$$

$$+ \frac{1}{T_0}\left[-\int_0^1\left(\frac{dF}{d\lambda}\right)d\lambda + \left(U_{sol}^{PIMD}(T_0) - U_{sol}^{CLMD}(T_0)\right)\right] \qquad \text{Eq. 5.1-22}$$

5.1.4. Statistical mechanical description on hydrogen

5.1.4.1. Partition function of diatomic molecules

The diatomic molecules have translation, rotational, and vibrational motions as well as nuclear and electron spin degeneracy.

$$Q_{H_2} = Q_{trans} Q_{rot} Q_{\text{vib}} Q_{nucl} Q_{elec} \qquad \text{Eq. 5.1-23}$$

For the translational motion (Q_{trans}), it is well approximated by that of classical ideal gas because average distance between the molecules (d_{ave}) is far longer than their thermal de-Broglie wavelength (λ_{th}) at 100 K. That is, $\lambda_{th} = \frac{h}{\sqrt{2\pi m_{H_2} k_B T}} = 1.2\,\text{Å}$ and $d_{ave} = 15\,\text{Å}$ because $\frac{4\pi}{3} d_{ave}^3 = \frac{V}{N} = \frac{k_B T}{P_{H_2}}$.

$$Q_{trans} = \left(\frac{2\pi m_{H_2} k_B T}{h^2} \right)^{\frac{3}{2}} \left(\frac{N_{H_2} k_B T}{P_{H_2}} \right) \qquad \text{Eq. 5.1-24}$$

For the rotational and vibrational motions, the coupled cluster method which contains all single and double substitutions (CCSD) was used to calculate the exact energy under the vibrational (*n*) and rotational quantum number (*J)*. Different nuclear spin degeneracy was considered for fermion (H_2, T_2) and boson (D_2). Thus, rotational and vibrational motions as well as nuclear spin degeneracy are coupled in $Q_{rovib}^{fermion}$ and Q_{rovib}^{boson}.

$$
\begin{aligned}
Q_{rovib}^{fermion} = &\sum_{even\,J} \sum_{n} (2J+1)\, e^{-\beta E_{CCSD}(n,J)} \\
&+ 3 \sum_{odd\,J} \sum_{n} (2J+1)\, e^{-\beta E_{CCSD}(n,J)}
\end{aligned}
\qquad \text{Eq. 5.1-25}
$$

$$
\begin{aligned}
Q_{rovib}^{boson} = &6 \sum_{even\,J} \sum_{n} (2J+1)\, e^{-\beta E_{CCSD}(n,J)} \\
&+ 3 \sum_{odd\,J} \sum_{n} (2J+1)\, e^{-\beta E_{CCSD}(n,J)}
\end{aligned}
\qquad \text{Eq. 5.1-26}
$$

For electronic partition function (Q_{elec}), only ground state bonding orbital was considered because its large gap from the 1st excited energy. The electron spin degeneracy at ground state (g_0) is one because they are paired.

$$Q_{elec} = \sum_l g_l e^{-\beta E_{elec}(l)} \cong e^{-\beta E_{elec}(0)}$$

Eq. 5.1-27

5.1.4.2. Spin degeneracy

Table 5.1-1 Comparison between previous studies and the current study regarding assumptions about the spin states of H nuclei and their electrons.

# of spin states	Electrons of H_2	Electrons of dissolved H	Nuclei of H_2	Nuclei of dissolved H	Remarks
Fowler [91]	1	1	1	1	Nuclear rotational motions and nuclear spins are decoupled
Ogawa [92]	1	2	4	2	Self-trapped states [93]: one electron of dissolved H has two degeneracy in 1s(↑) and 1s(↓).
This study	1	1	4	2	

5.1.4.2.1. Electron spin degeneracy

(Electrons of H_2) According to the molecular orbital theory [89], two electrons are supposed to occupy the bonding orbitals (σ_{1s}), the ground state, which leads to a spin singlet state and its spin degeneracy to be 1.

(Electrons of dissolved H) Fowler simply assumed that the valence electron of dissolved H behaves like a free electron, so its spin degeneracy would be 1. To the contrary, Ogawa considered that as 2 because the dissolved hydrogen atom is in a *self-trapped state* where the electron of dissolved H has its own spin degenerate states. According to our analysis of partial density of states on H in Fe_{54} and W_{54}, Fowler's assumption is more likely to valid because hydrogen has only 33 % portion in electron. In addition, and the DOS of up-spin electrons is the same with that of down-spin electrons, and thus no spin is induced in the system. Therefore, electron spin degeneracy of dissolved H should be 1.
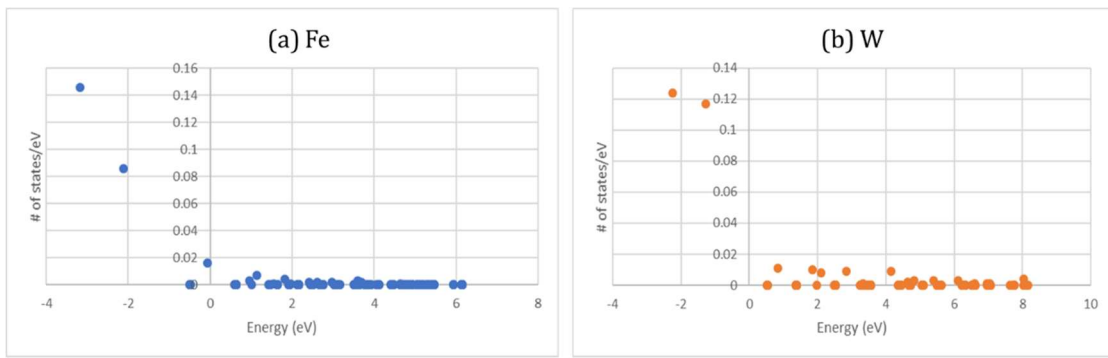
Fig. 5.1-2 Projected density of states of hydrogen in (left) Fe and (right) W below fermi energy. The fermi energy is 5.8 eV in Fe and 7.8 eV in W.

5.1.4.2.2. Nuclear spin degeneracy

bcc-W is paramagnetic, but bcc-Fe is ferromagnetic. Without external magnetic fields, nuclear spin degeneracy of hydrogen is 2 in the paramagnetic metal. The magnetic field inside bcc-Fe can vary depending on the specific conditions and properties of specimens. Nevertheless, we consider that the energy level splitting from the intrinsic magnetic field is negligibly small. The magnetic moment of the proton is $\frac{e\hbar}{m_p c} \sim \frac{10^{-8}\text{eV}}{\text{T}}$ in SI unit [94]. Then, the magnetic field should be at least 10000 T to make energy difference of 0.1 meV between the spin-up and spin-down states. Thus, nuclear spin degeneracy of hydrogen in metals is 2 in both W and Fe.

In Fowler's H solution model, nuclear rotational motions and nuclear spins are decoupled. At high temperatures, this assumption can be justified because the energy levels of rotational motion are approximately continuous. However, since our target temperature is above 100 K, we considered their coupling effects.

5.2. Solution enthalpy
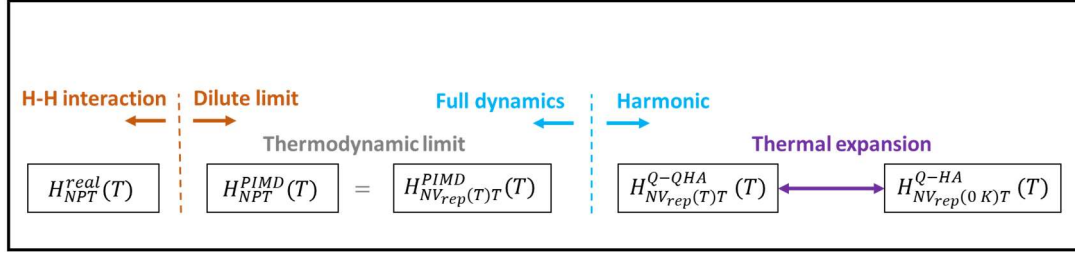
Fig. 5.2-1 A schematic diagram of methods and assumptions in calculating hydrogen solution enthalpy

Solution enthalpy of H is defined as the enthalpy difference from a gas H_2 molecule to H-dissolved state.

$$H_{sol}(T, P_0) := [H_{M+H}(T, P_0) - H_M(T, P_0)] - \frac{1}{2} H_{H_2}(T, P_0)$$

$$
\begin{aligned}
H_{M+H}(T) - H_M(T) \\
&= \left[\langle E \rangle_{M+H}^{NVT}(V_{rep}, T) - \langle E \rangle_{M}^{NVT}(V_{rep}, T) \right] \\
&+ T \left(\frac{\partial V_{rep}}{\partial T} \right) \left[\langle W \rangle_{M+H}^{NVT}(V_{rep}, T) - \langle W \rangle_{M}^{NVT}(V_{rep}, T) \right]
\end{aligned}
$$

where $V_{rep} = \langle V \rangle^{NPT}(N_M, P_0, T)$ and P_0 is consistently 1 bar in this study.

Note that the enthalpies of the hydrogen molecule were consistently calculated using the Q-HA method for the rotational and vibrational energies. H_2 and T_2 were considered ideal Fermi gases, while D_2 was assumed to be an ideal Bose gas. Fig. 5.2-2 shows the hydrogen solution enthalpies from PIMD/CLMD/quantum quasiharmonic approximation (Q-QHA) with reference to the classical quasihaarmonic approximation (CL-QHA) results. The only difference between harmonic and quasiharmonic approximation is inclusion of volumetric change in the calculations. The quasiharmonic approximation includes thermal expansion effects, so it's more accurate than harmonic approximation. Because the three methods were used to calculate the pure and hydrogen-dissolved metals, enthalpies of H_2, D_2,

and T_2 were cancelled out.
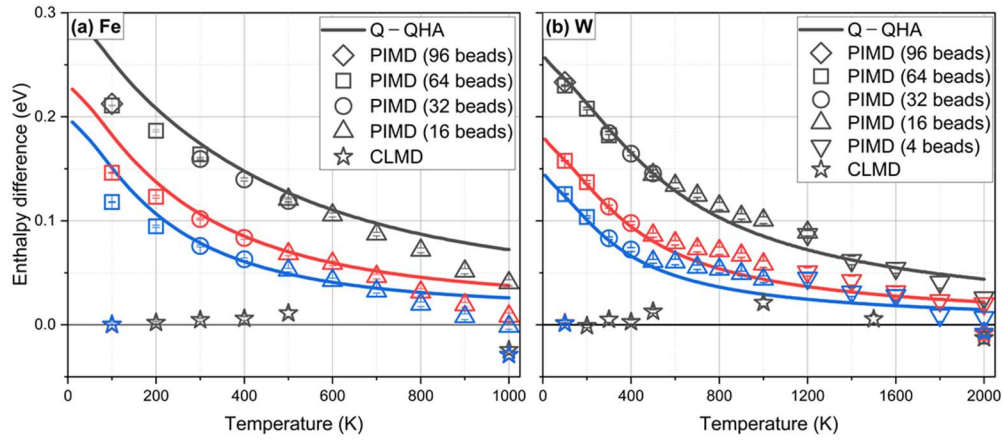
Fig. 5.2-2 Hydrogen solution enthalpy in (a) Fe and (b) W. Black, red, and blue colors denote H_2, D_2, and T_2, respectively. The enthalpies of PIMD/CLMD/Q-QHA were subtracted by the CL-QHA values.

According to the Trotter-Suzuki approximation[95,96], a sufficiently large number of beads should be used to accurately reflect the NQEs at low temperatures in PIMD. On the other hand, at high temperatures, the influence of NQEs is small, so smaller numbers of beads are sufficient to maintain the same accuracy. In Fig. 5.2-2, The bead convergence was checked for H_2 solution enthalpy by varying the number of beads from 4 to 96 above 100 K. This bead convergence test should be performed in the whole temperature ranges to minimize computation cost while maintaining accuracy: 64 beads for 100K ~ 200 K, 32 beads for 300 K ~ 400 K, 16 beads for 500 K ~ 1100 K, 4 beads for 1200 K ~ 2000 K. Conservatively, the estimated optimal numbers for H were applied for D and T at the same temperatures since the NQEs are less significant for heavier isotopes. In Fig 5.2-2, the following three points are worthy to discuss: NQEs, dynamic effects, and isotope effects.

In Section 4, we confirmed that the classical-quantum crossover temperatures of H diffusion in Fe and W are 500 K. However, in the case of H solubility,

the enthalpies of Q-QHA and PIMD exhibited substantial deviations from their classical outcomes, at temperatures exceeding 800 K in both metals. For example, the difference in H solution enthalpy between PIMD and CLMD in Fe was 65 ± 4 meV at 1000 K whose Boltzmann factor is around 0.5. If CLMD was used to predict the 1000 K solution enthalpy, solubility would be overestimated by about twice as much. The reason why the NQEs of solution appear more pronounced than those of diffusion at temperatures above 500 K is owing to the difference in compactness between the most stable site (T-site) and its counterpart. In the case of the solution, the counterpart state of hydrogen in T-site is a gas in vacuum, so atomic density near hydrogen significantly changes during the dissolution. On the other hand, the diffusion process occurs when hydrogen migrates from a T-site to saddle sites. The change in atomic compactness during the migration must be very small, compared to that during the solution process. Therefore, the NQEs of solution are significant even above the crossover temperature of diffusion, and classical approaches may fail to predict accurate hydrogen solubility.

The dynamic effects can be estimated from the difference between the results of MD and QHA in the same approach. Generally speaking, the energy of hydrogen decreases at low temperatures, leading to a reduction in thermal displacement. This causes hydrogen to be strongly bound to the most stable site (T-site), making the dynamic effects negligible. If so, harmonic approximation can effectively replace MD. In a classical approach, the enthalpies of CLMD must converge to those of CL-QHA since kinetic energy becomes zero at 0 K limit. However, in a quantum approach, the kinetic energy of hydrogen does not decrease in proportion to temperature. As a result, anharmonicity does not completely vanish at the limit of 0 K. As shown in Fig. 5.2-2, CLMD enthalpies converged to CL-QHA enthalpies below 200 K in the metals. While the dynamic effects of PIMD are negligible below 500 K in W, the PIMD enthalpies for Fe substantially deviated from the Q-QHA enthalpies below 200 K, which imply that the low-temperature dynamic effects including NQEs are significant only in Fe.

75

Isotope effects were not observed in classical methods, which is consistent with classical statistical mechanics. On the other hand, the quantum isotope effects were observed in Fe where the difference in the solution enthalpies between PIMD and Q-QHA decreased below 200 K as hydrogen mass increased. However, such quantum isotope effects were not observed in W.

5.3. Solution entropy
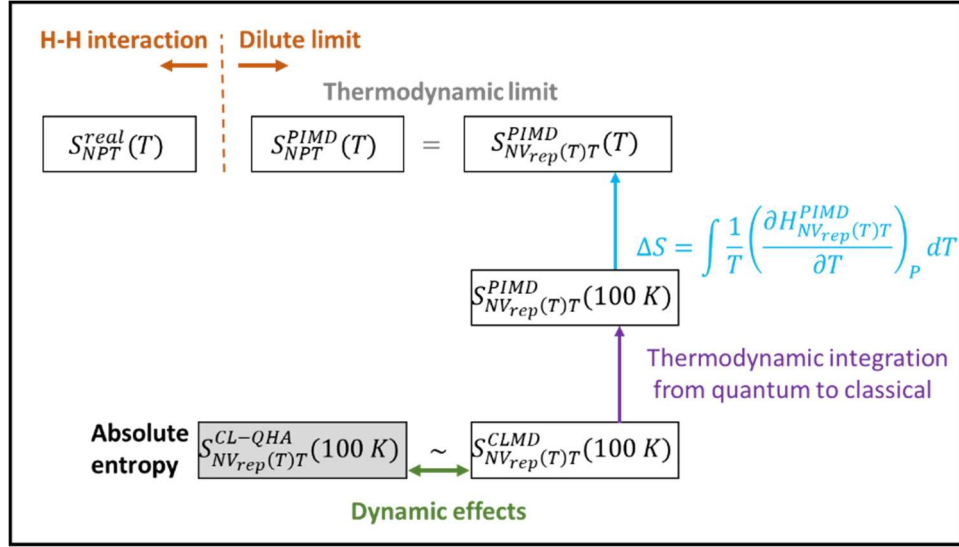
Fig. 5.3-1 A schematic diagram of methods and assumptions in calculating hydrogen solution entropy

5.3.1. Solution entropy at T_0

Thermodynamic integration from CLMD to PIMD was conducted for calculating $\Delta F_{sol}^{CLMD \rightarrow PIMD}$ which is used to estimate PIMD solution entropy (S_{sol}^{PIMD}) at 100 K by the following equations

$$\Delta S_{sol}^{CLMD \rightarrow PIMD} = (\Delta U_{sol}^{CLMD \rightarrow PIMD} - \Delta F_{sol}^{CLMD \rightarrow PIMD})$$

$$S_{sol}^{PIMD} = S_{sol}^{CLMD} + \Delta S_{sol}^{CLMD \rightarrow PIMD}$$

Fig. 5.3-2. shows the $dF/d\lambda$ values of MD and HA by the SC method[90] for the thermodynamic integration. Habershon and Manopoulos[90] analytically derived mathematical forms of the SC method with quantum harmonic approximation.

$$\frac{dF_{SC}^{HA}}{d\lambda} = \sum_i \frac{y_i \lambda \, coth(y_i \lambda) - 1}{\beta \lambda} \qquad \text{Eq. 5.3-1}$$

where $y_i = \beta h \nu_i / 2$. In this study, all vibrational modes of both hydrogen and metals

77

are considered in the QHA.
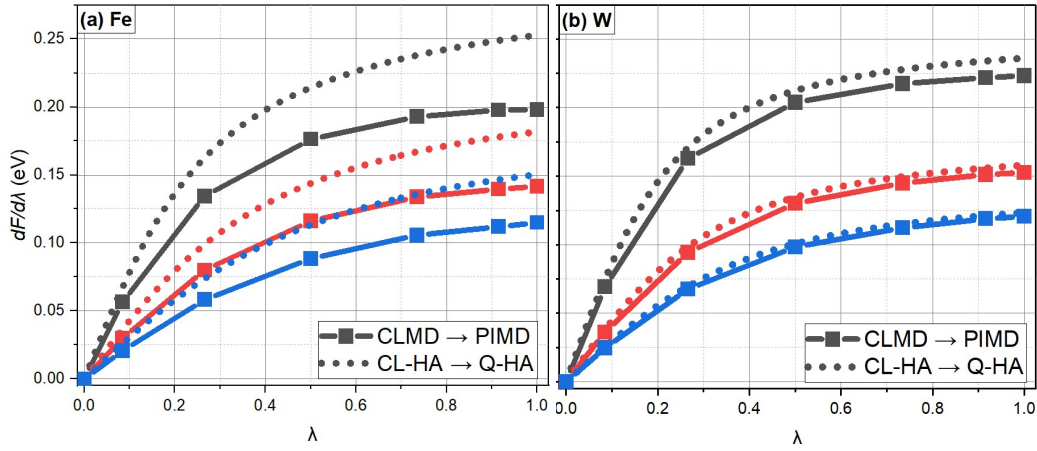
Fig. 5.3-2 Thermodynamic integration of MD and HA from classical $(\lambda = 0)$ to quantum $(\lambda = 1)$ approach at 100 K in (a) Fe and (b) W. Black, red, and blue colors denote H, D, and T, respectively. 7-points Gauss-Lobatto quadrature was applied for the numerical integrations from CLMD to PIMD.

While analytical form of $dF/d\lambda$ was derived in HA, massive computations with 64 beads/atom are required to increase the number of data points in "CLMD→PIMD". Because small number of data points can lead to large error in the numerical integration, there is a need to discuss the most suitable numerical integration method for application of the SC method to our purpose.

Rather than using equal distance for numerical integration of PIMD results, it is considered more efficient to use Gaussian quadrature with few points. In particular, for the SC method, the values of the two endpoints $(\lambda = 0, 1)$ can be calculated without additional computations by understanding the physical meaning in the formulas. $dF/d\lambda$ at the right endpoint $(\lambda = 1)$ can be obtained from twice of the difference in kinetic energy between CLMD and PIMD, while the value of the left endpoint $(\lambda = 0)$ is zero by definition[90]. If the Gauss-Lobatto rule, which includes both endpoints in the quadrature, is used, it is considered the most efficient integrator for performing the SC thermodynamic integration. In this study, the 7-point

Gauss-Lobatto rule was used because it resulted in at most 0.02 meV error in the numerical integration from CL-HA to quantum harmonic approximation (Q-HA) where analytical solution of HA is known. Table 5.3-1. shows the change of thermodynamic variables from classical to quantum approaches at 100 K.

It is worth discussing how the agreement between MD and HA varies depending on the metals. While there is a large difference of 35 meV in $\Delta F_{sol}^{CLMD \rightarrow PIMD}$ between HA and PIMD for H in Fe, the difference is only at 8.8 meV for H in W. This discrepancy indicates that the HA method agrees well with PIMD only for W due to the weak dynamic effects, while it failed to reproduce similar results of PIMD for Fe. A scientific discussion of these phenomenological differences will be provided in more detail in Section 5.5.2. In terms of isotope effects, the gap between HA and PIMD decreases as the mass of the isotope increases for Fe and W, which can be understood that the NQEs become smaller for the heavier isotopes.

Table 5.3-1 Change of thermodynamic variables from classical to quantum approaches at 100 K.

Unit: meV	H in Fe		H in W	
Method	CLMD → PIMD	CL-HA → Q-HA	CLMD → PIMD	CL-HA → Q-HA
$\Delta F_{sol}^{CLMD \rightarrow PIMD}$	153.6	188.6	177.4	186.2
$\Delta U_{sol}^{CLMD \rightarrow PIMD}$	211.0 ± 0.5	252.8	228.4 ± 0.7	236.1
$\Delta S_{sol}^{CLMD \rightarrow PIMD}$	57.4	64.2	51.0	49.9

Unit: meV	D in Fe		D in W	
Method	CLMD → PIMD	CL-HA → Q-HA	CLMD → PIMD	CL-HA → Q-HA
$\Delta F_{sol}^{CLMD \rightarrow PIMD}$	101.3	116.7	113.0	118.2
$\Delta U_{sol}^{CLMD \rightarrow PIMD}$	146.1 ± 0.5	166.8	155.9 ± 0.5	160.2
$\Delta S_{sol}^{CLMD \rightarrow PIMD}$	44.8	50.1	42.9	42.0

Unit: meV	T in Fe		D in W	
Method	CLMD → PIMD	CL-HA → Q-HA	CLMD → PIMD	CL-HA → Q-HA
$\Delta F_{sol}^{CLMD \rightarrow PIMD}$	78.1	86.9	85.5	89.3
$\Delta U_{sol}^{CLMD \rightarrow PIMD}$	117.7 ± 0.5	129.2	124.4 ± 0.7	126.4
$\Delta S_{sol}^{CLMD \rightarrow PIMD}$	39.6	42.3	38.9	37.1

5.3.2. Entropy change above 100 K

As can be seen from the fact that the CLMD solution enthalpy converges to that of CL-QHA in the 0 K limit in Fig. 5.2-2, it is evident that the entropy CLMD can

be replaced with that of CL-QHA at sufficiently low temperatures due to its small thermal displacement.

$$S_{sol}^{CLMD}(100\ K) \cong S_{sol}^{CL-QHA}(100\ \text{K}) \qquad \text{Eq. 5.3-2}$$

By correcting the entropy difference between CLMD and PIMD obtained in Table 5.3-1, the 100 K solution entropy of PIMD can be calculated.

$$S_{sol}^{PIMD}(100\ \text{K}) \cong S_{sol}^{CL-QHA}(100\ \text{K}) + \Delta S_{sol}^{CLMD \to PIMD}(100\ \text{K}) \qquad \text{Eq. 5.3-3}$$

Using the relationship $dS_{sol}^{PIMD} = \frac{1}{T}\left(\frac{\partial H_{sol}^{PIMD}}{\partial T}\right)$ of the isobaric-isothermal ensembles, the PIMD solution entropy above 100 K in the form of an integrated solution enthalpy is represented as Eq. x.

$$
\begin{aligned}
S_{sol}^{PIMD}(T) &= \int_{100\ K}^{T} \frac{1}{T}\left(\frac{\partial H_{sol}^{PIMD}}{\partial T}\right)_P dT + S_{sol}^{PIMD}(100\ K) \\
&\cong \int_{100\ K}^{T} \frac{1}{T}\left(\frac{\partial H_{sol}^{PIMD}}{\partial T}\right)_P dT + S_{sol}^{CL-QHA}(100\ \text{K}) \qquad \text{Eq. 5.3-4} \\
&\quad + \Delta S_{sol}^{CLMD \to PIMD}(100\ \text{K})
\end{aligned}
$$

For the integration, the cubic spline method was used to approximate the continuous values of $H_{sol}^{PIMD}(T)$ because its exact function form is unknown. The solution entropy of CL-QHA, Q-QHA, and PIMD are plotted in Fig 5.3-2.
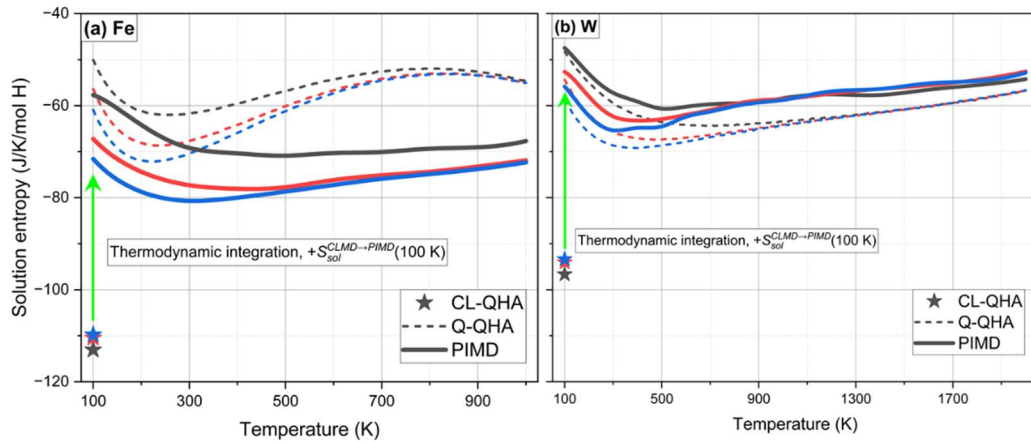
Fig. 5.3-3 Hydrogen solution entropy calculated by CL-QHA, Q-QHA, and PIMD in (a) Fe and (b) W. Black, red, and blue colors denote H_2, D_2, and T_2, respectively. Note that the plots denote only non-configurational entropies.

As shown in Fig. 5.3-3, the 100 K PIMD solution entropy was estimated by the following procedure. At first, S_{sol}^{CL-QH} (100 K) values were calculated for all vibrational modes. Secondly, PIMD solution entropies at 100 K were calculated by adding $\Delta S_{sol}^{CLMD \rightarrow PIMD}$ (100 K) to the corresponding S_{sol}^{CL-QHA} (100 K). Finally, the entropy changes from 100 K were calculated by the thermodynamic relation $dS_{sol}^{PIMD} = \frac{1}{T}\left(\frac{\partial H_{sol}^{PIMD}}{\partial T}\right)$. In Fig 5.3-2, the following two points are worthy to discuss: dynamic effects and isotope effects.

Similar to the phenomena observed in Fig. 5.2-2 and Fig. 5.3-2, the PIMD solution entropies for Fe substantially deviated from those of Q-QHA, while the PIMD solution entropies for W showed good agreement with Q-QHA. To be specific, in the case of W, both methods exhibited a similar trend above approximately 800 K. However, in the case of Fe, the values and slopes varied between PIMD and Q-QHA.

In the case of isotope effects, PIMD produced consistent results above 500 K for all cases in the metals, except for H_2 in Fe. It exhibits not only different values but also distinct slopes compared to the trends of D_2 and T_2. This indicates that the NQEs

82

of H_2 alone remain significant even at a temperature as high as 1000 K.

5.4. Solubility and Permeability

5.4.1. Binding energy correction

The MTPs were only trained in hydrogen-dissolved bulk systems, so they do not represent the accurate hydrogen binding energy with DFT accuracy. Thus, a correction term should be added to make the 0 K binding energies of the MTPs equivalent to those of the DFT calculations. The correction only deals with classical potential energy, not ZPE although its volume is fixed to the 0 K volume (V_{ZPE-0}) of the pure metals including ZPE effects determined by Q-QHA.

$$
BE_{ZPE-0K}^{corr} := \left[PE_{M+H}^{DFT}(V_{ZPE-0K}) - PE_{M}^{DFT}(V_{ZPE-0K}) - \frac{1}{2} PE_{H_2}^{DFT} \right] \\
- \left[PE_{M+H}^{MTP}(V_{ZPE-0}\ ) - PE_{M}^{MTP}(V_{ZPE-0K}) - \frac{1}{2} PE_{H_2}^{MTP} \right]
$$

Eq. 5.4-1

Then, the accurate form of the solution enthalpy is written as follows.

$$
\begin{aligned}
H_{sol}(T, P_0) \\
= BE_{ZPE-0}^{corr}\ + \left[\langle U \rangle_{M+H}^{NVT}\big(V_{rep}(T, P_0), T\big) - \langle U \rangle_{M}^{NVT}\big(V_{rep}(T, P_0), T\big) \right] \\
+ T_0 \left(\frac{\partial V_{rep}(T, P_0)}{\partial T} \right)_P \left[\left\langle \frac{W}{3V} \right\rangle_{M+H}^{NVT} \big(V_{rep}(T, P_0), T\big) \right. \\
\left. - \langle P \rangle_{M}^{NVT}\big(V_{rep}(T, P_0), T\big) \right] - \frac{1}{2} H_{H_2}(T, P_0)
\end{aligned}
$$

Eq. 5.4-2

Regarding the 0 K binding energy correction term (BE_{ZPE-0K}^{corr}), DFT should not be necessarily very accurate for it because the DFT systematic errors may not be sufficiently cancelled out when calculating the total energy difference between a hydrogen molecule in vacuum and hydrogen solute in lattice[97]. We estimate that the DFT error would be low for the migration energy in diffusion since the two systems being compared have the same lattice structure. On the contrary, in the case of solutions, the two systems being compared are of different types, namely a metal and a diatomic molecule. Therefore, the systematic error inherent in each system would not be fully canceled out but rather included in the 0 K DFT binding energy. The estimated error in the DFT binding energy will be discussed in Section 5.5.1.1. by

comparing activation energies of permeability between PIMD and experiments.

Table 5.4-1 0 K Binding energy of H in T-sites predicted by DFT calculations. ZPE corrections are not included here.

Unit: eV	Fe	W	Supercell size	K-space grid	Energy cutoff (eV)	Volume
This study	0.183	0.909	$4 \times 4 \times 4$	$5 \times 5 \times 5$	650	0 K volume including ZPE effects.
Jiang and Carter[9]	0.20		$4 \times 4 \times 4$	$2 \times 2 \times 2$	350	Geometry optimized volume
Lee et al.[98]		0.94	$2 \times 2 \times 2$	$8 \times 8 \times 8$	450	
Kong et al.[99]		0.89	$3 \times 3 \times 3$	$5 \times 5 \times 5$	500	

5.4.2. Solubility and permeability
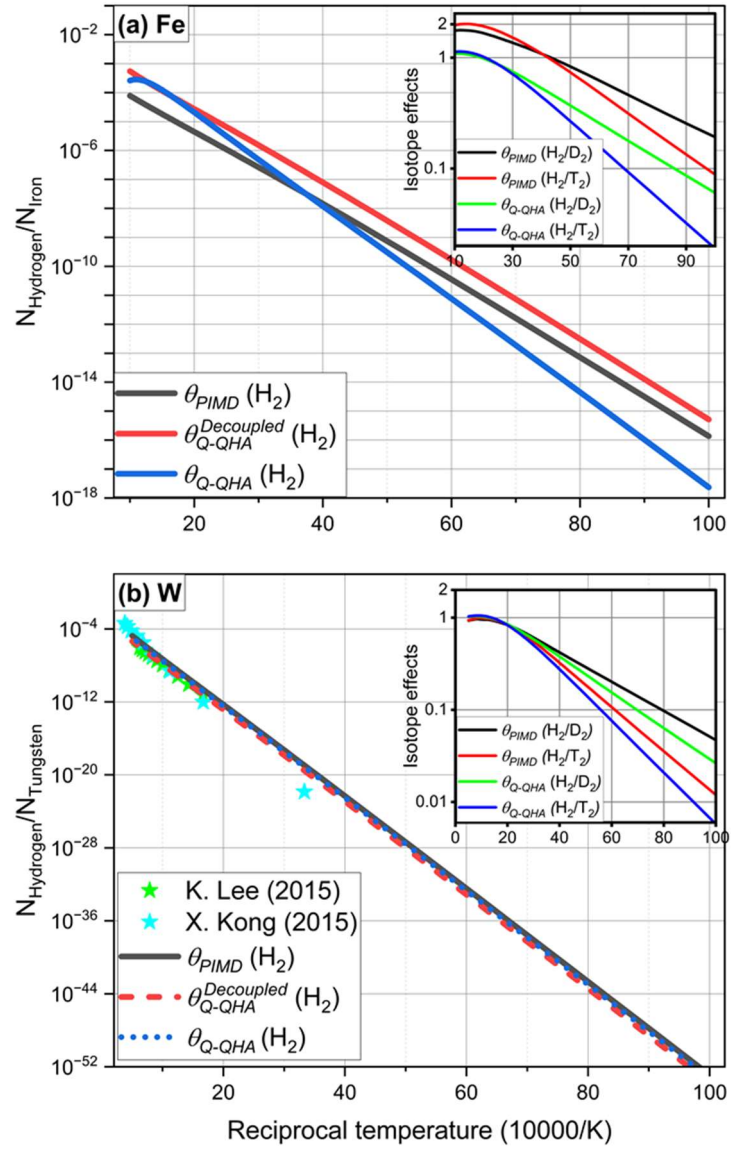
Fig. 5.4-1 H_2 solubility and its isotope effects with D_2 and T_2 in (a) Fe and (b) W. $\theta_{QHA}^{Decoupled}$ denotes hydrogen solubility calculated with Q-QHA excluding every vibrational motion of the metals.

In Section 3.1. and 3.2., we proposed systematic ways to use PIMD and the

MTPs for accurate consideration of NQEs and dynamic effects when estimating solution enthalpy and entropy above 100 K. Fig. 5.4-1. shows the predicted solubility of H_2 and the its isotope effects with D_2 and T_2 in the metals. In the case of Fe, there was a significant difference of approximately 60-fold between Q-QHA solubility and PIMD solubility at 100 K. On the other hand, in the case of W, the difference was only around two-fold at the same temperature, which indicate that using Q-QHA in predicting hydrogen solubility in W can be well justified while it cannot be in Fe.

According to classical statistical mechanics, solubility does not depend on hydrogen mass, so the H_2 solubility should be equal to the D_2 and T_2 solubility. However, according to quantum mechanics, isotope effects arise due to the difference in ZPE between hydrogen molecule and the hydrogen-dissolved states, which depends on the mass. This can be observed in the insets of Fig. 5.4-1. The prominently high solubility specifically for H in Fe is attributed to the significantly higher solution entropy compared to other isotopes, as shown in Fig. 5.3-3.

One notable point is that, regarding the solubility of H_2, in the case of Fe, the Arrhenius plots of Q-QHA showed significant non-linearity above 800 K unlike that of W. This phenomenological difference can be explained by the coupling between hydrogen vibrations and lattice phonons. In the case of W, the vibrational motions of the dissolved hydrogen are almost decoupled from the lattice phonons, whereas in Fe, they are strongly coupled. This can be understood by observing how the phonon frequency changes depending on the presence of hydrogen. In W, the phonon frequency changes by a maximum of 0.05 THz (0.7 %) after hydrogen dissolution at the 0 K volume. In contrast, in Fe, it changes significantly by at most 0.5 THz (4 %). As the temperature arises, the change equilibrium volume affects the vibrational frequencies. The phonon vibrations of W show only small difference from the dissolved hydrogen, so the thermal expansion effects on lattice phonons are cancelled out in the solution enthalpy and entropy. On the contrary, in Fe, the vibrating motions are strongly dependent on the presence or absence of hydrogen under the thermal expansion. Therefore, the metallic vibrations of Fe caused by the thermal expansion

87

has a meaningful influence on the entropy and enthalpy, which resulted in non-linear Arrhenius plots in Fig. 5.4-1 (a).

According to this analysis, for metals with weak hydrogen-metal coupling, the use of HA without volume change can be justified. Lee et al. used HA to estimate solubility with the 0 K solution energy and vibrational frequencies of only hydrogen, but produced very similar results with ours. Kong et al. considered the thermal expansion effects in their solubility calculations. However, their solubility exhibits a noticeably different slope compared to ours, which cannot be solely attributed to the difference in the binding energy presented in Table 5.3-1. This discrepancy can be caused by the fact that they used experimental data to determine the solution entropy and neglected the temperature dependence of entropy in their calculations.

If hydrogen is strongly coupled to metals, like Fe, the differences in metallic motions due to thermal expansion effects can have a significant impact on solubility, indicating the importance of QHA for the systems. While there are numerous reported experimental values that could be compared with our computational results, we decided not to directly compare them for the following reasons.

Firstly, some direct measurement techniques are not available because the hydrogen concentrations in Fe and W are too low. The direct solubility measurement techniques, such as Differential scanning calorimetry (DSC), thermal desorption spectroscopy (TDS), have limitations in materials with dilute hydrogen concentration because the magnitude of gas signals are too weak to detect. Secondly, solubility in hydrogen permeation experiments is derived indirectly by dividing permeability by diffusivity. While reported diffusivity values may exhibit significant deviations, permeation data tends to have relatively smaller deviations. Hence, solubility data is also expected to have significant deviations [100]. Finally, similar to diffusivity, solubility is significantly influenced by the microstructure and can be challenging to compare with our current computational results, which assume a defectless lattice. The impact of microstructural effects makes direct comparisons difficult. Therefore, it would be reasonable to compare our calculated permeability with corresponding

experimental values which is free from large deviation. This allows for a meaningful comparison with reported experimental values, as the diffusivity and solubility were calculated by the same moment tensor potential.
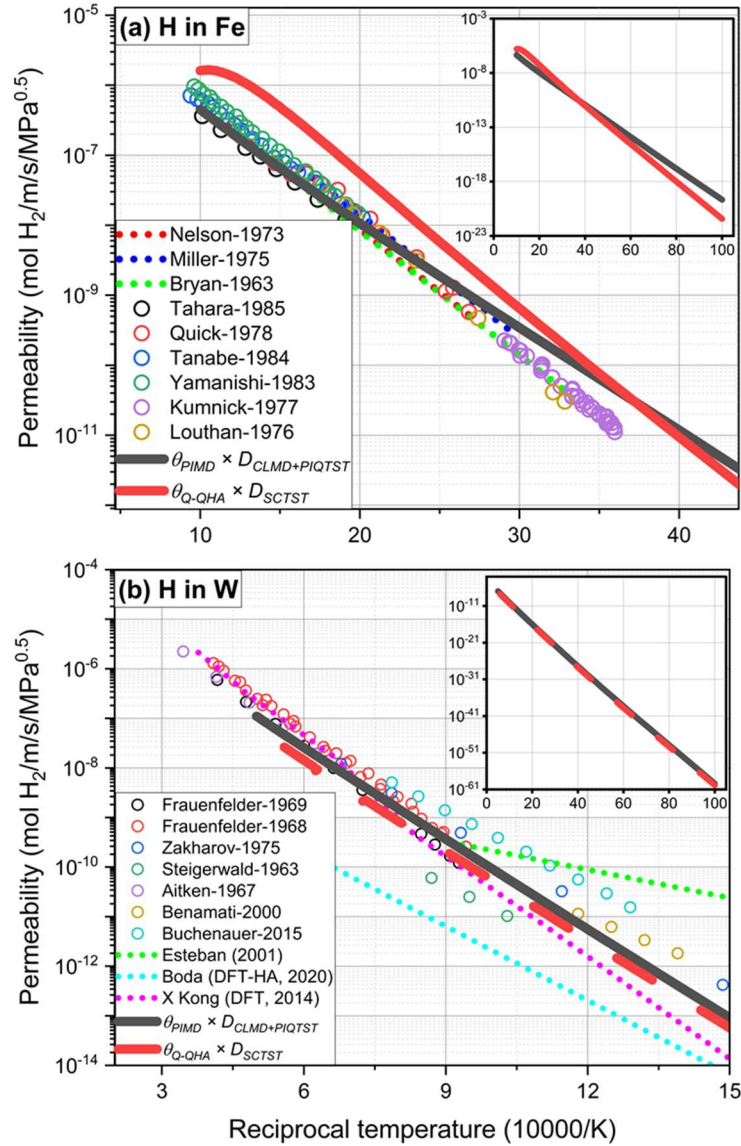
Fig. 5.4-2 H_2 permeability in (a) Fe and (b) W. "CLMD+PIQTST" denotes the parameterized functions which were fitted to the diffusion coefficients of CLMD above 500 K and PIQTST below 300 K[101]. Semi-classical transition state theory (SCTST) is harmonic approximation to calculate diffusivity including ZPE and

tunneling effects. $\boldsymbol{D_{SCTST}}$ values were calculated with Eq. (12) in Di Stefano's study including metallic vibrational modes.

To convert the solubility into permeability for comparison with experimental values, we selected corresponding methods that are consistent with Q-QHA and PIMD. D_{SCTST} is consistent with θ_{Q-QH} as it takes into account ZPE and tunneling effects under the harmonic approximation, while using migration barrier and vibrational frequencies at the thermal equilibrium volume. $D_{CLMD+PIQTST}$ represents the parameterized functions obtained by fitting CLMD diffusivity at temperatures above 500 K and PIQTST diffusivity at temperatures below 300 K. It closely reflects dynamic effects above 500 K as it provides values similar to CLMD, but it has the limitation of incorporating harmonic approximation in PIQTST at low temperatures. However, PIQTST is a relatively accurate method with an accuracy that shows a difference of only about twice the value of RPMD/CMD at 100 K. Since most experimental values are measured at temperatures above 300 K, multiplying them by θ_{PIMD} is a reasonable approach to compare with the experimental values.

The converted PIMD permeability $\left(= \theta_{PIMD} \times D_{CLMD+PIQTS}\right)$ shows good agreement with the available experimental values at high temperatures as seen in Fig. 5.4-2 (a) and (b). On the other hand, the converted Q-QHA permeability $(= \theta_{PIMD} \times D_{SCTST})$ showed a similar trend to the experimental values only for H in W, while it exhibited significant differences for H in Fe. As mentioned earlier, this highlights the fact that the harmonic approximation cannot produce accurate solubility for H in Fe.

5.5. Discussion

5.5.1. Error analysis in solubility

5.5.1.1. Systematic error: binding energy and finite system size effects
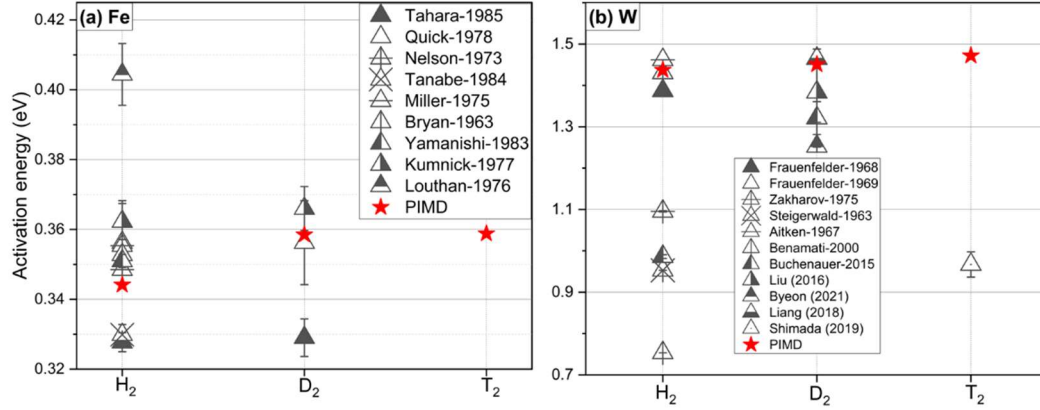
Fig. 5.5-1 Activation energy of hydrogen permeability in (a) Fe and (b) W.

In Fe, an error of about 0.01 eV scale was observed, while in W, it is on the scale of 0.1 eV. However, since the experimental values have GB effects, it is difficult to fully trust them.
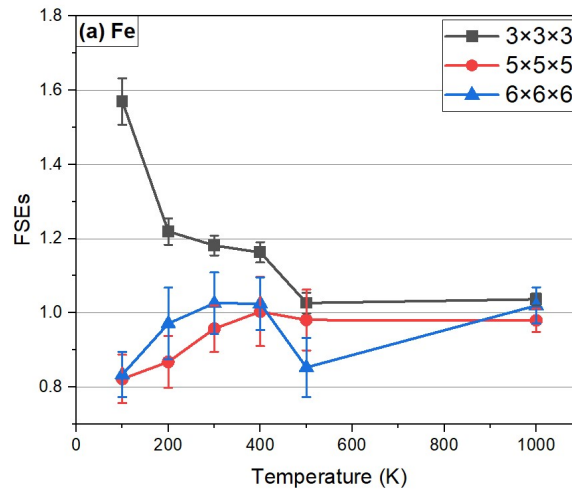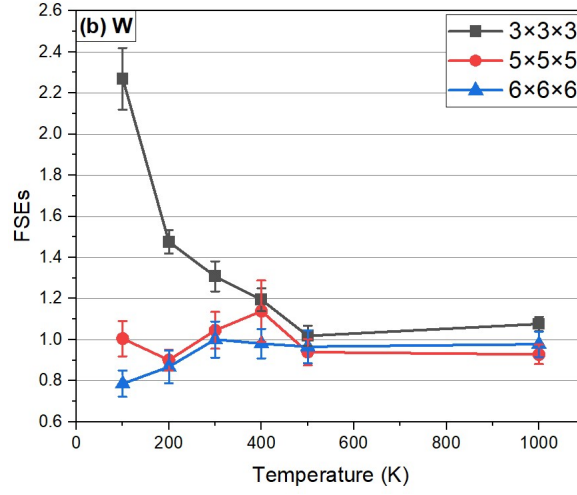
Fig. 5.5-2 FSEs in solubility determined by CLMD-NVT. y-axis denotes

$$exp\left[\frac{\left(H_{sol}(T)-H_{sol}^{4\times4\times4}(T)\right)}{k_BT}\right].$$

According to the analysis of FSEs by CLMD in Fig. 5.5-2, there can be a systematic error of approximately 10 % ~ 20 % in the low-temperature solubility induced by FSEs for a 4×4×4 supercell size.

5.5.1.2. Random error: Numerical precision of solution enthalpy & solution entropy

$$\theta(T) = 6\,exp\left[\frac{S_{sol}^{PIMD}(T_0)}{k_B} + \frac{1}{k_B}\int_{T_0}^{T}dS_{sol}^{PIMD} - \frac{H_{sol}^{PIMD}(T)}{k_BT}\right]$$

The first term is determined by $\Delta F_{sol}^{CLMD\rightarrow PIMD}(T_0)$ and $\Delta U_{sol}^{CLMD\rightarrow PIMD}(T_0)$, but we suggest that the former has higher uncertainty than that of latter. This is because uncertainty of $\frac{dF_{SC}^{PIMD}}{d\lambda}$ vanishes at $\lambda \rightarrow 0$ limit, so the random error of $\Delta F_{sol}^{CLMD\rightarrow PIMD}(T_0)$ should be smaller than that of $\Delta U_{sol}^{CLMD\rightarrow PIMD}(T_0)$.

$$\sigma^2\left(\frac{S_{sol}^{PIMD}(T_0)}{k_B}\right) \cong \sigma^2\left(\frac{H_{sol}^{PIMD}(T_0)}{k_B T_0}\right)$$

The second term is calculated by the numerical integration with equal intervals ($\Delta T = 100\ \text{K}$ in this study).

$$\frac{1}{k_B}\int_{T_0}^{T} dS_{sol}^{PIMD} = \frac{1}{k_B}\int_{T_0}^{T}\frac{1}{T}\left(\frac{\partial H_{sol}^{PIMD}}{\partial T}\right)dT$$

$$= \frac{1}{k_B}\left[\left(\int_{T_0}^{T_0+\Delta T}\frac{1}{T}\left(\frac{\partial H_{sol}^{PIMD}}{\partial T}\right)dT\right) + \left(\int_{T_{0+\Delta T}}^{T_0+2\Delta T}\frac{1}{T}\left(\frac{\partial H_{sol}^{PIMD}}{\partial T}\right)dT\right) + \cdots\right.$$

$$\left. + \left(\int_{T-\Delta T}^{T}\frac{1}{T}\left(\frac{\partial H_{sol}^{PIMD}}{\partial T}\right)dT\right)\right]$$

$$\cong \frac{1}{k_B}\left[\left(\frac{H_{sol}^{PIMD}(T_0+\Delta T) - H_{sol}^{PIMD}(T_0)}{\Delta T}\right)\left(\int_{T_0}^{T_0+\Delta T}\frac{1}{T}dT\right) + \cdots\right.$$

$$\left. + \left(\frac{H_{sol}^{PIMD}(T) - H_{sol}^{PIMD}(T-T_0)}{\Delta T}\right)\left(\int_{T-\Delta T}^{T}\frac{1}{T}dT\right)\right]$$

$$\cong \frac{1}{k_B}\left[\left(\frac{H_{sol}^{PIMD}(T_0+\Delta T) - H_{sol}^{PIMD}(T_0)}{\Delta T}\right)\ln\left(\frac{T_0+\Delta T}{T_0}\right) + \cdots\right.$$

$$\left. + \left(\frac{H_{sol}^{PIMD}(T) - H_{sol}^{PIMD}(T-T_0)}{\Delta T}\right)\ln\left(\frac{T}{T-\Delta T}\right)\right]$$

$$\cong \frac{1}{k_B \Delta T}\left[-H_{sol}^{PIMD}(T_0)\ln\left(\frac{T_0+\Delta T}{T_0}\right)\right.$$

$$+ \sum_{\tau=T_0+\Delta T,\ T_0+2\Delta T,\ \cdots,\ T-\Delta T} H_{sol}^{PIMD}(\tau)\ln\left(\frac{(\tau+\Delta T)(\tau-\Delta T)}{\tau^2}\right)$$

$$\left. + H_{sol}^{PIMD}(T)\ln\left(\frac{T}{T-\Delta T}\right)\right]$$

The variation of the third term is as follows.

$$\sigma^2\left(-\frac{H_{sol}^{PIMD}(T)}{k_B T}\right)$$

The major error term of the first term $\left(\frac{H_{sol}^{PIMD}(T_0)}{k_B T_0}\right)$ is negatively correlated

with the first term of the second term $\left(-\frac{H_{sol}^{PIMD}(T_0)}{k_B \Delta T}\ln\left(\frac{T_0+\Delta T}{T_0}\right)\right)$. Likewise, the third

term $\left(-\frac{H_{sol}^{PIMD}(T)}{k_B T}\right)$ is also negatively correlated with the last term of the second term

$\left(\frac{H_{sol}^{PIMD}(T)}{k_B T}\ln\left(\frac{T}{T-\Delta T}\right)\right)$. Based on the negative correlation between the error terms in

each term, it can be inferred that even if the individual error terms are large, the

overall error in the final value, solubility, becomes smaller due to error cancellation.
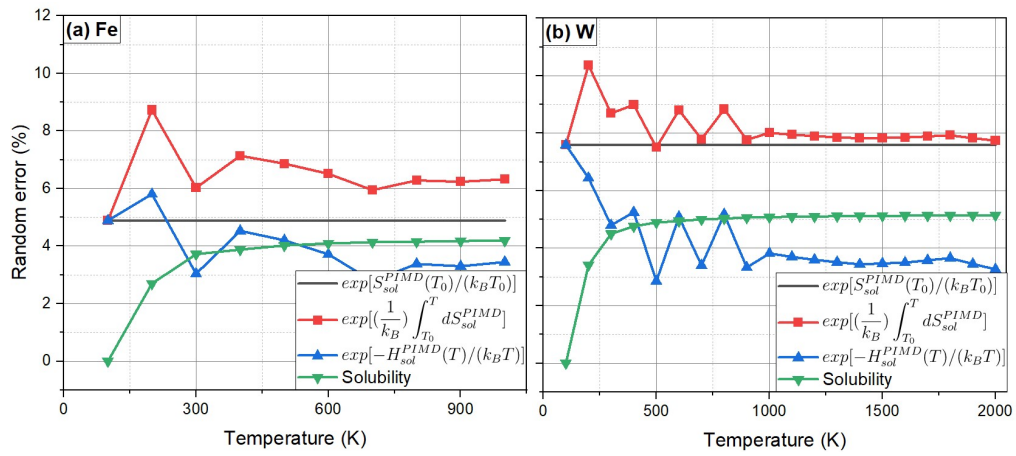
Fig. 5.5-3 Random error in each term of solubility.

At 100 K, since the errors are completely canceled out, there is no

uncertainty due to PIMD precision, only systematic errors exist. However, above 100

K, the uncertainty in PIMD enthalpy accumulates gradually. Starting from 500 K and

above, there is approximately a 4-5% uncertainty in the solubility of Fe and W owing

to this accumulated uncertainty in the PIMD enthalpy.

5.5.2. Validation of harmonic approximation
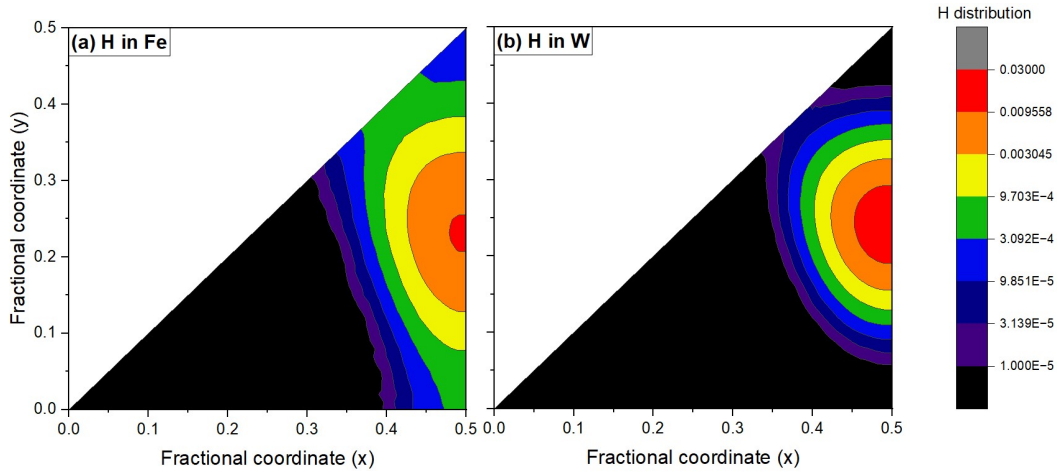
Fig. 5.5-4 H distribution on 001 plane calculated by PIMD-NVT at 100 K. $6 \times 6 \times 6$ supercell was adopted to reasonably fix center of mass.

Anharmonicity is determined by relative difference between the ZPE and classical migration barrier. Table 5.5-1 shows the migration quantities through the trigonal sites in Fe and W. Because the ZPE calculation is based on harmonic approximation, there may be systematic errors in ZPE.

Table 5.5-1 Classical migration barrier and ZPE with respect to the dominant migration path (T-Tri-T).

Unit: meV	H in Fe	H in W
Classical migration barrier	97	208
ZPE	51	42

6. Conclusion

In this thesis, I developed and validated accurate and easy-to-use computational methods for predicting hydrogen diffusivity and solubility in bcc metals. While the use of QHA is not justified in some due to the large dynamic effects, our method can be applied to any bcc metal regardless of its element.

In Section 3, MLPs were trained to reproduce the DFT force field near the configuration space related to hydrogen dynamics in bcc metals using MS calculation results and active learning. The migration barriers and normal mode frequencies were reproduced with reasonable accuracy compared to those of DFT. The fast speed of the MLPs also allowed long-time quantum dynamics simulations using large numbers of atoms and beads, which is currently difficult with AI-PIMD. Consequently, the simulation results in this study attained high accuracy at the DFT level and high numerical precision.

In Section 4, the H diffusion coefficients obtained from CLMD/CMD/RPMD were compared to analyze the NQEs. Their diffusion coefficients were almost indistinguishable above 500 K considering the statistical errors. This implies that NQEs should be considered for H dynamics below 500 K for all metals tested in this study. Although there is an abundance of experimental data, most data show inconsistent trends, mainly due to surface and trapping effects. Reviewing and interpreting previous studies, we identified experimental data that were considered reliable. The calculated results were in good agreement with the experimental data.

In Section 5, hydrogen solubility was predicted from PIMD, and compared to experimental values after conversion to permeability. The NV(P)T approximation removed the significant system size effects and calculation time that is required for the NPT simulations. For the high migration barrier case (W), our process produced almost the same solubility as QHA, while there was large difference for the low barrier case (Fe). The calculated activation energy of permeability fell within the distribution of the experimental values at high temperatures. We consider that the 0 K solution

enthalpy of DFT is a main culprit for the difference from experimental results, which should be overcome by exploiting more accurate ab-initio quantum chemistry calculations.

We have presented a systematic methodology in our research that accurately and automatically calculates hydrogen diffusivity and solubility in bcc metals important for nuclear engineering. The most powerful aspect of this research is its design to automate the entire process, from the generation of MLPs to the calculation of diffusivity, solubility, and permeability. By pre-setting the elements and other details of the metal, diffusivity and solubility can be calculated by the path integral simulations. First of all, the established method can be used to construct a database on diffusivity, solubility and permeability of all hydrogen isotopes for fusion reactor materials. Considering the scarcity and large deviation in currently available data, such a database generated by accurate computational methods will have a large impact and contribution to nuclear fusion materials engineering. In addition, this research can be applied to computational materials designs for finding better functional materials that effectively reduce hydrogen inventory and leakage in nuclear fusion reactors. Likewise, the methods developed in this study can be used to better understand and predict hydrogen behavior in zirconium cladding alloys for nuclear fission reactors. It also can be applied to designing functional materials that prevent hydrogen-induced corrosion or hydrogen leakage in hydrogen ships transporting liquefied hydrogen for hydrogen economy.

Appendix

A1. Key features of moment tensor potential

The building blocks of moment tensor potential are moment tensor descriptors,

$$M_{\mu,\nu}(n_i) = \sum_j f_\mu(|\boldsymbol{r}_{ij}|, z_i, z_j) \, \boldsymbol{r}_{ij} \otimes \cdots \otimes \boldsymbol{r}_{ij}, \qquad \text{Eq. A1}$$

where n_i is the atomic environment of the i-th atom, and $\boldsymbol{r}_{ij}$ is the position of the j-th atom relative to the i-th atom. "$\boldsymbol{r}_{ij} \otimes \cdots \otimes \boldsymbol{r}_{ij}$" denotes ν times of outer products of $\boldsymbol{r}_{ij}$, and it describes the angular part of the interaction. f_μ addresses the radial part of the interaction,

$$f_\mu(|\boldsymbol{r}_{ij}|, z_i, z_j) = \sum_{\beta=1}^{N_Q} c_{\mu,z_i,z_j}^\beta Q^\beta(|\boldsymbol{r}_{ij}|), \qquad \text{Eq. A2}$$

where z_i and z_j are the atomic types of the i-th and j-th atoms, respectively. $\boldsymbol{c} = \left\{ c_{\mu,z_i,z_j}^\beta \right\}$ is a set of radial parameters where μ is the index of radial parameters. N_Q is the number of radial basis functions, and $Q^\beta(|\boldsymbol{r}_{ij}|)$ is the β-th radial basis function which consists of invariant polynomials and a smooth damping function. These polynomials are symmetric to Euclidean transformations (translations, rotations, and reflections) and permutation of equivalent atoms [34].

Moment tensor descriptors lower than a target level of moments are contracted to a set of basis functions $\{B_\alpha\}$, which constructs the site energy of n_i as

$$V^{mtp}(n_i) = \sum_\alpha \xi_\alpha B_\alpha(n_i). \qquad \text{Eq. A3}$$

Here, $\boldsymbol{\xi} = \{\xi_\alpha\}$ is a set of coefficients for basis functions B_α. Finally, the potential energy of a specific configuration (cfg) can be calculated from the sum of every atom's site energy as

$$E^{mtp}(cfg) = \sum_{i=1}^{n} V^{mtp}(n_i).$$

Eq. A4

A set of MTP parameters $\boldsymbol{\theta} = \{\boldsymbol{\xi}, \boldsymbol{c}\}$ are optimized by fitting to a training set composed of energy, force, and stress data, which were prepared by first-principles calculations. The target level of moments is called the MTP level, and it largely determines the accuracy and efficiency of MTP.

A2. Conditions for construction of the MTP training sets

Table A1. The number of configurations included in the initial training sets.

Method	Number of atoms (Metal; H)	Number of configurations	
MCMC*	2;0	122	123
Geometry optimization	54;1	180	180
NEB	54;1	144	96
QHA with H	54;1	45	45
QHA without H	54;0	24	24

The expected effects of the initial training sets are as follows. First, the training sets from Markov-Chain Monte Carlo (MCMC) method with random distortions of lattice vectors were expected to ensure not only reasonable stability of bcc phases at wide temperature and stress conditions, but also accurate elastic properties. Second, Geometry optimized calculations for hydrogen at T, Tri, and O sites at linearly expanded or contracted $3 \times 3 \times 3$ supercells (96% ~ 108% from 0 K lattice constant) would enhance the accuracy of bulk modulus. Third, NEB images of hydrogen migration from T-site to Tri-site, and from T-site to O-site at different lattice parameters (96% ~ 104% from the 0 K lattice constant) are collected to the training sets. Hydrogen migration at thermal lattice fluctuations would be improved by the NEB training sets. Finally, irreducible configurations for the QHA calculations

with finite displacement methods with and without one hydrogen atom at T, Tri, and O sites were collected. The degrees of finite displacement were 0.03 Å, 0.10 Å, or 0.30 Å in isotropically deformed structures (0.96, 1.00, or 1.04 as the linear contraction/expansion coefficients) to partly include the information of anharmonicity.

Table A2. Simulation conditions of the active learning scheme.

Active learning	CLMD	PIMD (64 beads)
ensemble	NPT (0 GPa)	NVT (0 K lattice constant)
Structure	One H atom in a periodic $3\times3\times3$ bcc supercell.	
learning temperature	$Fe_{54}H_1$: 1000 K $W_{54}H_1$: 2400 K	100 K, 300 K
timestep length (fs)	1	0.2
Maximum time (ps)	500	50
γ_{select}*	2	2
γ_{break}*	100	2

* γ is the extrapolation grade which indicates a magnitude of extrapolation from a training set [35].

A3. MTP validation
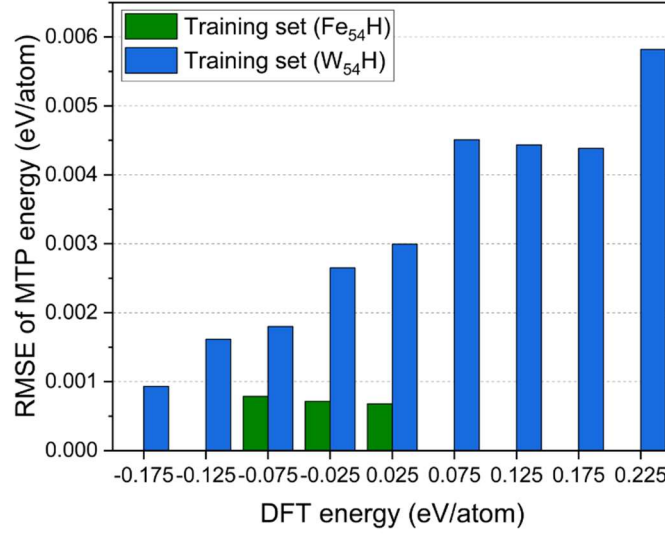
Fig. A1 Root-mean-square error (RMSE) of MTP energies in the training sets.

Table A3. Lattice constants (a_0, unit: Å) and elastic constants (C_{ij}, unit: GPa) of pure bcc metals. In the calculation, a_0 and C_{ij} were obtained from geometry optimization and the stress-strain relation without kinetic contribution, respectively. In the experimental values, the vibration effect at zero-point energy was removed for a_0 [56], and C_{ij} was the extrapolated value at 0 K of the measured data near 4 K [58–60].

	Fe			W		
	MTP	DFT	Exp.	MTP	DFT	Exp.
a_0	2.832	2.832	2.855	3.172	3.172	3.161
C_{11}	258	278	239	533	543	533
C_{12}	142	148	136	203	198	205
C_{44}	96	98	121	140	137	163
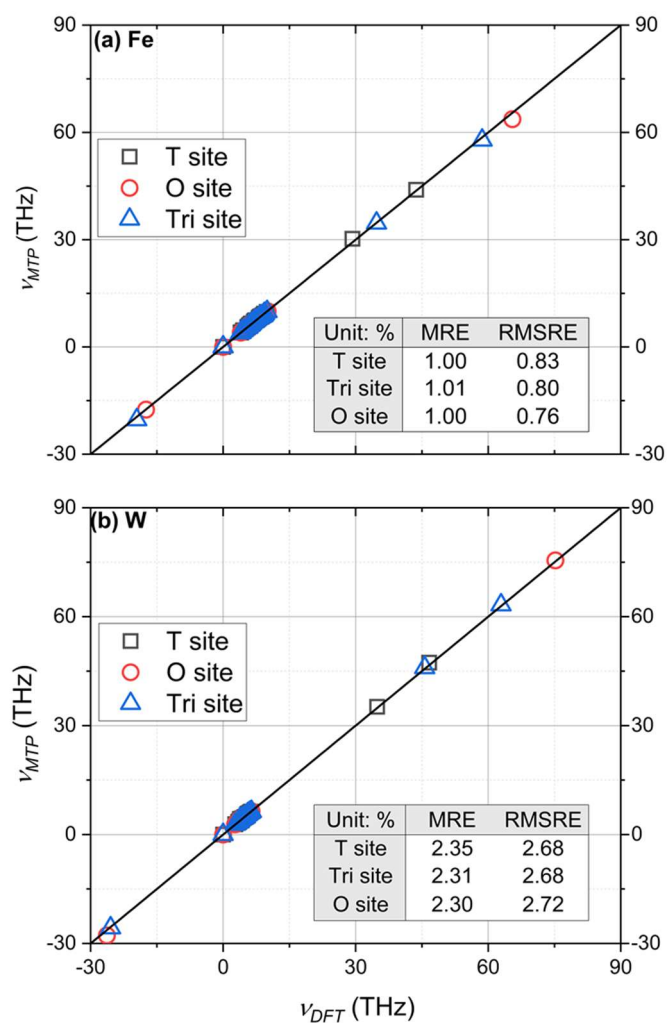
Fig. A2 Vibrational frequencies of normal modes in (a)$Fe_{54}H_1$, and (b)$W_{54}H_1$. Negative frequencies denote imaginary frequencies. Translational modes are not considered in mean relative error (MRE) and root-mean-square relative error (RMSRE).

A4. Simulation conditions of MD simulations

Table A4. Simulation conditions of CLMD/CMD/RPMD/PI-QTST.

Method		CLMD	RPMD	CMD	PI-QTST

Constraints	System	One hydrogen atom in a periodic 4×4×4 bcc supercell			
	Ensemble	NVT	NVE	NVE	NVT
	System size	Thermal equilibrium volume of pure metal by CLMD			0 K lattice constant
Time	Equilibration time (ns)	1	0.2*	0.2*	0
	Production time (ns)	20	3	3	0.025
	Real timestep length (fs)	1	0.25	0.1	
	Imaginary timestep length (fs)**		0.25	0.01	0.1
Control of temperature	Thermostat	Nosé-Hoover thermostat		Massive Nosé-Hoover Chain[102]	
	Number of chains [103]	1		3	4
Adiabaticity parameter				0.0625	

* PIMD simulations under the NVT ensemble were implemented for equilibration of the CMD/RPMD simulations.[104,105]

** Reference system propagator algorithm (RESPA) [106] was employed for time integration.

A5. Codes used in this study

The machine learning interatomic potential (MLIP) package [35], invented by Novikov et al., was used to determine the extrapolation grade of configurations, reinforce the training sets, and reoptimize MTP parameters.

The Vienna Ab Initio Simulation Package (VASP) [45–47] was used to calculate electronic energy, force, and stress of atomic configurations by DFT. Especially, VASP utilizes plane wave basis sets and pseudopotentials to efficiently perform DFT calculations.

The Large-scale Atomic/Molecular Massively Parallel Simulator (LAMMPS) [107] and Path Integral Molecular Dynamics [44] were used to perform atomistic simulations of nuclei in classical and quantum regimes, respectively.

Bibliography

[1]   J. Roth, E. Tsitrone, T. Loarer, V. Philipps, S. Brezinsek, A. Loarte, G.F. Counsell, R.P. Doerner, K. Schmid, O. V. Ogorodnikova, R.A. Causey, Tritium inventory in ITER plasma-facing materials and tritium removal procedures, Plasma Phys Control Fusion. 50 (2008). https://doi.org/10.1088/0741-3335/50/10/103001.

[2]   Y. Hatano, M. Shimada, T. Otsuka, Y. Oya, V.K. Alimov, M. Hara, J. Shi, M. Kobayashi, T. Oda, G. Cao, K. Okuno, T. Tanaka, K. Sugiyama, J. Roth, B. Tyburska-Püschel, J. Dorner, N. Yoshida, N. Futagami, H. Watanabe, M. Hatakeyama, H. Kurishita, M. Sokolov, Y. Katoh, Deuterium trapping at defects created with neutron and ion irradiations in tungsten, Nuclear Fusion. 53 (2013). https://doi.org/10.1088/0029-5515/53/7/073006.

[3]   M. Nishikawa, T. Tanabe, Study on the fuel balance of a DT reactor, in: Fusion Engineering and Design, Elsevier Ltd, 2010: pp. 987–991. https://doi.org/10.1016/j.fusengdes.2009.11.007.

[4]   X. Fang, A. Kreter, M. Rasinski, C. Kirchlechner, S. Brinckmann, C. Linsmeier, G. Dehm, Hydrogen embrittlement of tungsten induced by deuterium plasma: Insights from nanoindentation tests, J Mater Res. 33 (2018) 3530–3536. https://doi.org/10.1557/jmr.2018.305.

[5]   Y. Fukai, The metal-hydrogen system, 2005. https://doi.org/10.1007/3-540-28883-X_2.

[6]   K. Kiuchi, R.B. McLellan, The solubility and diffusivity of hydrogen in well-annealed and deformed iron, Acta Metallurgica. 31 (1983) 961–984. https://doi.org/10.1016/0001-6160(83)90192-X.

[7]   Frauenfelder R, Solution and Diffusion of Hydrogen in Tungsten, J Vacuum Science & Technology. 6 (1969) 388–397. https://doi.org/10.1116/1.1492699.

[8]   T. Otsuka, T. Hoshihira, T. Tanabe, Visualization of hydrogen depth profile by means of tritium imaging plate technique: Determination of hydrogen diffusion

coefficient in pure tungsten, Physica Scripta T. T138 (2009) 014052. https://doi.org/10.1088/0031-8949/2009/T138/014052.

[9] D.E. Jiang, E.A. Carter, Diffusion of interstitial hydrogen into and through bcc Fe from first principles, Phys Rev B. 70 (2004) 064102. https://doi.org/10.1103/PhysRevB.70.064102.

[10] K. Heinola, T. Ahlgren, First-principles study of H on the reconstructed W(100) surface, Phys Rev B Condens Matter Mater Phys. 81 (2010). https://doi.org/10.1103/PhysRevB.81.073409.

[11] Y. Tateyama, T. Ohno, Stability and clusterization of hydrogen-vacancy complexes in (formula presented) An ab initio study, Phys Rev B Condens Matter Mater Phys. 67 (2003). https://doi.org/10.1103/PhysRevB.67.174105.

[12] K. Ohsawa, J. Goto, M. Yamakami, M. Yamaguchi, M. Yagi, Trapping of multiple hydrogen atoms in a tungsten monovacancy from first principles, Phys Rev B Condens Matter Mater Phys. 82 (2010). https://doi.org/10.1103/PhysRevB.82.184117.

[13] T. Oda, D. Zhu, Y. Watanabe, Kinetic Monte Carlo simulation on influence of vacancy on hydrogen diffusivity in tungsten, Journal of Nuclear Materials. 467 (2015) 439–447. https://doi.org/10.1016/j.jnucmat.2015.07.054.

[14] K. Heinola, T. Ahlgren, Diffusion of hydrogen in bcc tungsten studied with first principle calculations, J Appl Phys. 107 (2010) 113531. https://doi.org/10.1063/1.3386515.

[15] T. Oda, Thermodynamic model for grain boundary effects on hydrogen solubility, diffusivity and permeability in poly-crystalline tungsten, Fusion Engineering and Design. 112 (2016) 102–116. https://doi.org/10.1016/j.fusengdes.2016.08.001.

[16] A. Fuoco, M. Monteleone, E. Esposito, R. Bruno, J. Ferrando-Soria, E. Pardo, D. Armentano, J.C. Jansen, Gas transport in mixed matrix membranes: Two methods for time lag determination, Computation. 8 (2020).

https://doi.org/10.3390/COMPUTATION8020028.

[17]   T. Tanabe, Y. Yamanishi, S. Imoto, Hydrogen Transport through Highly Purified Iron, Transactions of the Japan Institute of Metals. 25 (1984) 1–10.

[18]   A. Tahara, Y. Hayashi, Measurements of Permeation of Hydrogen Isotopes through α-Iron by Pressure Modulation and Ion Bombarding, Transactions of the Japan Institute of Metals. 26 (1985) 869–875. https://doi.org/10.2320/matertrans1960.26.869.

[19]   A.P. Zakharov, Hydrogen permeability of polycrystalline and monocrystalline molybdenum and tungsten, Angewandte Chemie International Edition, 6(11), 951–952. 9 (1975) 10–27.

[20]   G.H. Vineyard, Frequency factors and isotope effects in solid state rate processes, Journal of Physics and Chemistry of Solids. 3 (1957) 121–127. https://doi.org/10.1016/0022-3697(57)90059-8.

[21]   Zh Qi, J. Volkl, R. Lasser, H. Wenzl, Tritium diffusion in V, Nb and Ta, Journal of Physics F: Metal Physics. 13 (1983) 2053–2062. https://doi.org/10.1088/0305-4608/13/10/015.

[22]   G. Matusiewicz, H.K. Birnbaum, The isotope effect for the diffusion of hydrogen in niobium, Journal of Physics F: Metal Physics. 7 (1977) 2285–2289. https://doi.org/10.1088/0305-4608/7/11/009.

[23]   H. Wipf, G. Alefeld, Diffusion coefficient and heat of transport of H and D in niobium below room temperature, Physica Status Solidi (a). 23 (1974) 175–186. https://doi.org/10.1002/pssa.2210230119.

[24]   H. Kimizuka, M. Shiga, Two distinct non-Arrhenius behaviors of hydrogen diffusivities in fcc aluminum, silver, and copper determined by ab initio path integral simulations, Phys Rev Mater. 5 (2021) 065406. https://doi.org/10.1103/PhysRevMaterials.5.065406.

[25]   J. Sanchez, J. Fullea, M.C. Andrade, P.L. De Andres, Ab initio molecular dynamics

simulation of hydrogen diffusion in α -iron, Phys Rev B. 81 (2010) 132102. https://doi.org/10.1103/PhysRevB.81.132102.

[26] R.P. Feynman, A.R. Hibbs, D.F. Styer, Quantum Mechanics and Path Integrals, Dover Publications, 2010.

[27] R.P. Feynman, Statistical mechanics, Benjamin, New York, 1972.

[28] D. Marx, M. Parrinello, Ab initio path integral molecular dynamics: Basic ideas, Journal of Chemical Physics. 104 (1996) 4077–4082. https://doi.org/10.1063/1.471221.

[29] M. Shiga, M. Tachikawa, S. Miura, Ab initio molecular orbital calculation considering the quantum mechanical effect of nuclei by path integral molecular dynamics, Chem Phys Lett. 332 (2000) 396–402. https://doi.org/10.1016/S0009-2614(00)01269-0.

[30] M. Shiga, M. Tachikawa, S. Miura, A unified scheme for ab initio molecular orbital theory and path integral molecular dynamics, Journal of Chemical Physics. 115 (2001) 9149–9159. https://doi.org/10.1063/1.1407289.

[31] T. Mueller, A. Hernandez, C. Wang, Machine learning for interatomic potential models, Journal of Chemical Physics. 152 (2020). https://doi.org/10.1063/1.5126336.

[32] H. Kimizuka, B. Thomsen, M. Shiga, Artificial neural network-based path integral simulations of hydrogen isotope diffusion in palladium, Journal of Physics: Energy. 4 (2022) 034004. https://doi.org/10.1088/2515-7655/ac7e6b.

[33] H.E. Sauceda, L.E. Gálvez-González, S. Chmiela, L.O. Paz-Borbón, K.-R. Müller, A. Tkatchenko, BIGDML—Towards accurate quantum machine learning force fields for materials, Nat Commun. 13 (2022) 3733. https://doi.org/10.1038/s41467-022-31093-x.

[34] A. V. Shapeev, Moment tensor potentials: A class of systematically improvable interatomic potentials, Multiscale Modeling and Simulation. 14 (2016) 1153–

1173. https://doi.org/10.1137/15M1054183.

[35]   I.S. Novikov, K. Gubaev, E. V Podryabinkin, A. V Shapeev, The MLIP package: moment tensor potentials with MPI and active learning, Mach Learn Sci Technol. 2 (2021) 025002. https://doi.org/10.1088/2632-2153/abc9fe.

[36]   D. Chandler, P.G. Wolynes, Exploiting the isomorphism between quantum theory and classical statistical mechanics of polyatomic fluids, J Chem Phys. 74 (1981) 4078–4095. https://doi.org/10.1063/1.441588.

[37]   J. Cao, G.A. Voth, The formulation of quantum statistical mechanics based on the Feynman path centroid density. II. Dynamical properties, J Chem Phys. 100 (1994) 5106–5117. https://doi.org/10.1063/1.467176.

[38]   J. Cao, G.A. Voth, The formulation of quantum statistical mechanics based on the Feynman path centroid density. IV. Algorithms for centroid molecular dynamics, J Chem Phys. 101 (1994) 6168–6183. https://doi.org/10.1063/1.468399.

[39]   J. Cao, G.A. Voth, The formulation of quantum statistical mechanics based on the Feynman path centroid density. V. Quantum instantaneous normal mode theory of liquids, J Chem Phys. 101 (1994) 6184–6192. https://doi.org/10.1063/1.468400.

[40]   J. Cao, G.J. Martyna, Adiabatic path integral molecular dynamics methods. II. Algorithms, Journal of Chemical Physics. 104 (1996) 2028–2035. https://doi.org/10.1063/1.470959.

[41]   I.R. Craig, D.E. Manolopoulos, Quantum statistics and classical mechanics: Real time correlation functions from ring polymer molecular dynamics, Journal of Chemical Physics. 121 (2004) 3368–3373. https://doi.org/10.1063/1.1777575.

[42]   B.J. Braams, D.E. Manolopoulos, On the short-time limit of ring polymer molecular dynamics, Journal of Chemical Physics. 125 (2006) 124105. https://doi.org/10.1063/1.2357599.

[43]   A. Witt, S.D. Ivanov, M. Shiga, H. Forbert, D. Marx, On the applicability of centroid and ring polymer path integral molecular dynamics for vibrational spectroscopy,

Journal of Chemical Physics. 130 (2009) 194510. https://doi.org/10.1063/1.3125009.

[44] M. Shiga, PIMD, version 2.5.0, (2022). http://ccse.jaea.go.jp/software/PIMD/index.en.html.

[45] G. Kresse, J. Hafner, Ab initio molecular dynamics for liquid metals, Phys Rev B. 47 (1993) 558–561. https://doi.org/10.1103/PhysRevB.47.558.

[46] G. Kresse, J. Furthmüller, Efficiency of ab-initio total energy calculations for metals and semiconductors using a plane-wave basis set, Comput Mater Sci. 6 (1996) 15–50. https://doi.org/10.1016/0927-0256(96)00008-0.

[47] G. Kresse, J. Furthmüller, Efficient iterative schemes for ab initio total-energy calculations using a plane-wave basis set, Phys. Rev. B. 54 (1996) 11169–11186. https://doi.org/10.1103/PhysRevB.54.11169.

[48] J.P. Perdew, K. Burke, M. Ernzerhof, Generalized gradient approximation made simple, Phys Rev Lett. 77 (1996) 3865–3868. https://doi.org/10.1103/PhysRevLett.77.3865.

[49] H.J. Monkhorst, J.D. Pack, Special points for Brillouin-zone integrations, Phys. Rev. B. 13 (1976) 5188–5192. https://doi.org/10.1103/PhysRevB.13.5188.

[50] G. Henkelman, H. Jónsson, Improved tangent estimate in the nudged elastic band method for finding minimum energy paths and saddle points, Journal of Chemical Physics. 113 (2000) 9978–9985. https://doi.org/10.1063/1.1323224.

[51] H. Kwon, T. Oda, Moment Tensor Potential for hydrogen diffusion in bcc metals, Mendeley Data. (2023). https://doi.org/10.17632/dzsdvm4yjc.1.

[52] Z.S. Basinski, W. Hume-Rothery, A.L. Sutton, The Lattice Expansion of Iron, Proc R Soc Lond A Math Phys Sci. 229 (1955) 459–467.

[53] J.-W. Hwang, Thermal expansion of nickel and iron, and the influence of nitrogen on the lattice parameter of iron at the Curie temperature, Masters Theses. 5049

(1972).

[54] B.N. Dutta, B. Dayal, Lattice Constants and Thermal Expansion of Palladium and Tungsten up to 878 °C by X-Ray Method, Physica Status Solidi (B). 3 (1963) 2253–2259. https://doi.org/10.1002/pssb.19630031207.

[55] K. Wang, R.R. Reeber, The role of defects on thermophysical properties: Thermal expansion of V, Nb, Ta, Mo and W, Materials Science and Engineering R: Reports. 23 (1998) 101–137. https://doi.org/10.1016/S0927-796X(98)00011-4.

[56] P. Hao, Y. Fang, J. Sun, G.I. Csonka, P.H.T. Philipsen, J.P. Perdew, Lattice constants from semilocal density functionals with zero-point phonon correction, Phys Rev B. 85 (2012) 099903. https://doi.org/10.1103/PhysRevB.85.014111.

[57] V. Smirnov, Yu M and Finkel, Crystal structure of tantalum, niobium, and vanadium at 110-400 K, J. Exptl. Theoret. Phys. (U.S.S.R.). 22 (1966) 1077–1082.

[58] K.J. Carroll, Elastic Constants of Niobium from 4.2° to 300°K, J Appl Phys. 36 (1965) 3689–3690. https://doi.org/10.1063/1.1703072.

[59] J.J. Adams, D.S. Agosta, R.G. Leisure, H. Ledbetter, Elastic constants of monocrystal iron from 3 to 500 K, J Appl Phys. 100 (2006) 113530. https://doi.org/10.1063/1.2365714.

[60] F.H. Featherston, J.R. Neighbours, Elastic constants of tantalum, tungsten, and molybdenum, Physical Review. 130 (1963) 1324–1333. https://doi.org/10.1103/PhysRev.130.1324.

[61] M.J. Gillan, Quantum simulation of hydrogen in metals, Phys Rev Lett. 58 (1987) 563–566. https://doi.org/10.1103/PhysRevLett.58.563.

[62] G.K. Schenter, G. Mills, H. Jónsson, Reversible work based quantum transition state theory, J Chem Phys. 101 (1994) 8964–8971. https://doi.org/10.1063/1.468447.

[63] J.O. Richardson, S.C. Althorpe, Ring-polymer molecular dynamics rate-theory in

the deep-tunneling regime: Connection with semiclassical instanton theory, Journal of Chemical Physics. 131 (2009) 214106. https://doi.org/10.1063/1.3267318.

[64]   D. Chandler, Statistical mechanics of isomerization dynamics in liquids and the transition state approximation, J Chem Phys. 68 (1978) 2959–2970. https://doi.org/10.1063/1.436049.

[65]   B.J. Berne, M. Borkovec, J.E. Straub, Classical and modern methods in reaction rate theory, Journal of Physical Chemistry. 92 (1988) 3711–3725. https://doi.org/10.1021/j100324a007.

[66]   E. Pollak, Variational transition state theory for reactions in condensed phases, J Chem Phys. 95 (1991) 533–539. https://doi.org/10.1063/1.461453.

[67]   R.F. Miller, J.B. Hudson, G.S. Ansell, Permeation of hydrogen through alpha iron, Metallurgical Transactions A. 6 (1975) 117–121. https://doi.org/10.1007/BF02673678.

[68]   H.G. Nelson, J.E. Stein, Gas-phase hydrogen permeation through alpha iron, 4130 steel, and 304 stainless steel from less than 100 C to near 600 C, NASA-Tn-D-7265. (1973).

[69]   J. Völkl, G. Alefeld, Diffusion in solids, Academic Press, New York, 1975. https://doi.org/10.1016/B978-0-12-522660-8.X5001-6.

[70]   N.R. Quick, H.H. Johnson, Hydrogen and deuterium in iron, 49-506°C, Acta Metallurgica. 26 (1978) 903–907. https://doi.org/10.1016/0001-6160(78)90041-X.

[71]   G. Holzner, T. Schwarz-Selinger, T. Dürbeck, U. Von Toussaint, Solute diffusion of hydrogen isotopes in tungsten- A gas loading experiment, Phys Scr. 2020 (2020) 014034. https://doi.org/10.1088/1402-4896/ab4b42.

[72]   T. Yoshikawa, T. Takayanagi, H. Kimizuka, M. Shiga, Quantum-thermal crossover of hydrogen and tritium diffusion in α-iron, Journal of Physical Chemistry C. 116 (2012) 23113–23119. https://doi.org/10.1021/jp307660e.

112

[73] B. Cheng, A.T. Paxton, M. Ceriotti, Hydrogen Diffusion and Trapping in α -Iron: The Role of Quantum and Anharmonic Fluctuations, Phys Rev Lett. 120 (2018) 225901. https://doi.org/10.1103/PhysRevLett.120.225901.

[74] R. Ash, R.M. Barrer, D.G. Palmer, Diffusion in multiple laminates, British Journal of Applied Physics. 16 (1965) 873–884. https://doi.org/10.1088/0508-3443/16/6/314.

[75] C.R. Cupp, Gases in metals, 1953. https://doi.org/10.1016/0502-8205(53)90016-1.

[76] Y. Hayashi, H. Hagi, A. Tahara, Diffusion Coefficients of Hydrogen and Deuterium in Iron Determined by Permeation with Gas, Ion and Electrochemical Charging, Zeitschrift Fur Physikalische Chemie. 164 (1989) 815–820. https://doi.org/10.1524/zpch.1989.164.Part_1.0815.

[77] K. Yamakawa, T. Tsuruta, S. Yoshizawa, Interaction Between Dislocation and Hydrogen Occluded in Single Crystal of Iron., Boshoku Gijutsu. 30 (1981) 443–449. https://doi.org/10.3323/jcorr1974.30.8_443.

[78] W. Beck, Hydrogen permeation in metals as a function of stress, temperature and dissolved hydrogen concentration, Proc R Soc Lond A Math Phys Sci. 290 (1966) 220–235. https://doi.org/10.1098/rspa.1966.0046.

[79] H. Hagi, Y. Hayashi, N. Ohtani, Diffusion Coefficient of Hydrogen in Pure Iron Between 230 and 300 K., Transactions of the Japan Institute of Metals. 20 (1979) 349–357. https://doi.org/10.2320/matertrans1960.20.349.

[80] S. Asano, K. Hara, Y. Nakai, N. Ohtani, Effect of Trapping By Dislocations on Hydrogen Diffusion in Mild Steel., Nippon Kinzoku Gakkaishi/Journal of the Japan Institute of Metals. 38 (1974) 626–632. https://doi.org/10.2320/jinstmet1952.38.7_626.

[81] A.J. Kumnick, H.H. Johnson, Hydrogen Transport Through Annealed and Deformed Armco Iron., Metall Trans. 5 (1974) 1199–1206.

https://doi.org/10.1007/BF02644334.

[82]   J. McBreen, Ph.D. Thesis, Univ. Pennsylvania, PA, 1971.

[83]   P.K. Subramanyan, Ph.D. Thesis, Univ. Pennsylvania, PA, 1971.

[84]   A.T. Paxton, I.H. Katzarov, Quantum and isotope effects on hydrogen diffusion, trapping and escape in iron, Acta Mater. 103 (2016) 71–76. https://doi.org/10.1016/j.actamat.2015.09.054.

[85]   A.T. Paxton, C. Elsässer, Electronic structure and total energy of interstitial hydrogen in iron: Tight-binding models, Phys Rev B. 82 (2010) 235125. https://doi.org/10.1103/PhysRevB.82.235125.

[86]   W. Fang, J.O. Richardson, J. Chen, X.Z. Li, A. Michaelides, Simultaneous Deep Tunneling and Classical Hopping for Hydrogen Diffusion on Metals, Phys Rev Lett. 119 (2017) 126001. https://doi.org/10.1103/PhysRevLett.119.126001.

[87]   M. Nagano, Y. Hayashi, N. Ohtani, M. Isshiki, K. Igaki, Diffusion of Hydrogen and Deuterium in High Purity Iron Between 222 and 322 K., Transactions of the Japan Institute of Metals. 22 (1981) 423–429. https://doi.org/10.2320/matertrans1960.22.423.

[88]   H. Hagi, Y. Hayashi, Effect of Dislocation Trapping on Hydrogen and Deuterium Diffusion in Iron., Transactions of the Japan Institute of Metals. 28 (1987) 368–374. https://doi.org/10.2320/matertrans1960.28.368.

[89]   Donal A. McQuarrie, Statistical Mechanics, 2000.

[90]   S. Habershon, D.E. Manolopoulos, Thermodynamic integration from classical to quantum mechanics, Journal of Chemical Physics. 135 (2011). https://doi.org/10.1063/1.3666011.

[91]   H.T. Fellow, R.H. Fowler, A theoretical formula for the solubility of hydrogen in palladium, Proc R Soc Lond A Math Phys Sci. 161 (1937) 525–545. https://doi.org/10.1098/rspa.1937.0160.

[92]   H. Ogawa, A statistical-mechanical method to evaluate hydrogen solubility in metal, Journal of Physical Chemistry C. 114 (2010) 2134–2143. https://doi.org/10.1021/jp906506z.

[93]   H. Sugimoto, Y. Fukai, Theory of light interstitials in bcc metals. I. Self-trapped state of hydrogen and muons in Nb, Phys Rev B. 22 (1980) 670–680. https://doi.org/10.1103/PhysRevB.22.670.

[94]   I. ESTERMANN, R. FRISCH, O. STERN, Magnetic Moment of the Proton, Nature. 132 (1933) 169–170. https://doi.org/10.1038/132169a0.

[95]   H.F. Trotter, On the Product of Semi-Groups of Operators, Proceedings of the American Mathematical Society. 10 (1959) 545–551. https://doi.org/10.2307/2033649.

[96]   M. Suzuki, Mathematical Physics Generalized Trotter's Formula and Systematic Approximants of Exponential Operators and Inner Derivations with Applications to Many-Body Problems, 1976.

[97]   V. Stevanović, S. Lany, X. Zhang, A. Zunger, Correcting density functional theory for accurate predictions of compound enthalpies of formation: Fitted elemental-phase reference energies, Phys Rev B Condens Matter Mater Phys. 85 (2012). https://doi.org/10.1103/PhysRevB.85.115104.

[98]   K. Lee, M. Yuan, J. Wilcox, Understanding Deviations in Hydrogen Solubility Predictions in Transition Metals through First-Principles Calculations, Journal of Physical Chemistry C. 119 (2015) 19642–19653. https://doi.org/10.1021/acs.jpcc.5b05469.

[99]   X.S. Kong, S. Wang, X. Wu, Y.W. You, C.S. Liu, Q.F. Fang, J.L. Chen, G.N. Luo, First-principles calculations of hydrogen solution and diffusion in tungsten: Temperature and defect-trapping effects, Acta Mater. 84 (2015) 426–435. https://doi.org/10.1016/j.actamat.2014.10.039.

[100] P.N. Anyalebechi, Hydrogen Solubility in Liquid and Solid Pure Aluminum—

Critical Review of Measurement Methodologies and Reported Values, Materials Sciences and Applications. 13 (2022) 158–212. https://doi.org/10.4236/msa.2022.134011.

[101] H. Kwon, M. Shiga, H. Kimizuka, T. Oda, Accurate description of hydrogen diffusivity in bcc metals using machine-learning moment tensor potentials and path-integral methods, Acta Mater. 247 (2023). https://doi.org/10.1016/j.actamat.2023.118739.

[102] D.J. Tobias, G.J. Martyna, M.L. Klein, Molecular dynamics simulations of a protein in the canonical ensemble, J Phys Chem. 97 (1993) 12959–12966. https://doi.org/10.1021/j100151a052.

[103] G.J. Martyna, M.L. Klein, M. Tuckerman, Nosé-Hoover chains: The canonical ensemble via continuous dynamics, J Chem Phys. 97 (1992) 2635–2643. https://doi.org/10.1063/1.463940.

[104] S. Nosé, A unified formulation of the constant temperature molecular dynamics methods, J Chem Phys. 81 (1984) 511–519. https://doi.org/10.1063/1.447334.

[105] W.G. Hoover, Canonical dynamics: Equilibrium phase-space distributions, Phys. Rev. A. 31 (1985) 1695–1697. https://doi.org/10.1103/PhysRevA.31.1695.

[106] G.J. Martyna, M.E. Tuckerman, D.J. Tobias, M.L. Klein, Explicit reversible integrators for extended systems dynamics, Mol Phys. 87 (1996) 1117–1157. https://doi.org/10.1080/00268979600100761.

[107] A.P. Thompson, H.M. Aktulga, R. Berger, D.S. Bolintineanu, W.M. Brown, P.S. Crozier, P.J. in 't Veld, A. Kohlmeyer, S.G. Moore, T.D. Nguyen, R. Shan, M.J. Stevens, J. Tranchida, C. Trott, S.J. Plimpton, LAMMPS - a flexible simulation tool for particle-based materials modeling at the atomic, meso, and continuum scales, Comput Phys Commun. 271 (2022). https://doi.org/10.1016/j.cpc.2021.108171.

국문초록

수소의 확산도, 용해도 및 투과도는 그 풍부한 물리적 특성과 재료 공학에서의 중요성으로 인해 광범위하게 연구되었다. 원자력 재료 공학에서는 핵연료 피복관 재료로 사용되는 Zr 수소화물이 합금의 연성을 심각하게 저하시키기에 이를 깊이 연구하고 있다. 핵 융합 반응로의 개발을 위해, 금속 내에서 수소 동위원소로 인한 취약화/손상뿐만 아니라 삼중수소 자체의 거동도 중요한 연구 주제이다. 방사성 삼중수소에 대한 안전 규정을 충족하기 위해 핵 반응로 구성 요소에서의 삼중수소 축적과 누출을 최소화해야 한다. 따라서, 핵융합의 삼중수소 연료 주기를 유지하기 위해서도 삼중수소의 손실은 최대한 예방되어야 한다.

많은 실험적 노력에도 불구하고, 표면 및 포집 효과로 인해 수소의 확산 계수와 용해도 상수에 대한 실험 데이터에는 큰 편차가 있으며, 특히 낮은 온도에서 정확한 측정이 내재적으로 어렵다. 계산 연구를 위해, 특정 원자 시뮬레이션으로 격자 내의 실제 수소 확산성과 용해도를 결정하는 데 사용되었지만, 대부분의 연구에서는 힘장 (force field), 동적 효과 또는 핵 양자 효과를 정확하게 모사하지 못해 그 정확성이 의문스럽다.

본 연구에서는 체심입방구조의 철과 텅스텐에 해 긴 시간의 경로 시뮬레이션을 사용하여 머신러닝 모멘트 텐서 포텐셜과 밀도 범함수 이론(DFT)의 정확도로 작은 농도의 수소 확산성과 용해도를 추정하였다. 이 방법은 힘장, 동적 효과, 핵 양자 효과(NQE) 이 세 가지 요소를 동시에 정확하게 처리한다.

확산 계수 실험 결과, 신뢰할 만한 온도 범위(철의 경우 500 K 이상, 텅스텐의 경우 1500 K 이상)에서 본 계산 결과가 실험값과의 높은 일치도를 보였다. 수소의 확산 계수는 철과 텅스텐에서 500 K 미만의 온도에서 핵 양자

효과로 인해 비선형 아레니우스 그래프를 보였다. 동위원소 효과에 관해서는, 500 K 이상의 고전적인 확산 계수에 대해서도 확산도의 비율이 질량 비율의 제곱근에서 벗어났다. 이는 수소-포논 결합에 의해 야기되는 동적 효과로 설명할 수 있다.

본 용해도 계산 과정은 이전 연구에서 사용된 준조화 가정(QHA)과 같은 방법에 비해 동적 효과와 핵 양자 효과의 결합이 완전히 포함되어 있어 이론적으로 더 정확하다. 높은 온도에서 용해도보다 투과성이 실험에서 더 정확하게 측정될 수 있기 때문에 용해도의 정확성을 투과성으로 변환시켜 간접적으로 실험값과 비교했다. 결과는 사용 가능한 실험값과 비교하여 허용 가능한 오차 수준을 보였으며, 동시에 밀도 범함수 이론의 체계적인 오차가 머신러닝 포텐셜을 통해 일부 용해도로 전달되었을 것이라 예측하고 있다. 이러한 결과는 넓은 온도 범위에서 정밀한 측정이 실험 연구와 간단한 계산 방법에서 여전히 어려운 도전임을 보여준다. 지금까지 많은 연구에서는 QHA를 사용하여 금속에서 수소의 확산성과 용해도를 계산했으나, 근사법의 엄격한 검증 없이 수행되었다. 본 연구에 따르면, 동적 효과(예: 철에서의 핵 양자 효과)가 중요한 경우에는 QHA를 사용하면 수소의 용해도에 대해 수십 배의 오차가 발생할 수 있다. 본 연구는 경로 적분 시뮬레이션과 통계 역학적 기법의 결합을 통해 동적 효과와 핵 양자 효과를 정확하게 고려하는 방법론을 개발함으로써 분자 동력학의 적용 가능성을 높였다.

본 연구자는 체심입방구조 금속에서 수소의 확산성과 용해도를 정확하게 계산하는 체계적인 방법론을 개발했으며, 전체 과정을 자동화할 수 있도록 하였다. 이 연구는 핵융합 반응로 재료를 위한 수소 동위원소의 확산도, 용해도 및 투과도에 관한 포괄적인 데이터베이스를 생성하는 데에 사용될 수 있으므로 핵융합 재료 공학의 발전에 크게 기여할 수 있다. 또한, 본 연구에서 사용된 방법은 핵 분열 반응로 및 수소 경제에서 발생하는 수소

관련 문제를 해결하는 기능성 재료의 설계에도 적용할 수 있다.